TECHNICAL DESIGN REPORT

The NEXT-100 experiment

(22 November 2011)

Abstract

We present a Technical Design Report (TDR) describing the NEXT-100 detector. This documents formalizes the ANGEL design presented in our Conceptual Design Report (CDR). The baseline detector is designed to hold a maximum of about 150 kg of ^{136}Xe at 15 bar, or 100 kg at 10 bar. This option builds in the capability to increase the total isotope mass by 50% while keeping the operating pressure at a manageable level.

With respect to the CDR the design is simplified in several aspects: (a) a simple lead shielding is chosen; (b) a low-background stainless-steel pressure vessel is preferred to a titanium vessel for reasons of simplicity and cost-effectiveness; (c) an inner lining of ultra-pure copper, 12 cm thick *inside the pressure vessel* reduces the activity of the detector outer shells (lead shield and steel vessel) to even lower levels than those achieved at the CDR.

The ANGEL design calls for an asymmetric TPC, with photomultipliers behind a transparent cathode and position-sensitive light pixels behind the anode. We have chosen the low background R11410-10 PMTs for energy and timing and Hamamatsu MPPCs (S10362-11-050P model) as tracking pixels. Each individual PMT will be isolated from the gas by an individual, pressure resistant enclosure and will be couple to the sensitive volume through a sapphire window coated with terphenyl-butadiene (TPB) . MPPCs will be arranged in Dice Boards (DB) holding 64 sensors each in an array of 8×8 sensors. The light tube will also be coated with TPB.

To be competitive with the other two large xenon experiments, EXO and KamLand-ZEN, it is imperative that the detector is operative as soon as possible. Our goal is to start data taking in 2014. For that purpose we have designed an aggressive construction schedule that will extent through 2012, leading to detector commissioning in mid 2013.

The NEXT collaboration

E. Gómez, M. Losada, R. Gutiérrez, G. Navarro
Universidad Antonio Nariño, Bogotá, Colombia

L. Labarga
Universidad Autónoma de Madrid, Spain

A.L. Ferreira, C.A.B. Oliveira, J.F.C.A. Veloso
Universidade de Aveiro, Aveiro, Portugal

D. Chan, A. Goldschmidt, D. Hogan, T. Miller, D. Nygren,
J. Renner, D. Shuman, H. Spieler, T. Weber
Lawrence Berkeley National Laboratory, Berkeley CA, USA

F.I.G. Borges, C.A.N. Conde, T.H.V.T. Dias, L.M.P. Fernandes, E.D.C. Freitas,
J.A.M. Lopes, C.M.B. Monteiro, H. Natal da Luz, F.P. Santos, J.M.F. dos Santos
Universidade de Coimbra, Coimbra, Portugal

M. Batallé, L. Ripoll
Universitat de Girona, Girona, Spain

J. Hauptman
Iowa State University, USA

P. Evtoukhovitch, V. Kalinnikov, A. Moiseenko, Z. Tsamalaidze, E. Velicheva
Joint Institute for Nuclear Research (JINR), Dubna, Russia

E. Ferrer-Ribas, I. Giomataris, F.J. Iguaz
IRFU, Centre d'Études Nucléaires de Saclay, Gif-sur-Yvette, France

J.A. Hernando Morata, D. Vázquez
Universidade de Santiago de Compostela, Santiago de Compostela, Spain

C. Sofka, R. C. Webb, J. White
Texas A&M University, College Station TX, USA

J.M. Catalá, R. Esteve, V. Herrero,
A. Méndez, J.M. Monzó, F.J. Mora, J.F. Toledo
I3M, Universidad Politécnica de Valencia, Valencia, Spain

R. Palma, J.L. Pérez-Aparicio
Universidad Politécnica de Valencia, Valencia, Spain

V. Álvarez, M. Ball, J. Bayarri, S. Cárcel, A. Cervera,
J. Díaz, P. Ferrario, A. Gil, J.J. Gómez-Cadenas*, K. González,
I. Liubarsky, D. Lorca, J. Martín-Albo, F. Monrabal, J. Muñoz Vidal,

*Spokesperson. Contact email: gomez@mail.cern.ch

M. Nebot, J. Pérez, J. Rodríguez, L. Serra, M. Sorel, N. Yahlali
Instituto de Física Corpuscular (IFIC), CSIC & Univ. de Valencia, Valencia, Spain

J.M. Carmona, J. Castel, S. Cebrián, T. Dafni, H. Gómez, D.C. Herrera,
I.G. Irastorza, G. Luzón, A. Rodríguez, L. Seguí, A. Tomás, J.A. Villar
Lab. de Física Nuclear y Astropartículas, Universidad de Zaragoza, Zaragoza, Spain

Contents

Part I

The NEXT-100 detector

Chapter 1

Apparatus

1.1 Introduction

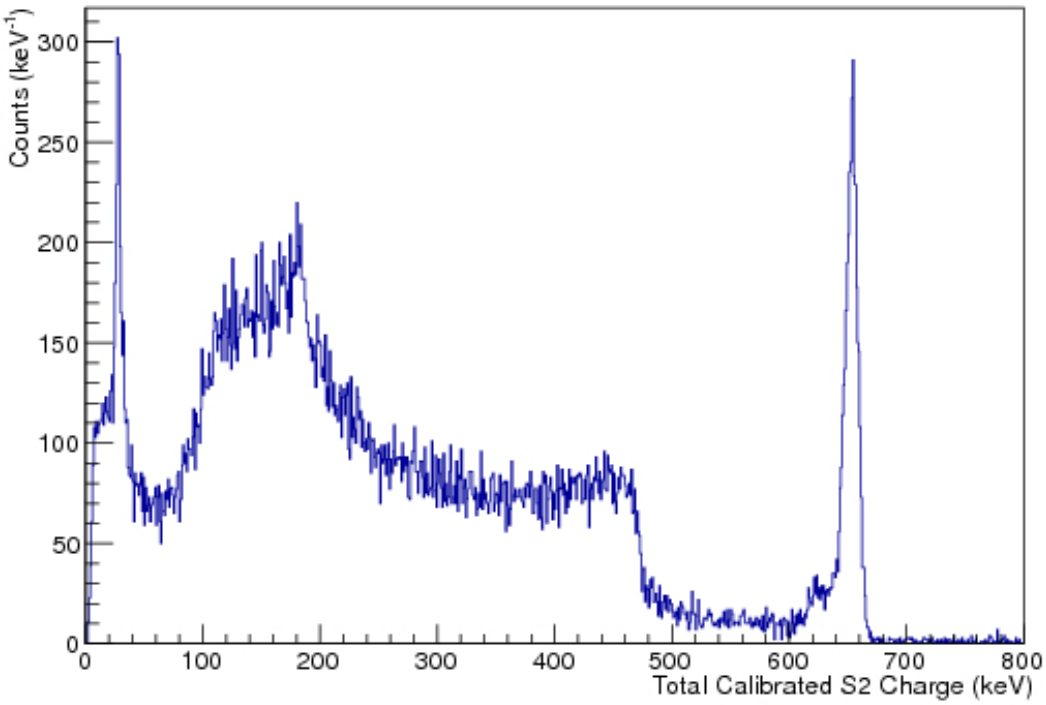

Figure 1.1: The energy spectrum of ^{137}Cs recorded by the NEXT-ENE prototype. The resolution of the photoelectric peak is 1.1%. This extrapolates to 0.5% at $Q_{\beta\beta}$, near the intrinsic limit dictated by Fano factor.

The NEXT experiment will search for $\beta\beta0\nu$ events in ^{136}Xe using a high-pressure gas Xenon (HPGXe) TPC. The main advantages of our technique over the direct competition

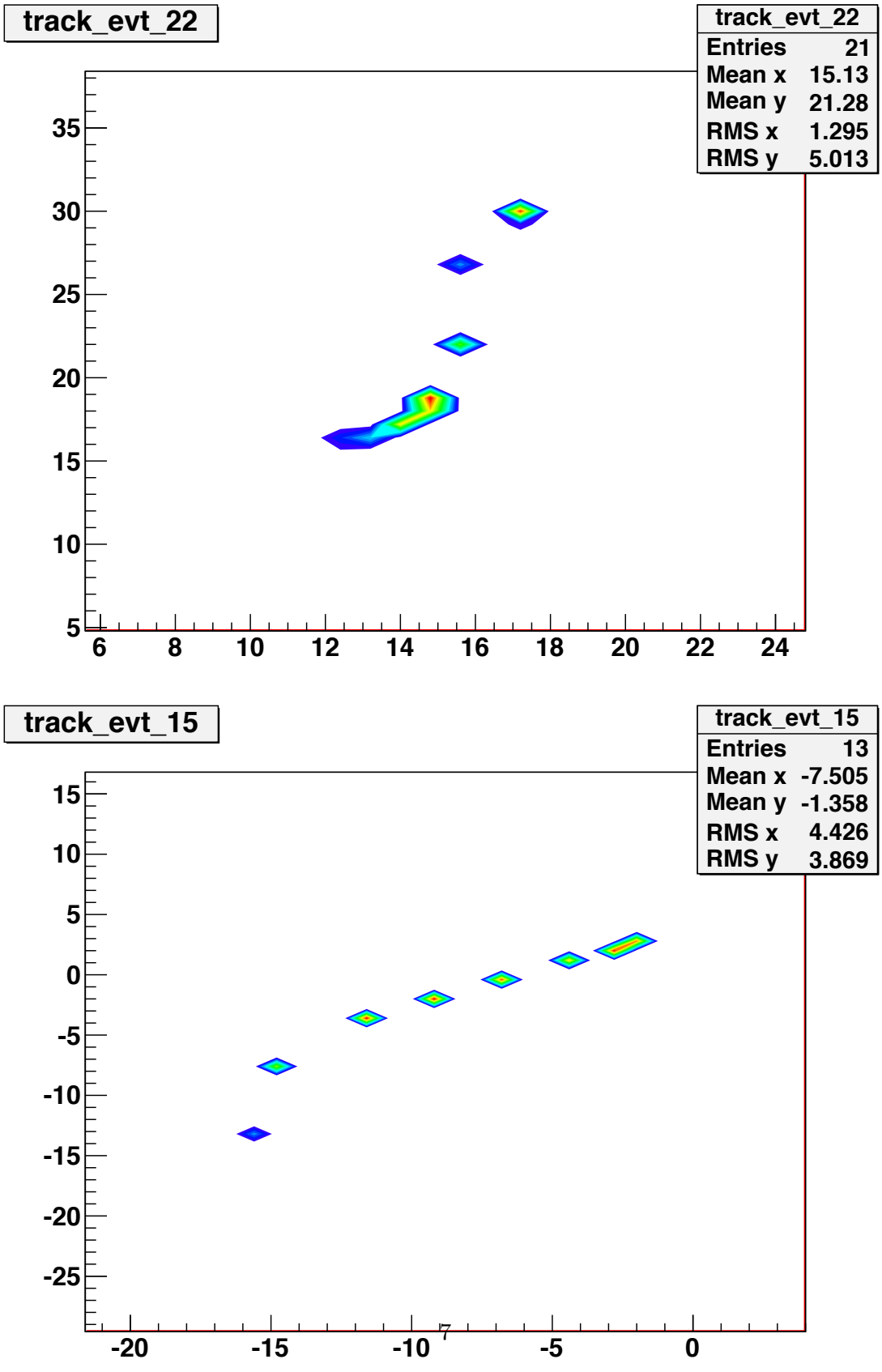

Figure 1.2: Tracks recorded in the NEXT-DEMO prototype.

– the Xenon-based experiments EXO [1] and KamLAND-ZEN [2,3] – are:

1. *The excellent energy resolution.* The intrinsic limit in gas, dominated by the Fano factor is near 0.3% [4]. The NEXT collaboration has measured the resolution attainable with HPGXe prototypes using electroluminescence (EL). A measurement, using a small prototype [5] yielded an extrapolated value of 0.4% FWHM in $Q_{\beta\beta}$. Recent measurements carried out with the large NEXT-DBDM prototype yields a resolution near 1% FWHM at the ^{137}Cs photopeak (the best measured value is 1.05%) which extrapolates to better than 0.5% at $Q_{\beta\beta}$(Figure 1.1). This energy resolution is a factor 10 better than the best value expected by EXO and a factor 20 better than the current values achieved by EXO and KamLAND-ZEN.

2. *The availability of a topological signature.* A HPGXe offers the possibility to determine the complete topology of each event in 3-D, based on energy-sensitive tracking of the $\beta\beta$ decay electrons and identification of "satellite" deposits. The NEXT topological signature has been studied in great detail using MC simulation (see our CDR). Background rejection factors of up to a factor 100 are possible exploiting the topology. The NEXT-DEMO prototype is currently reconstructing the topology of electrons emitted by Cs-137, Na-22 and Co-60 sources (Figure 1.2 shows two electrons produced by 660 keV photons emitted by a Cs-137 source).

Nevertheless, one should not forget that both EXO and KamLAND-Zen are already taking data with enriched xenon. To compete successfully with them the NEXT experiment must start as soon as possible. In this TDR we present a schedule that would result in completing the detector by mid 2013 and would make it possible to run as soon as 2014. If funds are available, a total mass of 150 kg could be deployed.

Does NEXT have a physics case given the fact that it has less mass than the competition and starts later? To assess this question, we write down the simple formula often used to express the sensitivity of an experiment in terms of its operative parameters:

$$T_{1/2}^{-1} \propto a \cdot \epsilon \sqrt{\frac{M \cdot t}{\Delta E \cdot B}} \tag{1.1}$$

where a is the isotopic abundance, ϵ the overall efficiency, $M \cdot t$ the total exposure ΔE the resolution and B the background rate in the experiment.

Table 1.1 shows the values of the parameters entering the sensitivity of xenon-based experiments, that we take from [6], except for the mass of KamLAND-ZEN (KZEN) which is set to 330 rather than to 400 and the efficiency which is set to 33% rather than 61%. Both numbers are updated after the recent DBD-2011 workshop in which KZEN has announced the initial mass dissolved in the liquid xenon (370 kg) and a fiducial cut to suppress backgrounds in the balloon, not taken into account in [6].

We can compare EXO and NEXT, requiring that both achieve the same sensitivity.

$$0.8 \cdot 0.34 \sqrt{\frac{200 \cdot t_{EXO}}{100 \times 8 \cdot 10^{-4}}} = 0.9 \cdot 0.33 \sqrt{\frac{100 \cdot t_{NEXT}}{18 \times 2 \cdot 10^{-4}}} \tag{1.2}$$

Table 1.1: Parameters entering the sensitivity of xenon-based $\beta\beta0\nu$ experiments (from [6])

Parameter	EXO	KZEN	NEXT
a	0.8	0.9	0.9
ϵ	0.34	0.33	0.33
ΔE (FWHM in keV at $Q_{\beta\beta}$)	100	250	18
B (in counts/(keV $\cdot$ kg $\cdot$ y))	8×10^{-4}	2×10^{-4}	2×10^{-4}
M (total, in kg)	200	330	100

to find that the exposure time of NEXT needs to be only 0.07 of that of EXO to reach the same sensitivity. This is roughly 15 years of EXO for each year of NEXT. Clearly, with respect to EXO, NEXT physics case is strong.

Let's now compare with KZEN

$$0.9 \cdot 0.33\sqrt{\frac{330 \cdot t_{KZEN}}{250 \times 2 \cdot 10^{-4}}} = 0.9 \cdot 0.33\sqrt{\frac{100 \cdot t_{NEXT}}{18 \times 2 \cdot 10^{-4}}} \tag{1.3}$$

The ratio between both experiments (in exposure time) is 0.24. This is roughly 4 years of KZEN for each year of NEXT. Therefore, with respect to KZEN, NEXT physics case is also solid.

Although clearly the numbers used in this simple exercise must be taken with a grain of salt, it illustrates the basic fact that NEXT can be a very strong competitor if it achieves its design goal and runs and starts data taking reasonably soon. Thus, the aggressive schedule presented in this TDR.

1.2 Detector principles

The NEXT-100 detector will be an asymmetric SOFT HPGXe TPC. The Separated Optimized FuncTions (SOFT) principle requires that tracking and energy measurements are carried out by different sensors optimized for each specific function. Figure 1.3 illustrates the idea. An event, shown as a wiggly track, generates primary scintillation recorded at both planes (S_1). EL light generated at the anode (S_2) is recorded in the photosensor plane right behind it and used for tracking. It is also recorded in the photosensor plane behind the transparent cathode and used for a precise energy measurement.

The design presented in this TDR follows the ANGEL concept described in our CDR [7]. The source mass of the NEXT experiment is gas xenon enriched in the ^{136}Xe isotope. The total mass of ^{136}Xe available for the first phase of the experiment is 100 kg. The pressure vessel has been designed to fit such mass at an operative pressure of 10 bar, but all the systems are designed to operate up to 15 bar. Therefore a total mass of up to 150 kg can be accommodated without modifying the apparatus.

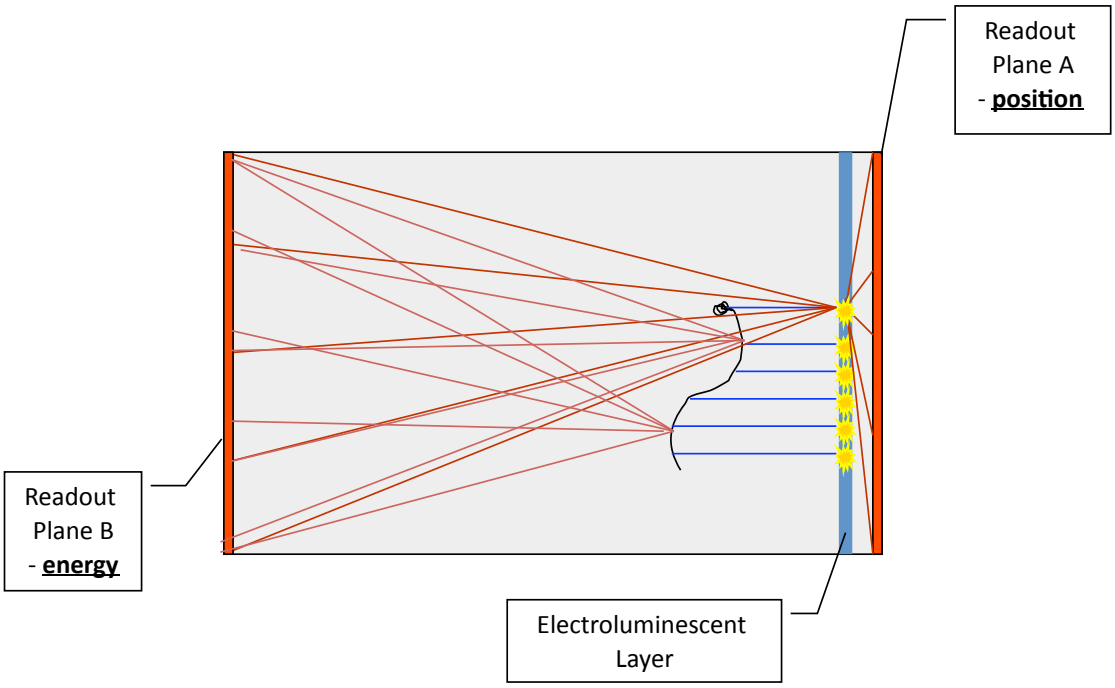

Figure 1.3: The SOFT concept. EL light generated at the anode is recorded in the photosensor plane right behind it and used for tracking. It is also recorded in the photosensor plane behind the transparent cathode and used for a precise energy measurement.

1.3 The detector

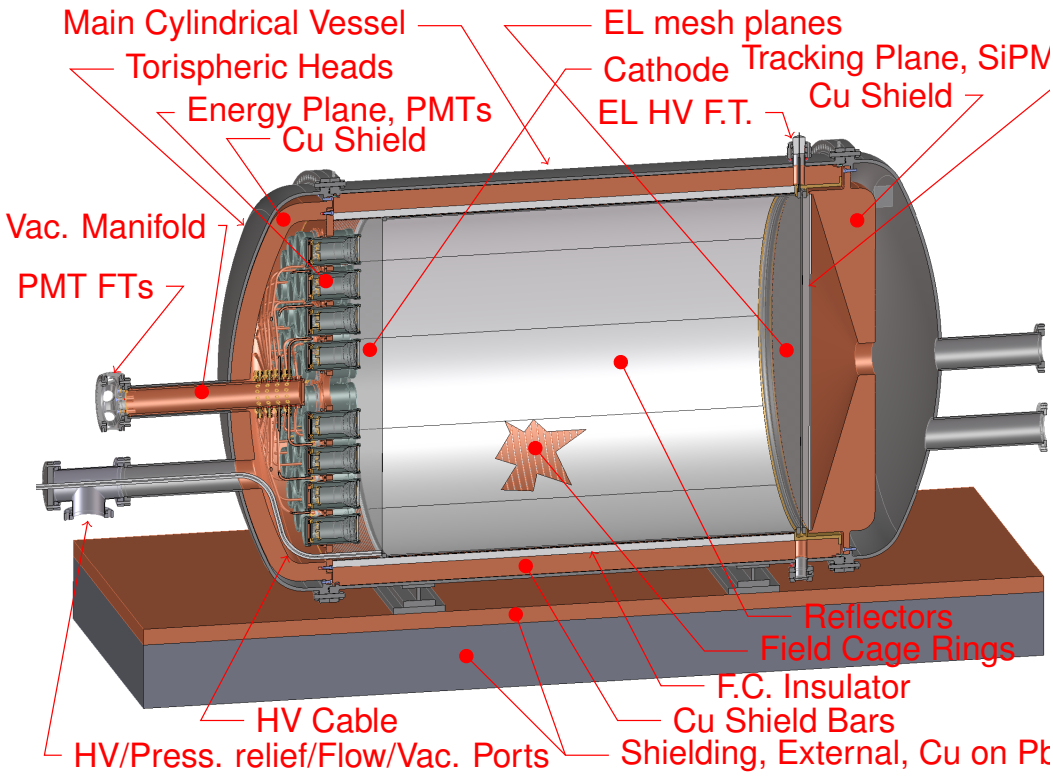

Figure 1.4: The NEXT-100 apparatus.

Figures 4.1 and Figure 4.2 show drawings of the NEXT-100 apparatus, revealing all the major subsystems. These are:

1. The pressure vessel (PV), consisting in a main cylindrical vessel and torispherical heads.
2. The inner copper shield (ICS).
3. The electrical system: field cage, cathode, EL grids and HV penetrators.
4. The light tube.
5. The energy plane made of PMTs housed in copper enclosures (cans) and connected to a vacuum manifold.
6. The tracking plane made of MPPCs arranged into dice boards (DB). The front-end electronics is inside the gas, shielded behind a thick copper plate.

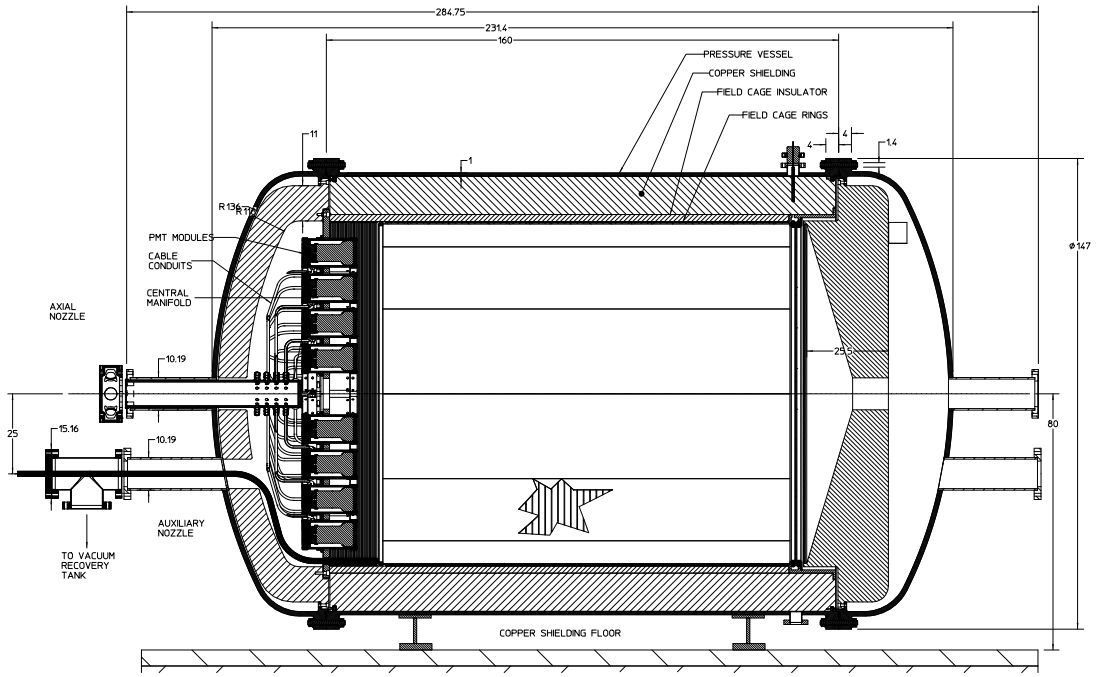

Figure 1.5: NEXT-100, longitudinal cross section

1.3.1 The pressure vessel and the inner copper shielding

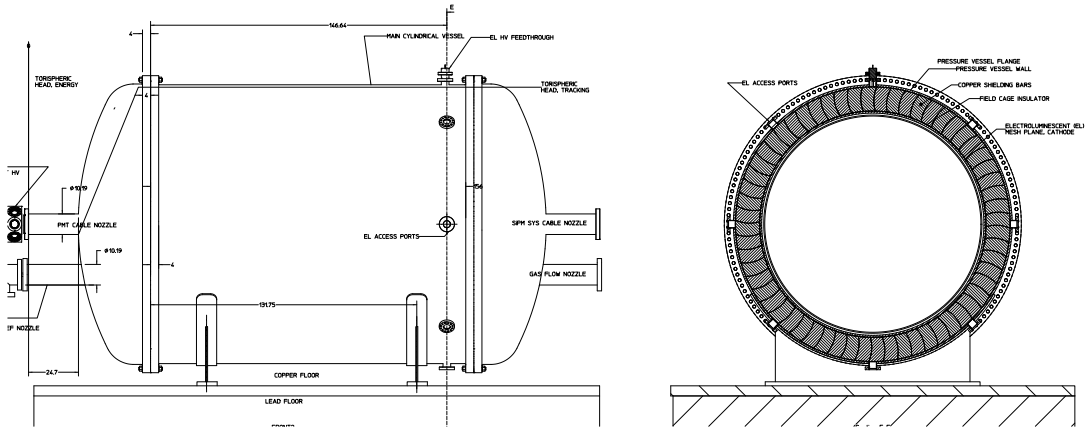

Figure 1.6: Pressure Vessel/Detector, Side and End Cross Section Views

The design of the pressure vessel (PV) has undergone significants changes and simplifications since the publication of the CDR. These are:

- Vessel design simplified.
- Vessel axis changed from vertical to horizontal
- Vessel material changed from titanium to stainless steel.
- Inner copper shield added to attenuate the background coming from the vessel and the residual background coming from the lead shield.
- PMT enclosures independent of the head.

The PV (Figure 4.2) consists of a cylindrical main section having near identical torispheric heads on each end. Both heads are convex (as viewed from outside) and each

have two nozzles, one for for services (power and signal cabling) and the other for gas flow/pressure relief. The PMT enclosures are independent from the head, and located fully inside the vessel allowing for a much simpler head design. The vessel orientation is horizontal, so as to minimize the overall height, which reduces the shielding cost and allows essentially unlimited length on each end for cabling and service expansion.

The vessel supports all internal components, and the design is quite modular; one head fully supports and contains the entire PMT system (energy plane), the other head fully supports and contains the SiPM system (tracking plane), and the main vessel fully supports and contains the field cage and mesh plane system. The drift section cathode plane high voltage feedthrough is integrated into the energy plane head and makes contact with the cathode plane when the head is assembled. The supports for these internal systems are a set of internal flanges, one incorporated into each main flange (4 total).

The simpler vessel design will significantly reduce cost, time, and risk in the fabrication; it is now very similar to a standard pressure vessel, which all qualified manufacturers will be familiar with. The decoupling of the vessel from the internal systems allows us to get an early start on the vessel fabrication, and allows for further refinement and development of these systems, should this be necessary.

The vessel material is now 304L or 316L Stainless steel. There are several reasons why we have abandoned titanium as construction material for the first version of the NEXT-100 detectors. These are:

1. Measurements of the activity of several samples of titanium, carried out by our collaboration as well as by other groups have not yield conclusive results, as shown in chapter 2. Specifically, our requirements were a maximum activity in uranium and thorium of the order of 100 μBq/kg, that would have resulted in a total PV activity of about 0.4 Bq. Contrarily to our expectations none of the measured sampled verified this condition, and most of them were found to have a level of activity 3 to 10 times larger.

2. Conversely, existing measurements of stainless steel, in particular by the XENON collaboration (see chapter 2) show that it is possible to secure SS with an activity in the range of 1-2 mBq/kg, which is of the same order than the activity measured in some titanium samples.

3. While titanium has many attractive features, including its lightness and (for some grades) its resistance to stress, it has also a number of disadvantages with respect to SS, including: (a) a much higher cost, (b) more complexity in the fabrication process that eliminated many potential manufacturers and increased the construction risks, (c) much restricted availability of parts, (d) more difficulties to accommodate the ASME standards, and (e) more difficulties for the risk assessment study, since titanium PV are way less common that SS PV.

Last, but not least, we realized that our shield design included a thick copper shield, which was essential to attenuate the residual radiation arising from the external lead

shield. On the other hand, moving the copper shield *inside* the PV has the obvious benefit of reducing the copper surface needed (thus the total mass, and therefore the cost), and in addition it attenuates the activity arising from the PV by two orders of magnitude. Consequently we decided to follow the approach taken by the XENON collaboration and fabricate a reasonably radiopure stainless steel vessel lined with an inner copper shield (ICS). The ICS is made of radiopure copper, 12 cm thick and with an activity of about 10 μBq/kg. It will attenuate the radiation coming from the external detector (including the PV and the lead shield) by a factor of 100. The ICS will be made of straight copper bars, and where relevant flat plates, which are straightforward to fabricate. It does not introduce any significant complication in the design.

It appears feasible to obtain 304L/316L stainless steel of an activity less than $\sim$5 mBq/kg in the uranium and thorium series. After the ICS the residual activity would be reduced to some 50 μBq/kg, for a total vessel mass of 1.2 tons, which is also lighter than in the titanium vessel version (in spite of the higher density of SS) due to the elimination of the heavy service flanges. Thus the residual activity due to the PV (after the ICS) is smaller than 0.1 Bq. One needs to add the residual activity of the ICS itself which is also smaller than 0.1 Bq (using copper of $\sim$10 μBq/kg, which is available from a number of suppliers, see chapter 2). Thus, the resulting activity of the whole system is smaller than that foreseen in the CDR.

Table 1.2: NEXT100 Pressure Vessel Parameters

Parameter	qty	units
Maximum Operating Pressure (MOP)	15.0	bar (abs)
Maximum Allowable Working pressure (MAWP)	16.4	bar (abs)
Minimum Allowable Pressure (external	1.5	bar (abs)
Inner diameter	130	cm
Outer Diameter, Vessel	131	cm
Outer Diameter, Flanges	147	cm
Length, inside shielding	2.22	m
Length, end to end, axial	2.85	m
Vessel and head wall thickness	10	mm
Head crown radius, internal	130	cm
Head knuckle radius, internal	13	cm
Flange thickness, head to vessel (both)	3.5	cm
Bolt Diameter, head to vessel flanges	14	mm
Bolt length, head to vessel flanges	9	cm
Number of Bolts, each head to vessel flange	150	
Mass, Vessel and both heads	1200	kg
Mass, Copper shielding	9000	kg

The basic parameters and dimensions of the pressure vessel are shown in table 4.1. The vessel will be built strictly to ASME pressure Vessel Design Code, sec VIII.

1.3.2 Field Cage

Parameter	Value
E/P	3.0 $kV*cm^{-1}*bar^{-1}$
Drift field	0.3 kV/cm
Pressure	15.0 bar
EL grid gap	0.5 cm
Drift length	127 cm
Gate grid voltage	-22.5 kV
Anode grid voltage	0
Cathode voltage	-58 kV
Optical gain	2500 photons/e^-

Table 1.3: NEXT-100 EL grid parameters

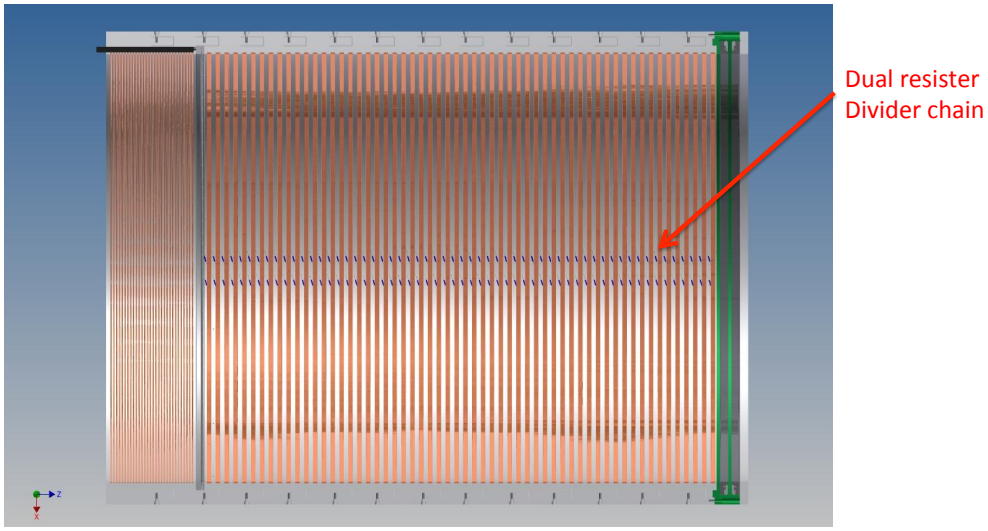

Figure 1.7: NEXT-100 Field Cage

The NEXT-100 field cage (FC) is shown in Figure 4.7 and the EL parameters are shown in Table 4.2. The main body of the FC will be a high density polyethylene (HDPE) cylindrical shell with a 2.5 cm wall thickness. The drift region will consist of OFHC copper strips connected with low background resistors. There is also a buffer region between the cathode and PMTs which will be used to degrade the high cathode voltage safely to ground. Using the parameters in Table tab.TL, the electric field varies <3% across the fiducial volume. The light tube will consist of thin sheets of Tetratex^{TM} (TTX), fixed over a 3M^{TM} substrate. The TTX will be vacuum coated with tetraphenyl

butadiene (TPB) wavelength shifter to maximize the light yield. The ArDM collaboration has measured a reflectance coefficient at 430 nm close to 97% for a wide range of coating thicknesses. In addition, the light yield measurements showed no aging effects (see chapter 7 for more details).

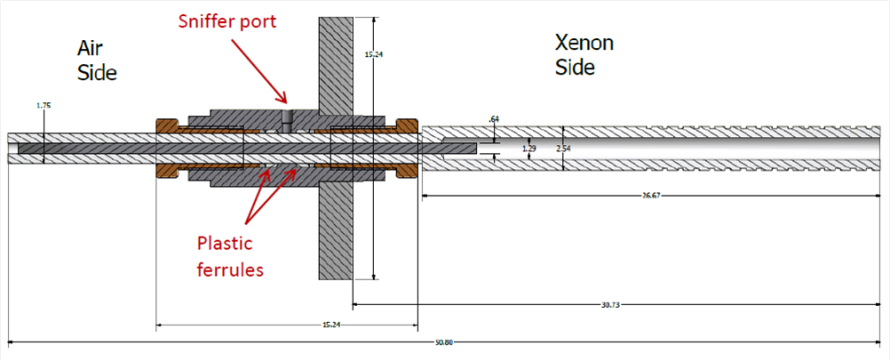

Figure 1.8: Cathode high voltage feedthrough (HVFT) designed for up to 100 kV operating voltage.

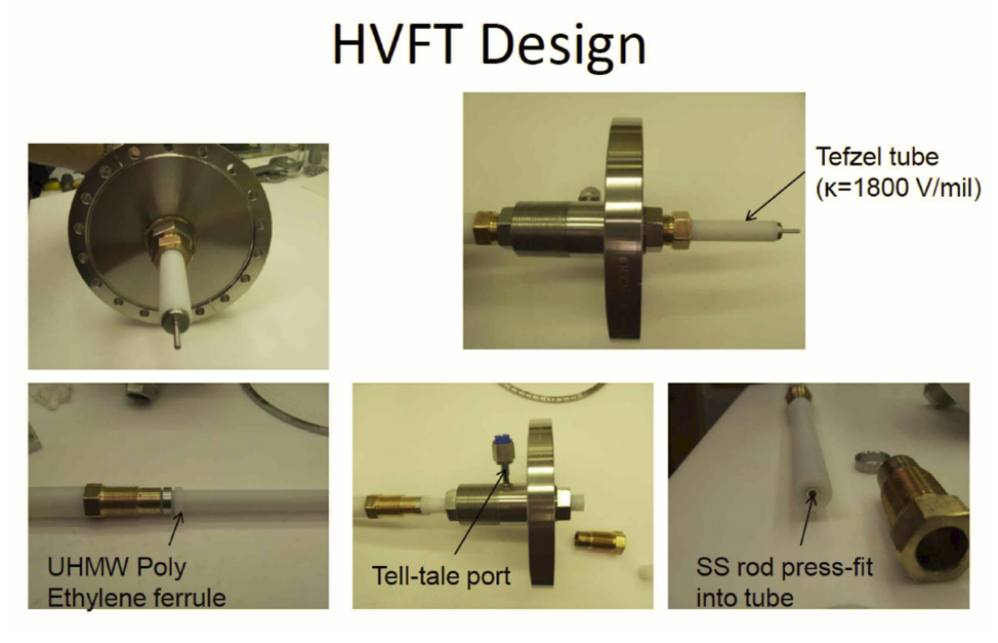

Figure 1.9: Cathode HVFT used in NEXT-DEMO.

The cathode high voltage feedthrough (HVFT) will be constructed using a compression seal approach as illustrated in Figures 4.9 and 4.10. A metal rod is pressed into a plastic tube (Tefzel or FEP, which have a high dielectric strength) which is then clamped

using plastic ferrules from both the pressure side and air side. A sniffer port is placed between the seals to assure that xenon is not leaking. The feedthrough will be attached to a flange located on the energy plane end-cap. A shielded cable will be connected to the feedthrough and placed through the PMT support plate. The unshielded portion of the cable, with an additional resistive coating, will then run along the inside of the buffer field rings and mate with the cathode via a spring loaded junction. This approach, with the exception of the resistive coating, has been used in NEXT-DEMO, where a cathode voltage of 45 kV has been achieved. A smaller prototype was tested to 100 kV in vacuum and 70 kV in nitrogen at 3 bar. It has been demonstrated to be leak tight at 10 bar xenon and 10^{-7} mbar vacuum.

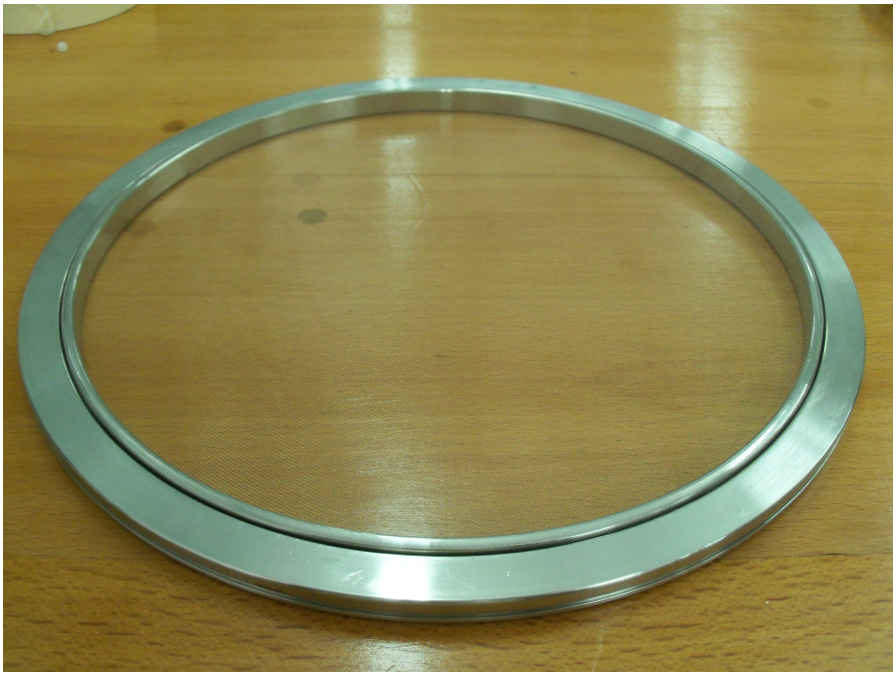

Figure 1.10: EL grids used in NEXT-DEMO

Figure 1.10 shows the electroluminescent (EL) grids built for the NEXT-DEMO prototype. The grids were constructed using a stainless steel mesh with pitch 0.5 mm and wire diameter 30 microns, which results in an open area of 88%. The grids are formed by clamping in a ring with a tongue and groove to hold the mesh and using a tensioning ring that is torqued with set screws to achieve the optimum tension. One important issue is that for the large diameter required in NEXT-100, preliminary estimates show that electrostatic attraction will cause the EL grids to bow considerably. This can be remedied by using a larger gauge wire. For example, a wire mesh is available with 90 micron wire diameter made from titanium with a similar open area. We are also investigating the use of titanium or copper grid frames to minimize the radioactive budget.

1.3.3 The energy plane

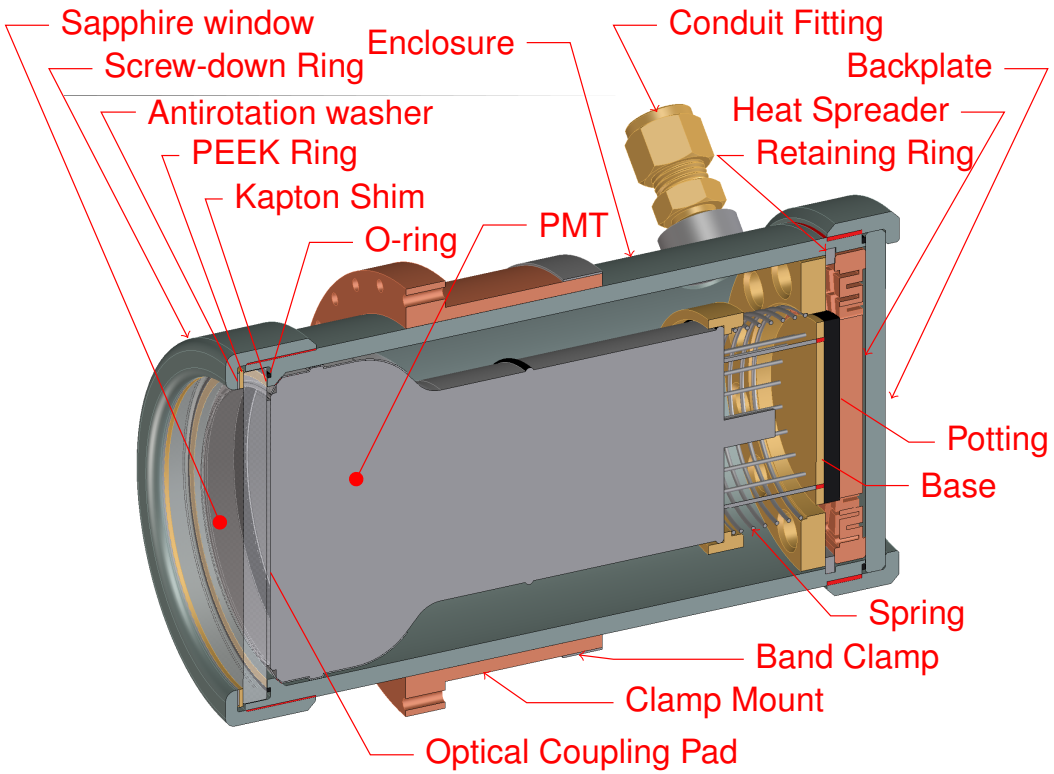

Figure 1.11: A PMT inside its enclosure.

The energy measurement will be provided by the detection of EL light via PMTs, which will also record the scintillation light needed for t_0. Those PMTs will be located behind a transparent cathode. The energy plane (Figure 5.5) includes the following elements:

- A total of 60 low-background, high-QE PMTs, model R11410-10 from Hamamatsu. (Figure 5.1), covering 32.5% of the cathode area. These are large tubes, with a 3" photocathode and low levels of activity of the order of 3 mBq per unit in the Uranium and 2 mBq per unit in the Thorium series, the only relevant backgrounds for NEXT (Figure 5.2). The QE of the R11410-10 model is around 25% both in the VUV and in the blue region (Figure 5.3). The PMT coverage is 30%, enough to guarantee detection of S1 in most of the energy spectrum and to measure the energy with good resolution (see chapter 5).

- PMTs are sealed into individual pressure resistant, vacuum tight titanium enclosures. These enclosures (a.k.a. *cans*) are shown in Figure 5.4. The concept is

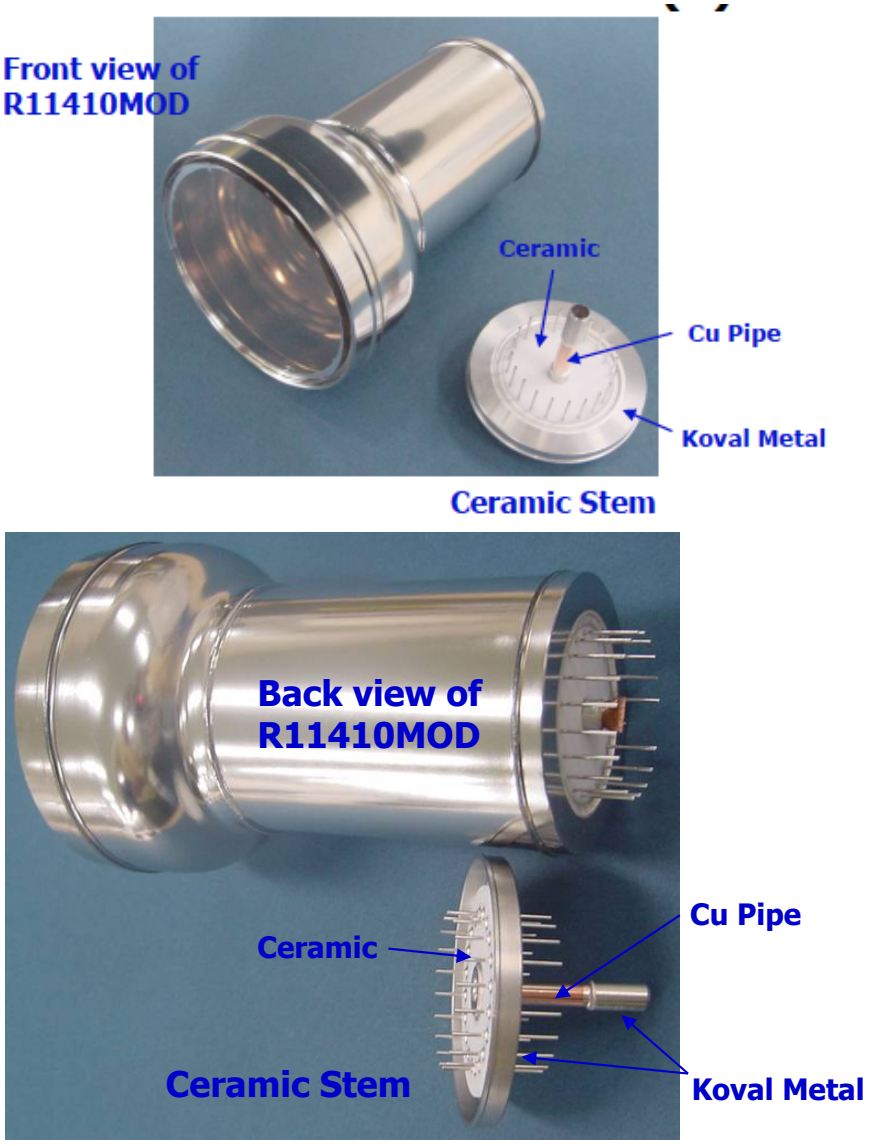

Figure 1.12: The Hamamatsu R11410-10 phototube. This is a large PMT, 3" in diameter, with an average radioactivity of 3.3 mBq for the U chain and 2.3 mBq for the Th chain.

RI Level for R11410MOD

Estimated RI level

< Unit : mBq/PMT >

Materials	Weight (g)	40K	U	Th	Co60	Sub Total
Quartz Faceplate	35	0.0	0.2	0.4	0.1	0.7
Metal Bulb	95	5.7	2.9	1.0	3.5	13.1
Stem (ceramic)	25	0.0	0.0	0.7	5.5	6.2
Insulating Plates	16	0.0	0.1	0.2	0.0	0.3
Electrodes	31	0.0	0.1	0.0	0.0	0.1
Total	202	5.7	3.3	2.3	9.1	20.4

Expected RI level : 10~30 mBq/PMT

Figure 1.13: Activity of the R11410-10 phototube.

Typical QE Curve

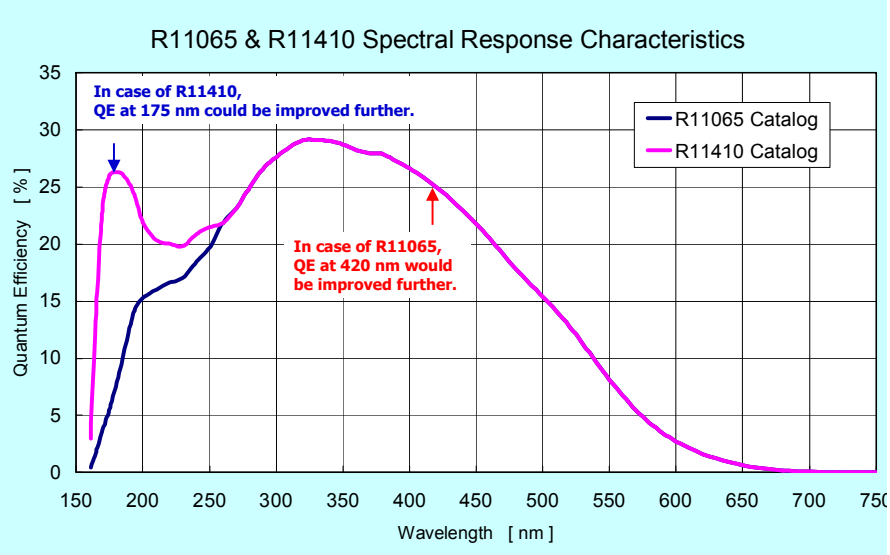

Figure 1.14: QE of the R11410-10 phototube.

similar to that shown in the CDR. but they are no longer welded into the torispheric head as in the original design. Instead, both the pressure vessel and the PMT system are simplified by moving the enclosures fully inside the vessel. This allows the PMT system to be developed independently of the vessel.

- The PMT cans are all mounted to a common carrier plate that attaches to an internal flange of the pressure vessel head.
- Sapphire windows are secured with titanium screw-down rings and O-ring sealed to the front end of the enclosure. A similar system seals the back side of the enclosure
- PMT bases are potted with heat conducting epoxy to flexible copper heat spreaders which connect to the enclosures.
- PMT cables are enclosed in individual pressure resistant,vacuum tight tubing conduits.
- Conduits all lead to a central manifold. The central manifold is cantilevered from the nozzle flange.
- PMT cables route through central manifold to 41 pin CF feedthroughs on a CF octagon, outside the lead shielding.
- High vacuum($< 10^{-6}$ torr) is applied at octagon port; good vacuum ($< 10^{-4}$ torr) is maintained inside enclosures through conduits, well below Paschen minimum, avoiding sparkover or glow discharge across PMT pins.
- A large vacuum tank buffer volume exists to limit pressure build in central manifold in case of sapphire window failure (avoids Super-K chain reaction failure mode). Xenon permeation through seals is recovered with a cold trap.
- Vacuum inside enclosure requires good thermal management, base cooling is by conduction into enclosure through a special low force heat spreader plate.
- PMT Modules are clamped into copper heat conduction flanges attached to the copper carrier plate.
- Heat is carried to pressure vessel flange by conduction through copper carrier plate; 7 C total temp rise.
- Carrier plate and central manifold can be electrically (but not thermally) isolated from the pressure vessel, to allow the PMTs to be operated with cathodes at full negative voltage, with anodes and signals at low voltage
- Alternately, the cathodes can be grounded, and the anodes and signal run at high positive voltage using only the central 21 pins of each 41 pin feedthrough, to avoid flashover.

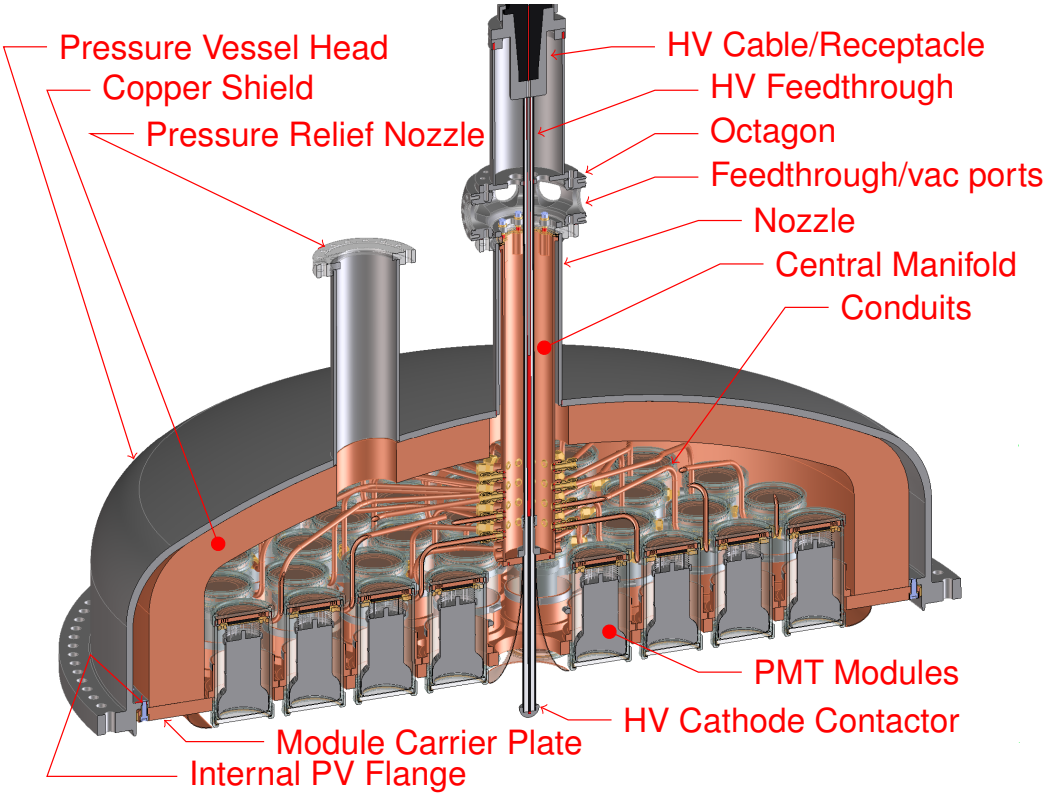

Figure 1.15: The full energy plane.

1.3.4 The tracking plane

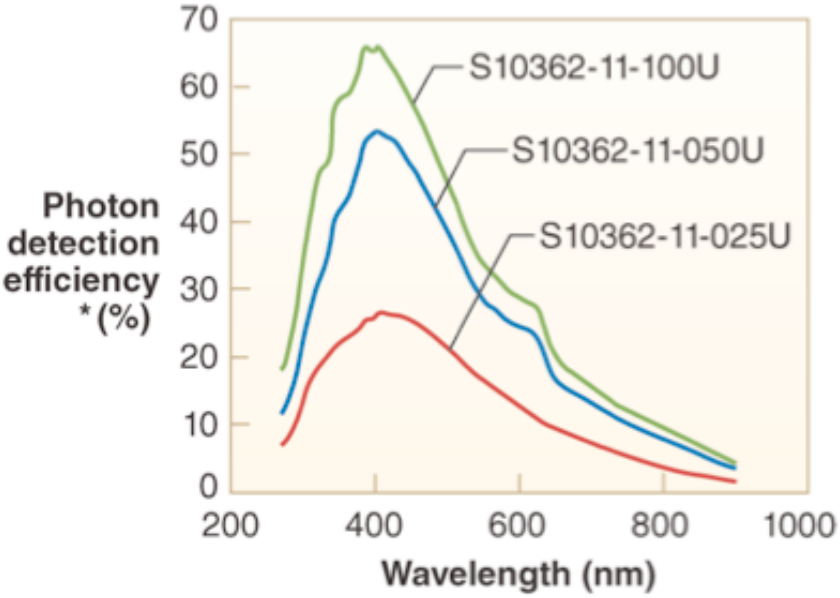

Figure 1.16: The Photon Detection Efficiency as a function of the wavelength of the incident light for the two MPPC models considered in NEXT. The S10362-11-025P has been used in NEXT1-TF. The S10362-11-050P will be used in NEXT100.

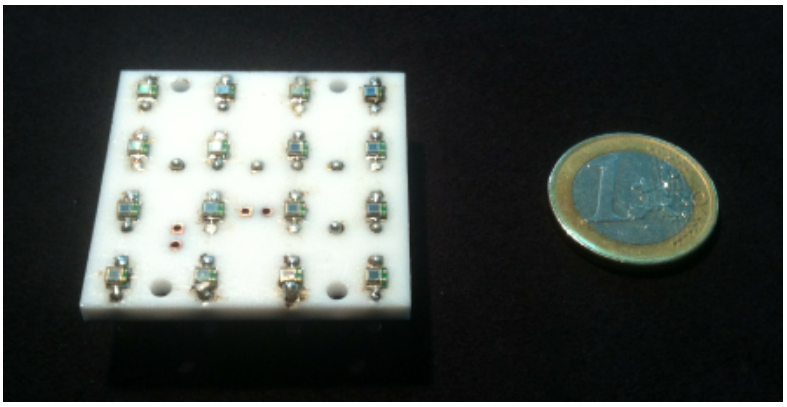

Figure 1.17: Dice Board containing 16 (4×4) MPPCs

In NEXT the tracking function is provided by a plane of multi-pixel photon counters (MPPCs) operating as a light-pixels and located behind the transparent EL grids. The MPPCs will be manufactured by Hamamatsu and the chosen model is S10362-11-050P. This small device has an area of 1mm^2, 400 pixels per sensor and very large particle

detection efficiency (PDE) in the blue region (Figure 1.16). It is very cost effective (less than 12.5 euros per unit for large orders) and its activity is expected to be low, given its composition (mainly silica) and very light mass.

The MPPCs will be mounted in Dice Boards (DB). This are square boards made of *cuflon* (PTFE fixed to a copper back plane). Figure 5.7 shows on of the DB of the NEXT-DEMO prototype, each one holding 4×4 pixels. NEXT-100 DB will be similar, but containing 8×8 pixels.

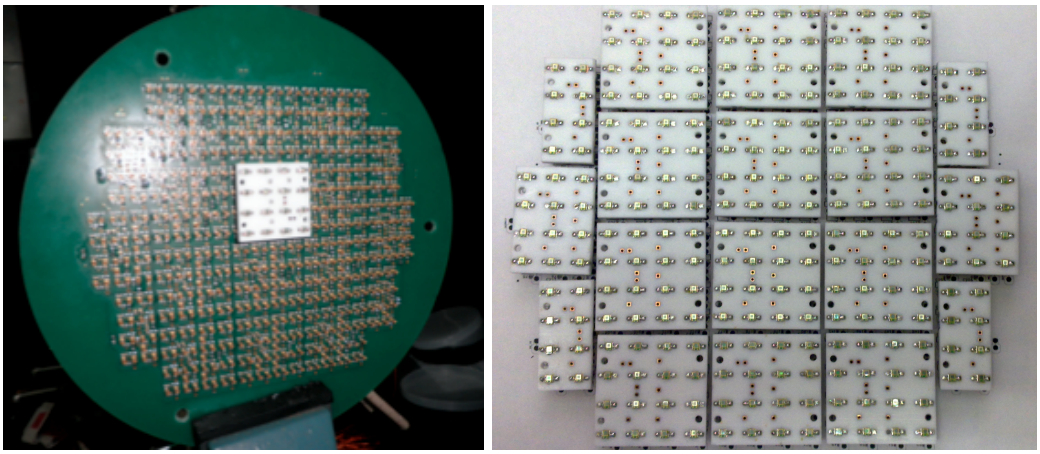

Figure 1.18: Left: Mother-Board with the front-end electronics on which center one of the Daughter-Boards is connected. Right: MPPCs DB arranged following the structure of NEXT-DEMO tracking plane.

In NEXT-DEMO, the DB are fixed to a Mother Board (MB) (Figure 5.8). In NEXT-100, the DB will be fixed to a light honeycomb structure and connected directly to the FE electronics. Each DB is supplied with a common bias voltage.

A dedicated setup was prepared to to measure the spread in gain of every single DB. As shown in Figure 5.10, spread in gain in every DB keep always below 4%, while the average in gain is (2.27 - 2.50) 10^5. These values provide a homogeneous response of the plane, and ensure the correct resolution for the reconstruction of $\beta\beta$ events.

Figure 5.11 shows the typical dark current measured in our MPPCs as a function of the bias voltage and for three different temperatures. The level of the dark current is at about 5 photoelectrons. In NEXT-100 a digital threshold at the 4 - 6 p.e. level should lead to an insignificant noise rate. An automatic system to compensate temperature differences by adjusting the bias voltage has also been tested successfully and will be implemented in NEXT-100.

The pitch of the NEXT-100 tracking planes is a compromise between several constrains imposed by the physics:

1. An electron moving in dense gas does not behave exactly as a minimum ionizing particle. Instead, it loses a significant part of its energy by the emission of discreet

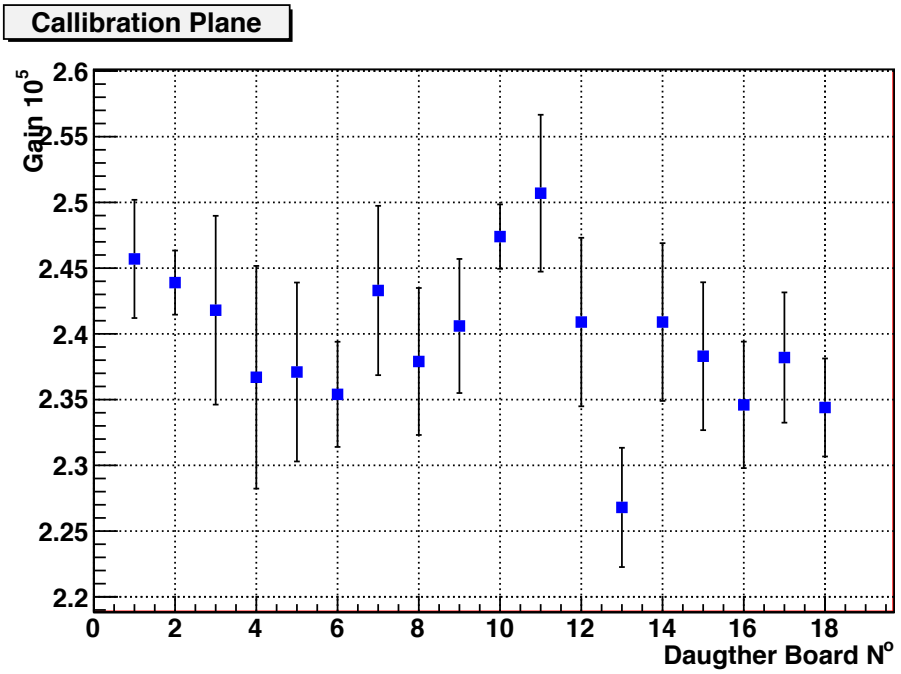

Figure 1.19: Values of Average and Spread in Gain of every Daughter Board.

delta rays and bremsstrahlung radiation. The "photon cloud" associated to the electron has an rms distribution of the order of 1 cm.

2. Transverse diffusion in pure xenon is large, and the typical rms of the charge distribution for electrons produced in the center of the chamber is of the order of 1 cm.

3. Identifying low-energy photons (e.g, x-rays of 35 keV) nearby the electron track is an extra handle to label background events (e.g, photoelectric events in the ^{214}Bi peak). Photon-track separation is directly proportional to pitch.

A pitch significantly smaller than 1 cm is not useful due to charge dispersion and the photon cloud. Conversely, as the pitch increases the background rejection capability decreases. Monte Carlo studies show that a reasonable tradeoff may be found for pitches between 1 cm and 1.5 cm. While physics performance appears not to degrade too much with pitch in that region, the number of pixels decreases with the square of the pitch. A reasonable compromise appears to be 1.1 cm, which in turn requires about 7 000 pixels.

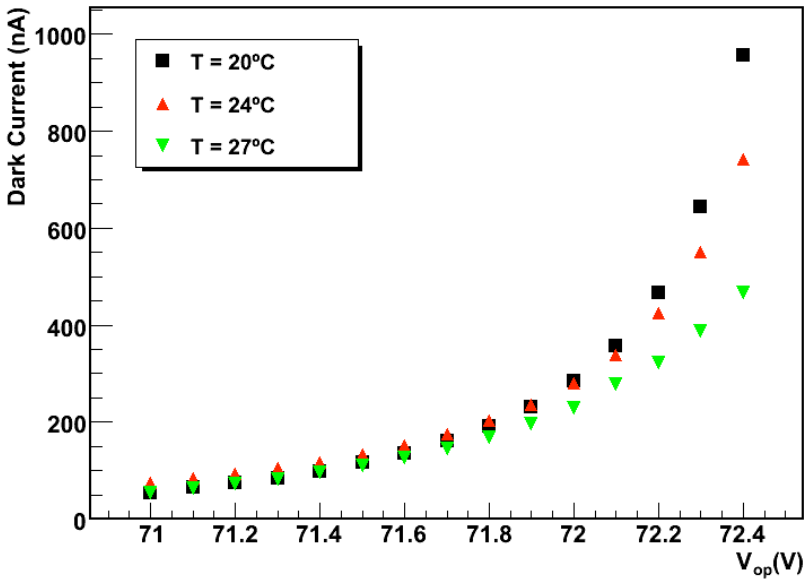

Figure 1.20: Dark current of one NEXT MPPC as a function of operative voltage and for three different temperatures T.

1.4 Front-end electronics

1.4.1 FE readout electronics for the PMTs

The FE electronics for the PMTs in NEXT-100 will be very similar to the one developed for the NEXT-DEMO and NEXT-DBDM prototypes. The first step is to shape and filter the fast signals produced by the PMTs (less than 5 ns wide) to match the digitizer and eliminate the high frequency noise. An integrator is implemented by simply adding a capacitor and a resistor to the PMT base. The charge integration capacitor shunting the anode lengthens the pulse and reduces the primary signal peak voltage accordingly. The integrating signal is then fed to a low-pass filter amplifier.

The design, shown in Figure 6.1 uses a single amplification stage based on the fully differential amplifier THS4511, which features low noise ($2\text{nV}/\sqrt{\text{Hz}}$) and provides enough gain to compensate for the attenuation in the following stage, based on a passive RC filter with a cut frequency of 800 kHz. This filtering produces enough signal stretching to allow taking many samples per single photo-electron at 40MHz.

The front-end circuit was implemented in 7 channel boards (Figure 6.3) and connected via HDMI cables to 12-bit 40-MHz digitizer cards. These digitizers are read out by FPGA-based DAQ modules that buffer, format and send event fragments to the DAQ PCs via gigabit Ethernet links.

Both the 16-channel digitizer card and the DAQ module (Front-End Concentrator,

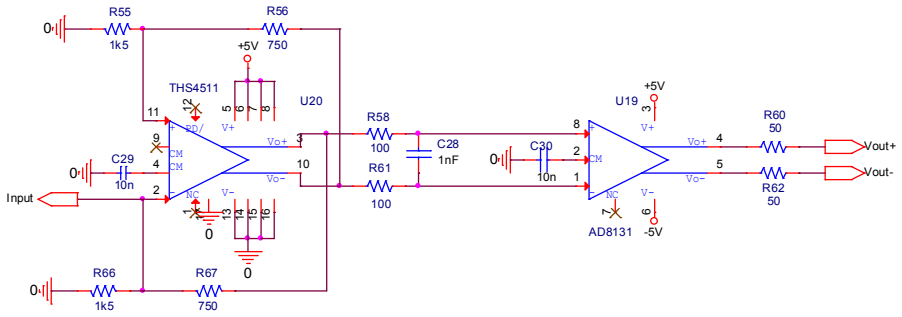

Figure 1.21: FE electronics schematics for one channel of the energy plane of NEXT-DEMO. A similar scheme will be implemented for NEXT-100.

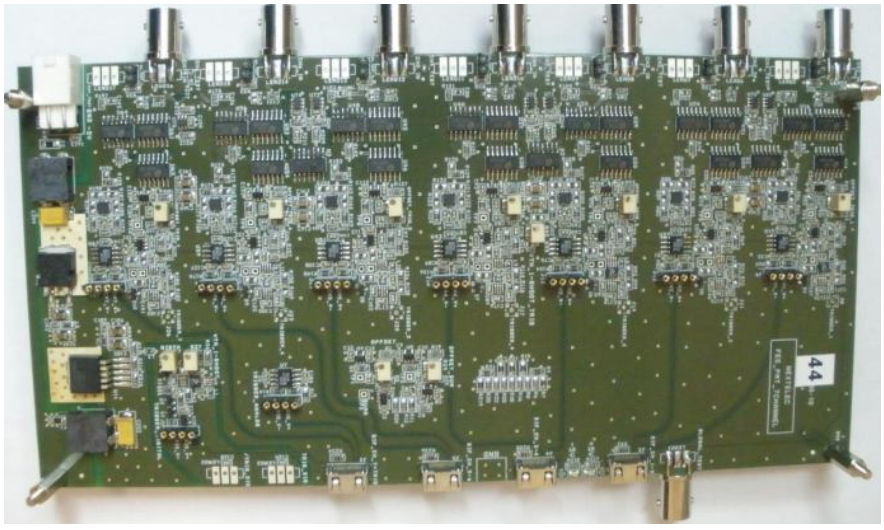

Figure 1.22: NEXT-DEMO front-end card with 7 analog channels.

FEC) have been designed as a joint effort between CERN and the NEXT collaboration in the framework of the Scalable Readout System (SRS) for the RD51 R&D program, as describe in our CDR. These two cards are edge mounted to form a standard 6U×220 mm eurocard. The FEC module can interface different kinds of front-end electronics by using the appropriate plug-in card.

An additional FEC module with a different plug-in card is used as trigger module. Besides forwarding a common clock and commands to all the DAQ modules, it receives trigger candidates from the DAQ modules, runs a trigger algorithm in the FPGA and distributes a trigger signal.

Up to two front-end cards can be read out by a single DAQ module through an ADC card. This readout system can be easily scaled up by simple addition of FEC cards.

To summarize, a low noise differential amplifier is used to obtain good resolution in the digitization of the primary scintillation, which provides high detection efficiency. The energy resolution of the front-end circuit using test input signals with charge values close to the ones expected from EL signals is of the order of 0.26%, which will provide precise energy measurement of the EL events in the TPC. The solution adopted for the DAQ system guarantees the scalability of the system for NEXT-100.

1.4.2 FE electronics and readout for NEXT-100 tracking plane

The collaboration has gained considerable experience in the design of FE electronics for the tracking plane with the design and construction of the FE electronics for the tracking plane of the NEXT-DEMO prototype (see chapter 6). The main problem to be addressed in the case of the NEXT-100 detector is the fact that it will have more than 7 000 channels. Passing all those wires across feedthroughs, as it has been done for NEXT-DEMO is possible but challenging and probably not optimal. Consequently we are developing a new in-vessel FE electronics that reduces the total number of feedthroughs to an acceptable level. Here we present the new electronics readout architecture.

Since the electronics will be inside the PV, it must necessarily be very low power to minimize the heat dissipated inside the vessel. The very front-end design and the ADCs are the key to low power.

Our design consists of a very simple front-end, very low power ADCs and a digital data merger stage (FPGA) to be placed inside the detector. This is achieved by replacing the gated integrator with a passive RC circuit and the power-hungry amplifiers with ultra low power devices. A preliminary estimation gives a total of 240 W. Additional power dissipation comes from drop in voltage regulators, FPGA (data handling and multiplexing) and transmission circuits required to reduce the number of feedthroughs in the TPC vessel. We estimate a total in-vessel electronics is 410 W.

To efficiently dissipate this heat we will attach the front-end cards to 10-cm-long copper fins radially mounted on the inner vessel surface. Since xenon is a bad heat conductor, most of the heat will be transferred from the fins to the vessel. A cooling circuit surrounding the detector would define an appropriate, constant vessel temperature. Simulations need to be carried out to validate how much power can be dissipated with this solution. Alternatively, liquid cooling inside the vessel could be used.

Taking the NEXT-DEMO electronics as a starting point, we have designed a three-stage circuit, with a gain of 10 in each stage. The first two stages are based on the AD8012 (two amplifiers per package, very low noise) and the last one on the AD8005 (ultra low power, 400 μA quiescent current). Total gain is (Rt is the input termination resistance) $1.000 \times Rt = 50.000$, as the first stage is a transimpedance amplifier with gain of $10 \times Rt = 500$. A passive, 2 μs time-constant RC circuit (200 pF, 10 kΩ between the second and the third stages acts as the circuit integrator.

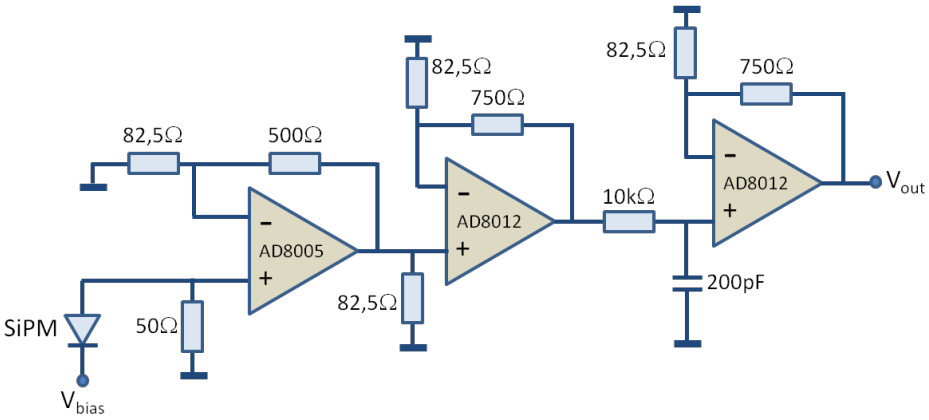

Figure 1.23: This low power amplifier circuit for NEXT100 features only approx. 30 mW power, 4mV/pe gain and 1.7mV rms noise

This gain will suffice to produce a 1V output for a 250-pe dynamic range. Total electronic noise in the amplifier circuit is very low according to the simulations: 1,7 mV rms. This is approx. 3 LSBs in a 12-bit ADC and sets the limit to the offset voltage adjustment. For the digitization two alternatives are currently under study:

- A single-channel 1-to-3 MHz low-power 12-bit ADCs (like AD7476), requiring only two lines (data and chip select) for readout. This solution is used in NEXT-DEMO. Total power dissipation (including amplifier and ADC) is approx. 35 mW per channel (a factor 18 less than the NEXT-DEMO solution). This value goes up to 60 mW after a conservative estimation for losses in voltage regulators and other auxiliary circuits (including FPGA readout and data transmission).

- A fast (40 MHz or higher) multi-channel ADC and an analog switch for multiplexing. This solution can lead to a reduced power consumption, though the effect of the noise induced by hundreds of switches inside the vessel has to be studied.

The readout will be triggered and zero suppressed. Our expected operational parameters (chapter 6) are a10 Hz trigger rate, 2 ms event size and 1 MHz sampling frequency. For these parameters a triggered readout produces 50 times less throughput than a continuous readout. 7 000 channels produce approx. 20 MByte/event in raw data mode. At 10 Hz rate this makes 200 MByte/s data, or 1,6 Gb/s throughput.

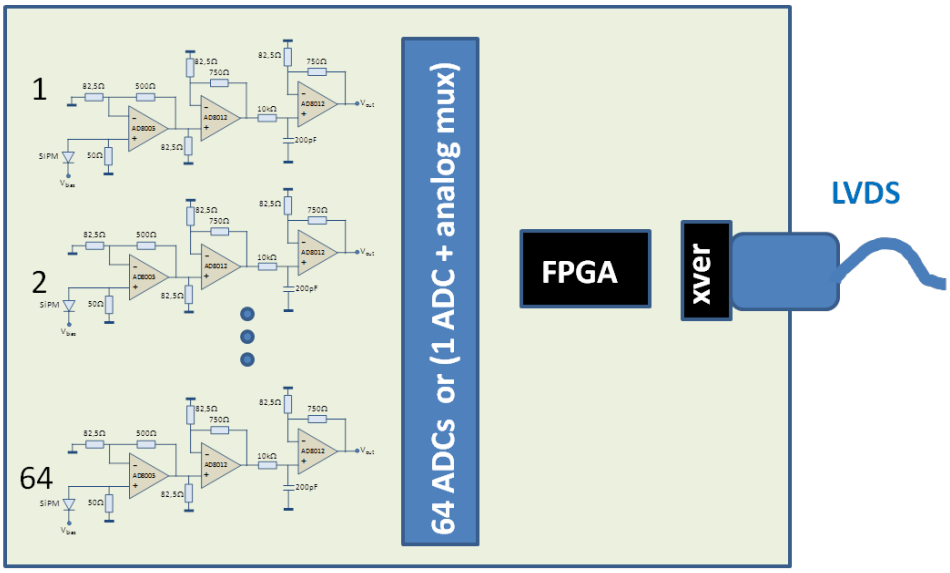

Figure 1.24: Functional blocks in the FEB card

These three conclusions suggest a readout architecture sketched next.

Consider a NEXT-100 DB with an 8×8 SiPM array. These DB cards equip the bias network and a few (maybe 4) connectors for low-cosstalk kapton ribbon cables. These cables arrive in a Front-End Board (FEB) that includes the analog stages, ADC converters, voltage regulators and an FPGA that handles, formats, buffers and transmits data to the outer DAQ. LVDS clock and trigger inputs are needed.

This 64-ch FEB is the key component in the in-vessel electronics. A total of 107 FEBs are required. FEB size can be 15×15 cm, leaving 3.5 cm^2 board area per channel. This can easily accommodate the three amplifying stages and ADC per channel plus associated SMD passive components in one board side. The FPGA, voltage regulators and I/O connectors can sit in the opposite layer.

Power dissipation (as calculated in previous sections) is 60 mW per channel, or 3.84W/FEB (64 channels). The FEB plane will dissipate approx. $107 \times 384\text{W} = 410$ W.

One full event (2 000 samples) requires $2.000 \times 64 \times 12$ bit, slightly more than 1,5 Mbit (or 187,5 KByte). This is a first estimation for the size of the data buffer. It is available as true dual-ported memory in low-power FPGAs like Spartan-6 LX45 in 324-BGA (15×15mm) or in the low power, low cost, Xilinx Artix XC7A30T. Therefore no external memory is required.

Data are stored in a circular (ring) buffer in the FEB. Storing 1,5 Mbit data in 2 ms requires writing the buffer at 750 Mb/s. After framing, reading out at 200 Mb/s (maybe a limit for copper links across a vacuum feedthrough) takes 7,5 ms. So, from the 100 ms period (1/10Hz) the system spends in worst case 2 ms filling the buffer and 7.5 ms emptying it.

For zero-dead-time operation the buffer must be large enough to be continuously

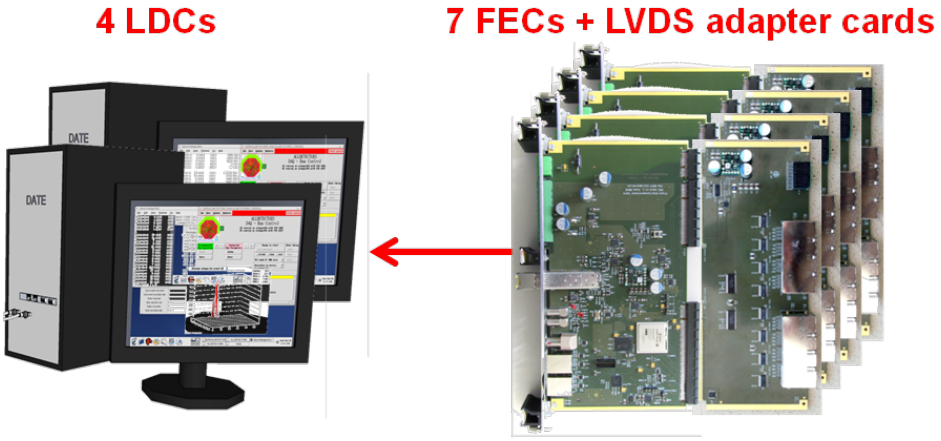

Figure 1.25: The NEXT-100 SiPM plane can be read out with 4 LDCs and 7 FECs

filled, and so a 2+7,5= aprox. 10 ms buffer is needed. This means 1,5Mbit×10ms/2ms = 7,5 Mbit. This is still feasible with Xilinx Artix FPGAs (XC7A200T), that has an internal 13,5 Mbit memory. A trade-off between readout speed and buffer size must be found in order to minimize cost and power. Data links must a have a low speed for the sake of reduced power consumption, cheaper electronics, reduced FEB noise and enhanced signal integrity.

The FEB output frame format can be an evolution for the existing NEXT1 SiPM format. We propose to use a 16-bit word format. An event will be split into a number of frames containing each: SOF (start of frame), Board ID (unique FEB ID number), a number of data blocks, a CRC word and an EOF (End of Frame) word. Each data block contains a Timestamp word (including error flags) and 64 data words.

With a tentative number of data blocks per frame of 10, this makes 644 words per frame, or 10 304 bits. An event containing a maximum of 200 frames has a size of slightly less than 2 Mb.

In order to transfer these data in 10 ms (requiring 12 ms buffer in the FPGA), we need a link speed of 200 Mb/s. This is again a compromise between buffer size and link speed, and the sweep spot must be found.

If zero-dead-time operation is not required, operating at a 10 Hz rate, the required link throughput would be just 20 Mb/s.

Careful evaluation of copper and optical link solutions will provide the right compromise between buffer size, power dissipation, reliability and cost.

The DAQ will follow the modular architecture described in the CDR. The number of Front End Cards (FECs) and local data concentrators (LDC) PCs is determined by two numbers:

1. The tracking plane produces 1.6 Gb/s data. Setting a comfortable working point for the gigabit Ethernet links between the FECs and the LDCs in 400 Mb/s, 4 LDCs are required.

2. Assuming 200 Mb/s link speed (LVDS over copper) from the in-vessel electronics to the DAQ (the same speed and technology used in NEXT1 for the SiPM plane readout) the existing 16-link LVDS adapter card can be used. The 107 links coming from the vessel require then 107/16=7 FEC cards.

Combining these two points, one needs 7 FECs and 4 LDCs as the size of the tracking DAQ partition. This is approx. the size of the full NEXT1 DAQ.

1.5 Shifting the VUV light for NEXT

Xenon scintillates in the VUV range, with a peak at ∼175 nm. Although the NEXT PMTs have the same QE for light in this range and in the blue (about 25%), the MPPCs have a very low PDE below 200 nm. Therefore, it is imperative to use a wavelength shifter (WLS) on MPPCs. Furthermore, the reflectivity of the light tube (made of TTX, a Teflon cloth) is dramatically improved by coating the TTX with TPB. Last, but not least, our PMTs will be enclosed in cans coupled to the gas through sapphire windows. UV grade sapphire is extremely expensive, and thus coating the sapphire windows of the PMT enclosures with PMT appears also as mandatory.

Tetraphenyl-butadiene (TPB) of $\geq 99\%$ purity grade is an organic WLS widely used in many experiments to shift scintillation light produced in the UV by Liquid Argon or Liquid Xenon to the visible. It absorbs light in a wide UV range and re-emits it in the blue with an emission peak around 430 nm. TPB can be applied by vacuum evaporation from crystalline form directly onto surfaces. The TPB coating obtained that way is reported to be hard and durable with good adherence to the substrate and high resistance to mechanical abrasion. It is not soluble in water but may be degraded by humidity, and can be removed when necessary by the use of benzene or other organic solvents.

A TPB procedure to deposit a thin layer of TPC on flat (relatively small) surfaces, such as dice boards (DBs) and the sapphire windows of the PMT cans has been developed at ICMOL and IFIC. A second procedure to coat large surfaces, such as the NEXT-100 light tube has also been developed at IFIC.

The technique to deposit thin layers in flat surfaces —including glass, quartz, sapphire and teflon— has been developed at the coating facility of the Instituto de Ciencias de Materiales (ICMOL). Figure 7.1 shows the evaporator used. It is enclosed in a glove-chamber filled with with N_2 to insures the conservation of the organic compounds by avoiding their oxidation and hydration. The coating setup consists in a vacuum chamber enclosing 4 ceramic crucibles used to contain and melt simultaneously up to 4 compounds. During the TPB evaporation campaign for NEXT the whole setup was cleaned to remove any traces of other molecules. One crucible only was used and filled with TPB pounder. It was heated by a cartridge with an adjustable current for monitoring the temperature and controlling the evaporation rate to avoid bubbling and sputtering of the TPB onto the exposed substrate.

Several successive depositions of a chosen thickness have been successfully produced

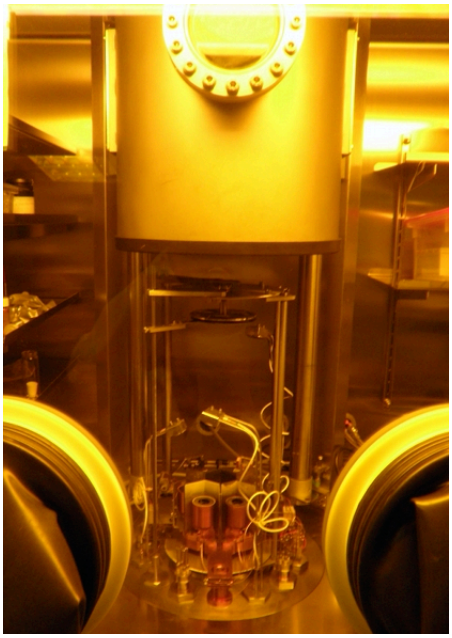

Figure 1.26: The Evaporator where one can distinguish from bottom to top, the crucibles and the deposition-sensors, the shutter, the sample-holder supported by a spinning disk and the vacuum chamber which is closed down during evacuation and coating.

on TiO_2 glass-slices and on several samples of MPPC dice boards. As an illustration, Figure 7.3 shows a glass-slice (left) and a prototype DB (right) coated with TPB and illuminated with UV light at 240 nm, clearly re-emitting in the blue. The coated glass-slices and DB samples have been tested and characterized at IFIC and ICMOL with different UV light sources. Some of the most relevant results are described in the following subsections (a detailed paper with more extensive details will be published shortly).

The light tube will cover the inner part of the field cage. The presence of a strong electric field demands, therefore, non conductive material as the substrate for the wavelength shifter. We have chosen the same materials studied by the ArDm collaboartion. The light tube substrate will be ESR (Vikuiti^TM Enhanced Specular Reflector foil) from the company 3M^TM and Tetratex (TTX)from the company Donaldson Membranes. The ESR foil is a multilayer specular reflecting polymer measured to be highly radiopure. Its appearance is that of a polished metal although the material is non conducting. It has a specular reflection coefficient of practically 100% in a large region of the optical spectrum. TTX is an aligned polytetrafluoroethylene (PTFE) fibrous cloth and is nearly a 100% diffuse Lambertian reflector. It is also radiopure (typically less than 1 ppb, which, given the very low mass involved, gives a negligible contribution to the radioactive budget) and has low degassing. The measured reflectivity of the ESR + TTX foils is about 97% at 430 nm.

The NEXT collaboration has acquired the large evaporation chamber developed by

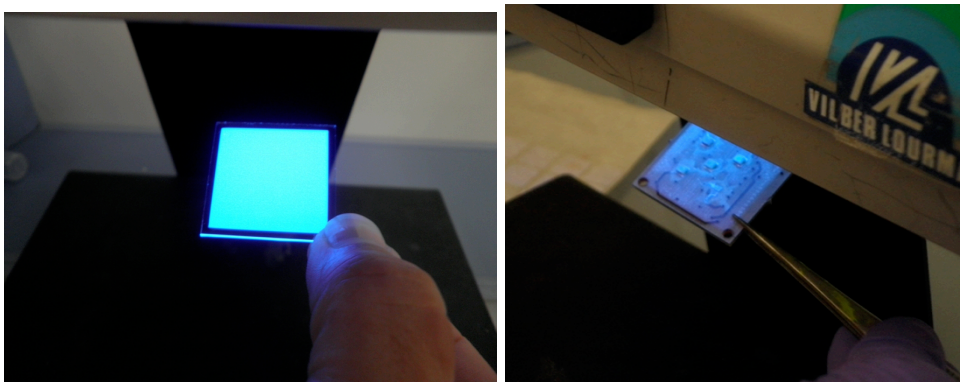

Figure 1.27: Illumination with 240 nm UV light of a glass-slice (left) and a 5-SiPM board (right) both coated with TPB.

Figure 1.28: The large evaporation chamber, details.

the ArDM collaboration, which is currently installed at the IFIC (Figure 7.9). This is a stainless steel vacuum chamber large enough to house reflector sheets of 120×25 cm^2 which have the right size for the NEXT-100 detector. The apparatus consists mainly of two parts, a horizontal tube with pumping connection on its closed end and a slide-

Figure 1.29: Response of the light tube foil (ESR+TTX) after coating, showing the characteristic blue light emission when illuminated by a UV lamp. In the upper part of the picture the same foil without coating.

in array of 13 crucibles mounted onto a Viton-sealed access flange. The crucibles are electrically connected in series for better uniformity and lower total supply current (10A). The reflector sheets are supported by 100μm wires in a crescent arrangement for constant distance to the crucibles. An evaporation cycle is started by filling the crucibles with TPB powder and positioning the TTX reflector sheet on its support.

After this preparation the sheets were inspected optically with a UV lamp (Figure 7.10) showing the characteristic re-emission in the blue.

1.6 The gas system

The pressure vessel/gas system must be capable of pressurizing, circulating, purifying, and depressurizing the detector with either enriched xenon (EXe), normal xenon (NXe), depleted xenon (DXe) argon and possibly other gases with negligible loss, and without damage to the detector. There is a high priority on avoiding loss of EXe, due to its cost and availability. A list of requirements in approximate decreasing order of importance is shown below:

1. Pressurize vessel, vacuum to 15 bar absolute (bara) - 1 hour max. - EXe, DXe, Ar

2. Depressurize vessel, on fault command, 15 bar to 1 bar - 10 sec max. - to closed reclamation system

3. Depressurize vessel, normal operation, 15 bar to vac. - 1 hour max. - to closed reclamation system

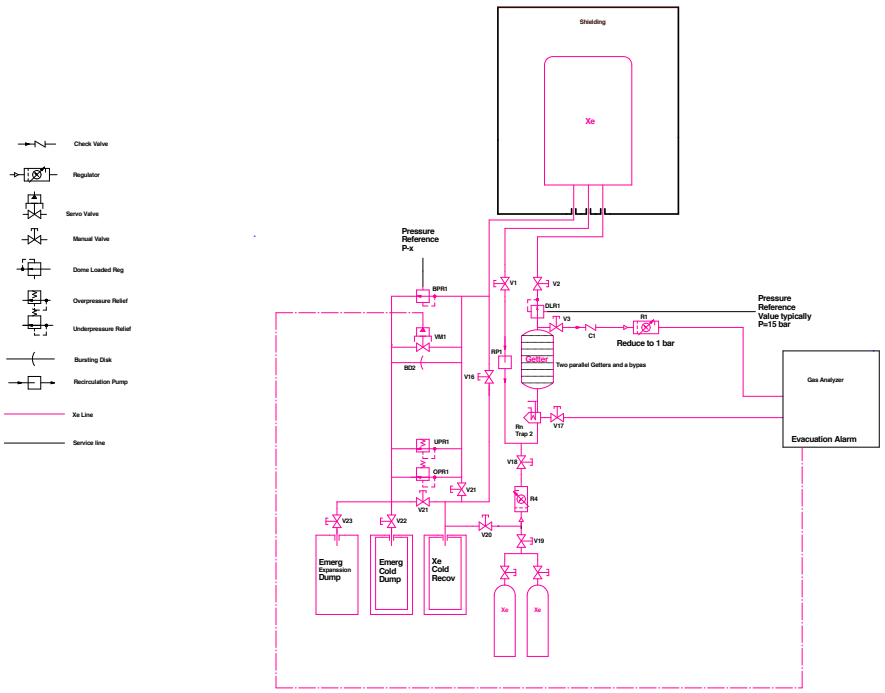

Figure 1.30: Schematic of the gas system.

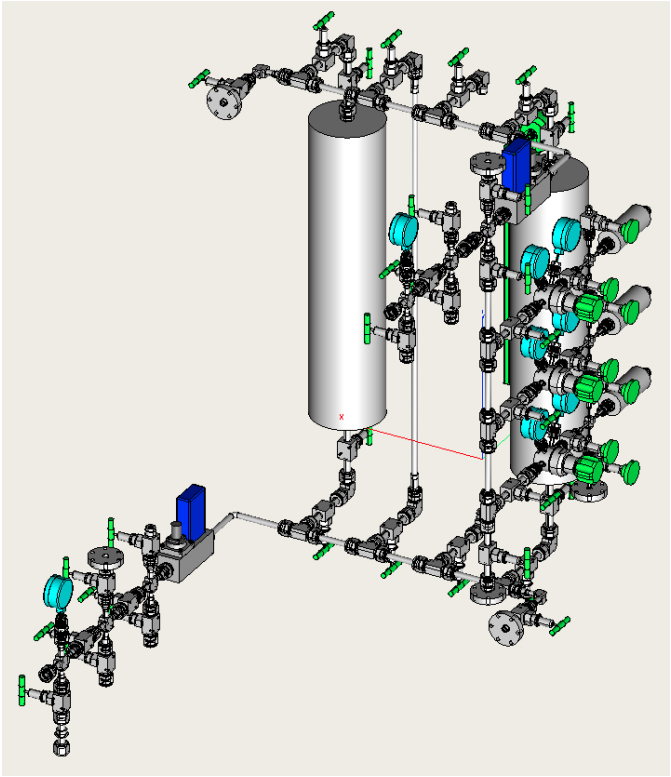

Figure 1.31: Three dimensional engineering model of the gas system piping.

4. Pressure relief for fire or other emergency condition (to ASME std.) - vent to closed reclamation system

5. Maximum leakage, EXe through seals (total combined) - 100 gm/yr

6. Maximum loss, EXe to atmosphere - 10 gm/yr

7. Accomodate a range of gasses - EXe, DXe, N2, dry air, Ar, 95N2/5H2, EXe/TMA, EXe/CF4

8. Circulate all gasses through detector- 10 SCM/min in axial flow pattern

9. Purify EXe continuously - inlet condition to be $<$ 1ppb O2, CO2, N2, CH4, THC$<$1ppt Ra

10. Pull vacuum 1*10^{-6} torr at vessel port

11. Provide 1 bara N2 to PMT enclosure system

12. Provide gas circulation of 1 SCM/min through annulus

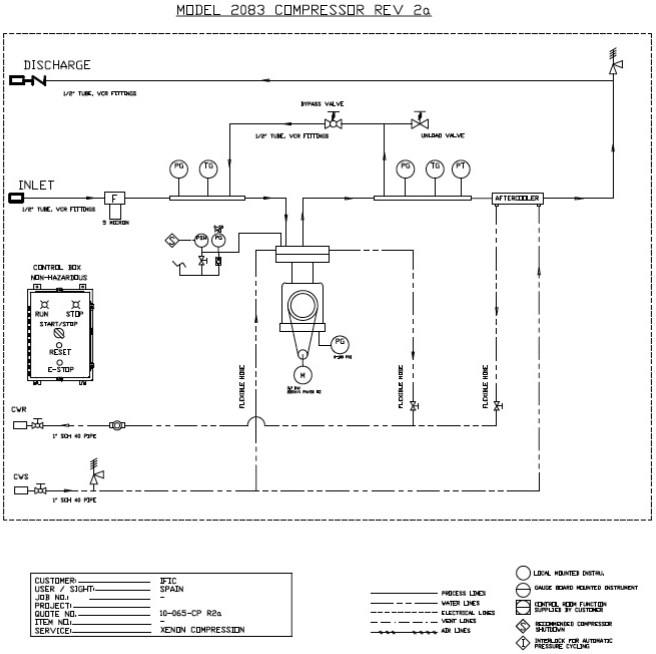

Figure 1.32: Schematic for the re-circulation pump.

The general schematic of the gas system is given in Figure 8.1. A 3D model is shown in Figure 8.2. The re-circulation pump, vacuum pump and cold traps are not shown.

The most vulnerable component of the gas system is the re-circulation pump. The enriched ^{136}Xe used in NEXT 100 project is very expensive and therefore the pump to move the gas through the re-circulation loop must have sufficient redundancy to minimize the probability of failure and leakage. Furthermore, to preserve the purity of the gas all metal to metal seals must be used. A pump manufactured by Pressure Products Industries [1]. This pump is made with metal-to-metal seals on all the wetted surfaces. The gas is moved through the system by a triple stainless steel diaphragm. Between each of the diaphragms there is a sniffer port to monitor for gas leakages. In the event of a leakage automatic emergency shutdown can be initiated (Figure 8.5).

Figure 1.33: Example of the re-circulation pump chosen for the Xe purification gas system. This is a triple stainless steel diaphragm pump capable of 200 slpm flow rates.

In terms of redundancy and reliability the estimate time time between failures during continuos operation per diaphragm is in excess of 40 years. Therefore this is a very safe, clean and reliable pump with a nominal maximum flow rate of 200 standard liters per minutes.

MicroTorr cold getter model number MC4500-902FV has been chosen as the purification filter for the Xe gas. Capable of removing electron negative impurities to less than 1 ppb the model chosen has a nominal flow rate of 200 standard liters per minute well in excess of the required flow rates for NEXT-100 offering sufficient spare capacity. The gas system will contain two such getters in parallel with a bypass. This configuration has been developed and used by the smaller gas systems operating at UNIZAR and IFIC. The second spare getter is placed in parallel in the event of accidental contamination of one of the getters allowing uninterrupted running. The ability to bypass the getters will allow the testing of the purification of the gas and aid in diagnostic and monitoring of the gas system.

[1] http://www.pressureproductsindustries.com/compressors/diaphragm_compressors.html

As the xenon gas that will be used in the NEXT-100 is expensive an automatic recovery system will be needed to evacuate the chamber in a case of an emergency condition. We are discussing the solution has been proposed by the LUX collaboration where a permanently chamber cooled by liquid Nitrogen will be used.

We have identified two primary conditions to trigger automatic evacuation. The first condition is an overpressure that could potentially cause an explosion. Because the gas system for NEXT-100 will be operated in a closed mode the overpressure condition could occur only under two possible conditions. The first is during the filling stage of the operation, when the system is being filled with gas and the second in the case of thermal expansion of the gas due to laboratory fire. In the case of overpressure we will have an electromechanical valve, activated by a pressure switch, that will open a pipe from the NEXT 100 chamber to a permanently cold recovery vessel. This will then cryo-pump xenon into the recovery vessel, causing the gas to freeze in the recovery tank. In the event of the electromechanical valve failing, a mechanical spring-loaded relief valve, mounted in parallel to the electromechanical valve, would open and allow the xenon to be collected in the recovery vessel. As a final safety feature in case both the electromechanical and spring-loaded valves fail a bursting disk, also mounted in parallel to the electromechanical and spring-loaded valves, will burst connecting the NEXT 100 chamber with the recovery vessel causing the gas to be thus evacuated.

The second emergency condition would be detected as under-pressure indicating a leak in the system. Such condition would require evacuation of the NEXT 100 chamber to prevent losses of gas. If this is detected an electromechanical valve sensing under-pressure will open and evacuate the xenon into the recovery vessel.

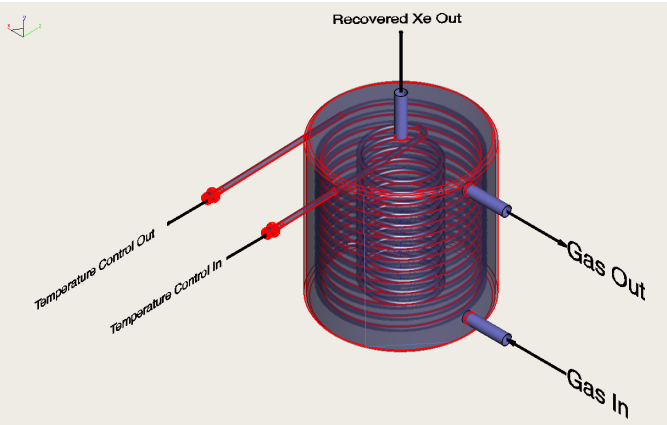

Figure 1.34: Example of a Xe cold trap.

As the recovery vessel is to be used for safety there cannot be a valve to close once the emergency recovery has been completed. Therefore in the event an automatic system is triggered a signal will be sent to an operator to arrive at the laboratory to supervise post recovery procedures. The aim of post recovery is to move the collected xenon from the recovery vessel to a closable gas bottle for future purification and use once

the problems that caused the emergency conditions have been rectified. This operation must be conducted by the responsible person and would involve cryo-pumping the gas collected in the recovery vessel into a stainless steel bottle which will be valved off post transfer.

The same system can be used for controlled recovery of xenon if work needs to be done on the NEXT-100 chamber.

The other condition that may trigger xenon reclamation is leaking through porous seals into the vacuum or a buffer gas. For instance in the design for the energy plane (see chapter 5) xenon could leak through the photomultiplier enclosure (can). If this happens the use of a cold trap as one shown in Figure 8.11 would permit to recover the gas. The mechanism is simple: a liquid at the xenon freezing temperature circulates through the double concentric coils seen in the figure and then freezes the gas as it circulates through the trap. Periodically the trap will be heated to evaporate the trapped ^{136}Xe into the holding vessel for re-purification. In the specfici case of a leak inside the cans of the energy plane the gas will be recovered by continuously vacuum pumping the system through the cold trap.

1.7 Shielding

In our CDR we described two shielding possibilities, a water tank and a water-lead-copper shield. In this TDR we present our final choice. We have chosen a simple structure made of lead and copper primarily on the grounds of safety and easy access. Access to all the critical systems for improvement, repair or regular servicing, which we expect will be frequent during the first year of operation, is much easier if the detector is not immersed in liquid. In addition one avoids HV cables and high-pressure pipes inside the water.

At the same time, the shielding structure that we have designed (a.k.a. lead castle) presents significant difference with respect to that proposed in the CDR. As for the PV, we have simplified the design (e.g, eliminating the water bricks), changed to horizontal axis, and coupled the castle to a working platform (following a requirement of the LSC) and a seismic structure. The lead castle and the seismic structure thad holds the detector are independent, to allow seismic oscillations in the event of an earthquake.

Figure **??** shows a 3D view of the whole structure. The most important systems are:

a. The apparatus, described in chapter 4.

b. The shielding structure, a.k.a. lead castle made out of lead bricks and terminated by a copper sheet.

c. The platform holding the vessel, mounted on a seismic structure.

d. The platform.

e. The gas system, described in chapter 8.

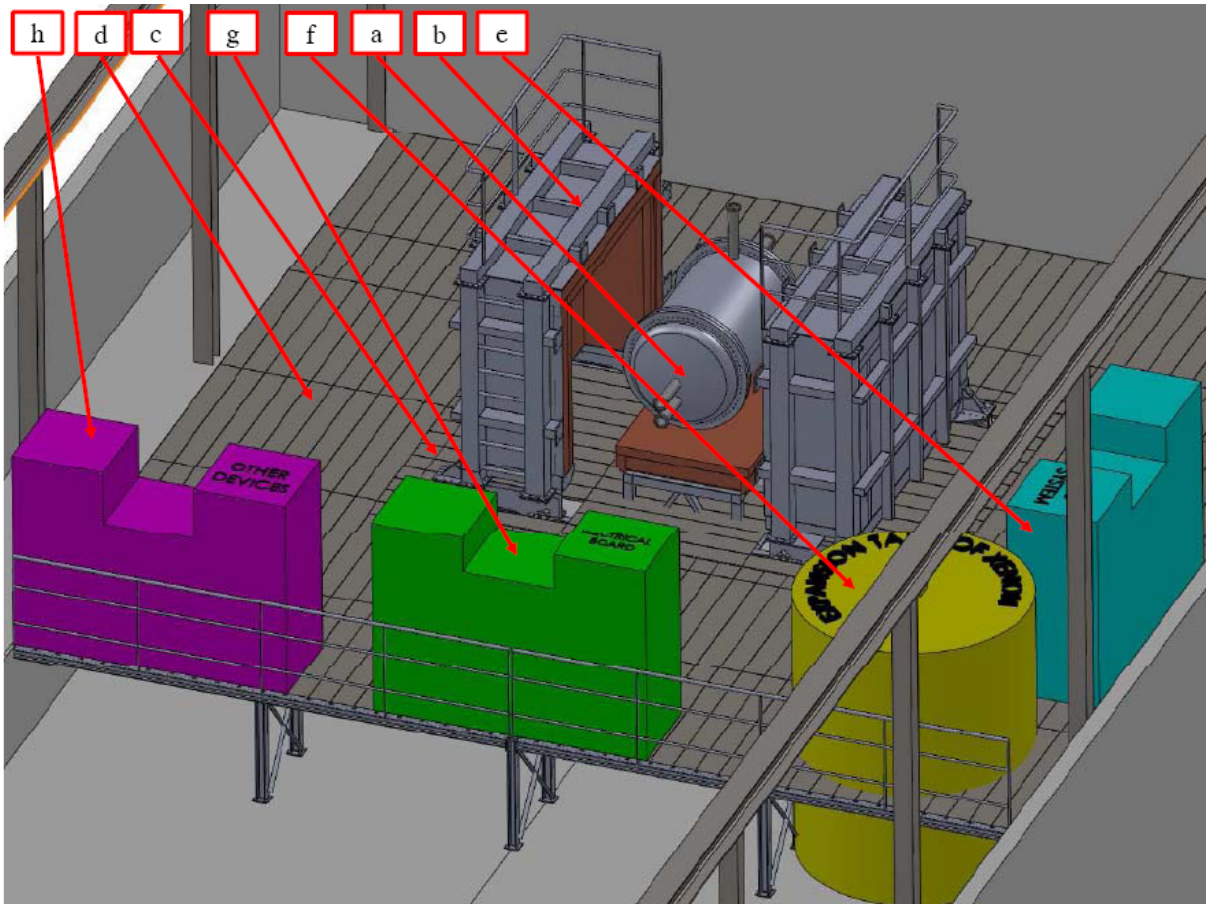

Figure 1.35: NEXT-100 lead castle and platform at the LSC

f. The xenon expansion tank also described in chapter 8.

g. Power and DAQ racks.

h. Other devices (e.g, slow controls).

i. Gas and cable pipes (not show in the figure).

In this chapter we present an integrated design of the working platform (WP), the seismic structure to hold the detector (a.k.a. detector pedestal, DP) and the lead castle (LC) itself.

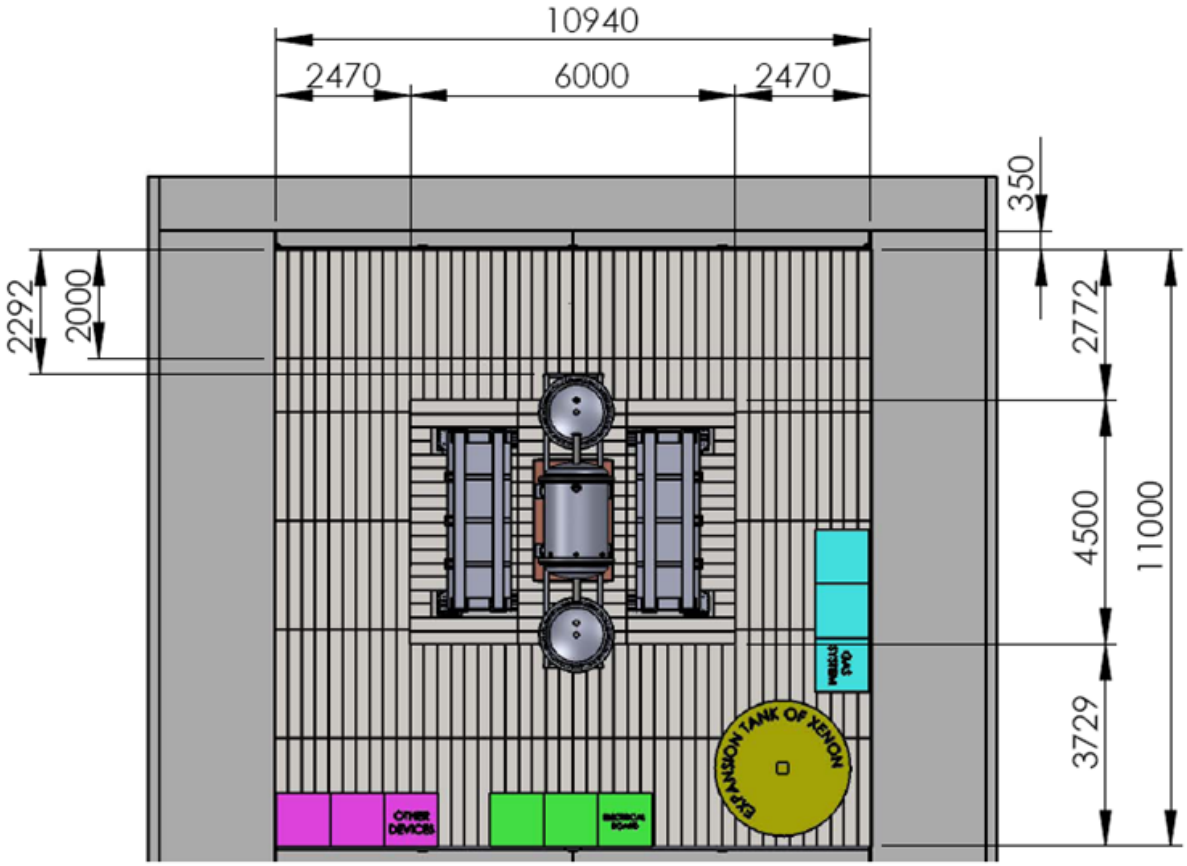

Figure 1.36: Top view of the layout

Figure 9.2 shows a top view of the layout, with dimensions. The platform has a squared shape, with dimensions of 11×11 m^2 meters and useful surface of 112 m^2. It includes a safety area with a length of about 2 meters to provide clear access in case of an emergency.

The DP, WP and LC are composed of modular and standard elements which will be manufactured by a supplier. All beam welding and most of the bolting will be done

outside the LSC hall. Pre-assembled elements will be transported to the LSC, cleaned when necessary (e.g, the lead bricks) and assembled in place, according to a procedure previously tested at an external workshop.

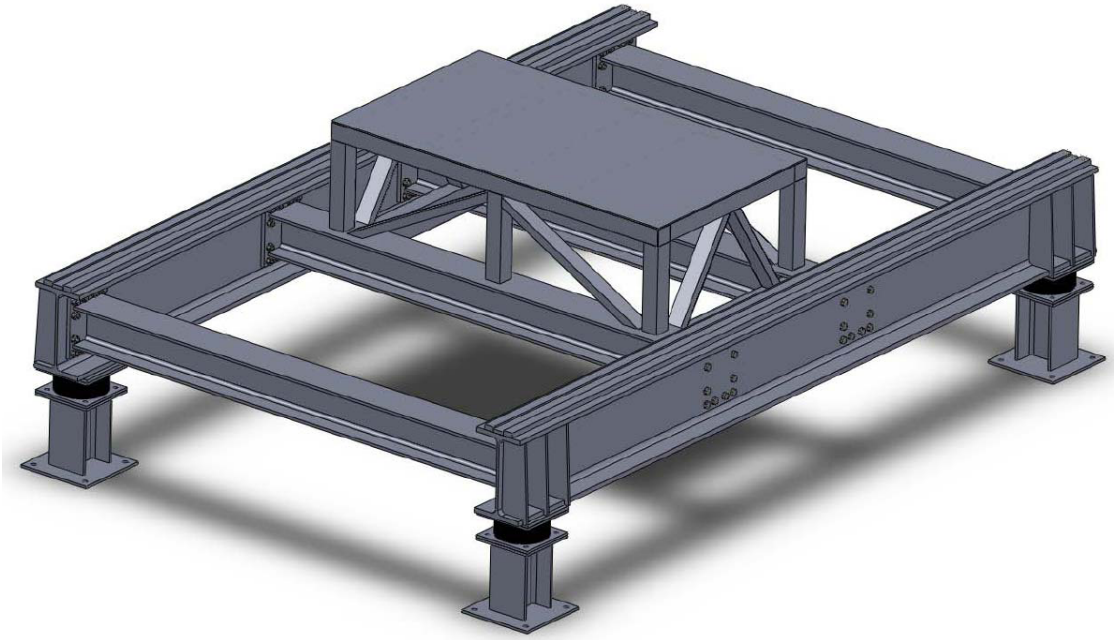

Figure 1.37: Three-dimensional view of the seismic structure (a.k.a. detector pedestal, DP)

The DP is shown in Figure 9.3. It is anchored to the pool ground and supports all the weight of the detector and the LC. The WP shown in Figure 9.5 is designed to stand a uniform load of 300 kg/m^2 and a concentrated load of 200 kg/m^2.The platform is anchored to the pool ground and to the pool walls. Notice that the WP and the DP structured are independent to allow seismic displacements in the event of an earthquake. The platform floor tiles are made of galvanized steel and have standard dimension to minimize cost. All beams and pillars of the WP are designed with IPE and HEB cross sections, IPE-100 for pillars, HEB-240 for seismic beams and HEB-500 for main seismic beams.

The movable lead castle has two position: opened, as shown in Figure 9.5 and closed, as shown in Figure 9.6. The open position is used for the installation and service of the pressure vessel. The closed position is used normal operations. The LC itself is made of two halves mounted on a system of wheels that move on tracks with the help of an electric engine. The system includes a lifting device and a lock for each wheel. The lifting devices elevates all the wheels from 5 to 10mm above the guides. Once in the desired position the lock fixes the movable lead castle to the seismic structure, both in the open and in the closed position, to avoid seismic displacements during an eventual earthquake.

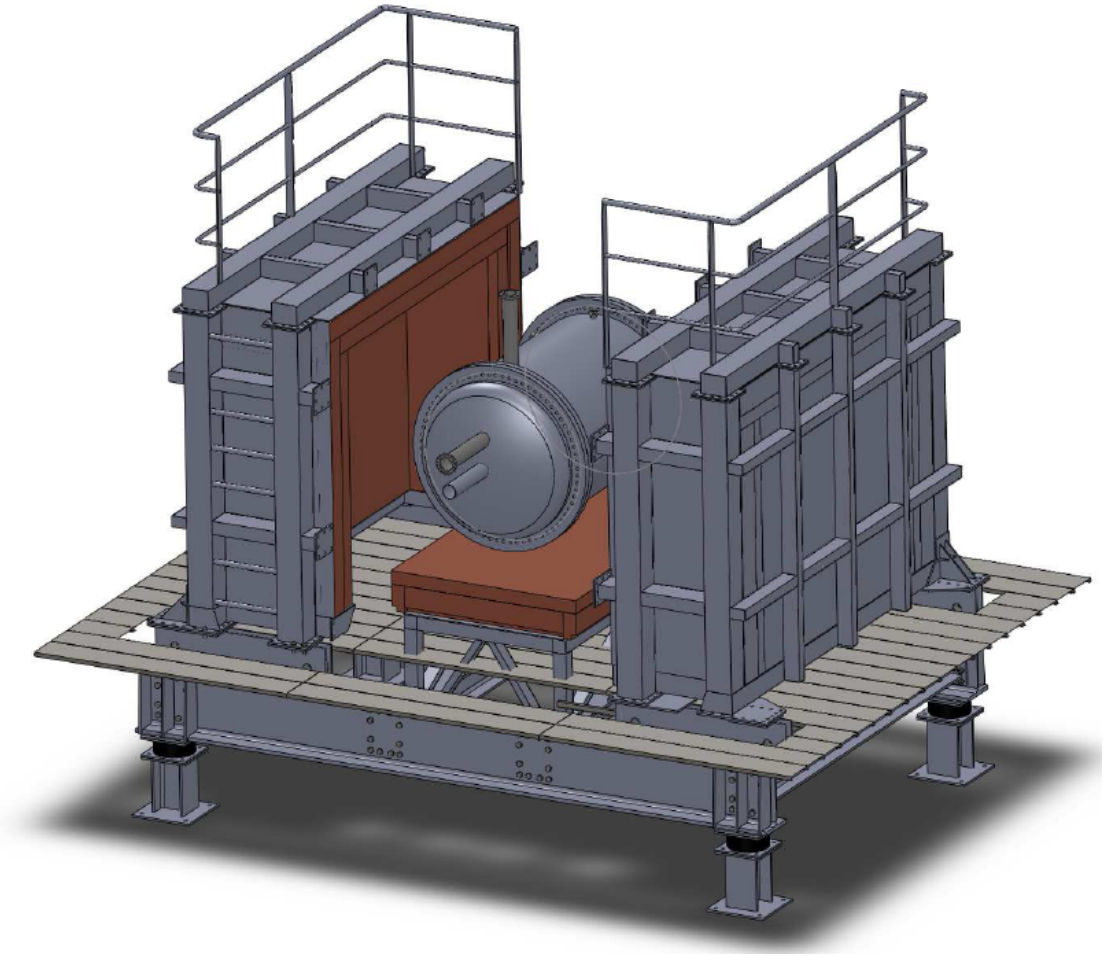

Figure 1.38: View of the DP holding the pressure vessel and movable lead castle

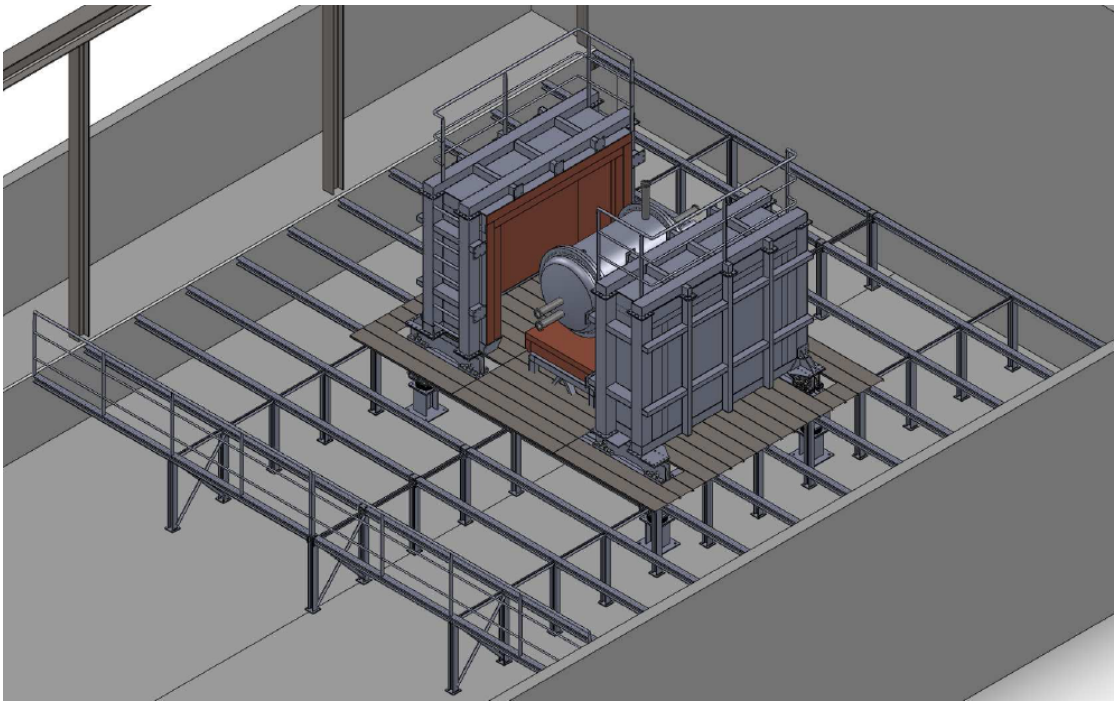

Figure 1.39: WP and DP with the lead castle opened.

A top view of the lead castle is shown in Figure 9.7. The lead wall has a thickness of 20 cm and is made of fours layers of staggered lead bricks and copper or steel sheets. The lead bricks have standard dimensions ($200 \times 100 \times 50$ mm^3, and, by requirement, an activity in uranium and thorium less than 0.4 mBq/kg respectively.

A copper wall, made of copper sheets was designed to further attenuate the residual activity emanating from the lead and to provide structural support. The thickness shown in Figure 9.7 is 10 cm. However, with the introduction of the inner copper shield inside the pressure vessel the thickness of the external copper shield can be considerably reduced, and even eliminated (in reality we have simply moved it inside the PV). Instead we will use a radiopure SS sheet (from the same batch used to build the detector), 1 cm thick, to provide structural support to the whole system.

Work is underway, in coordination with LSC staff to refine and complete the design of each relevant element, and the integration of all the systems.

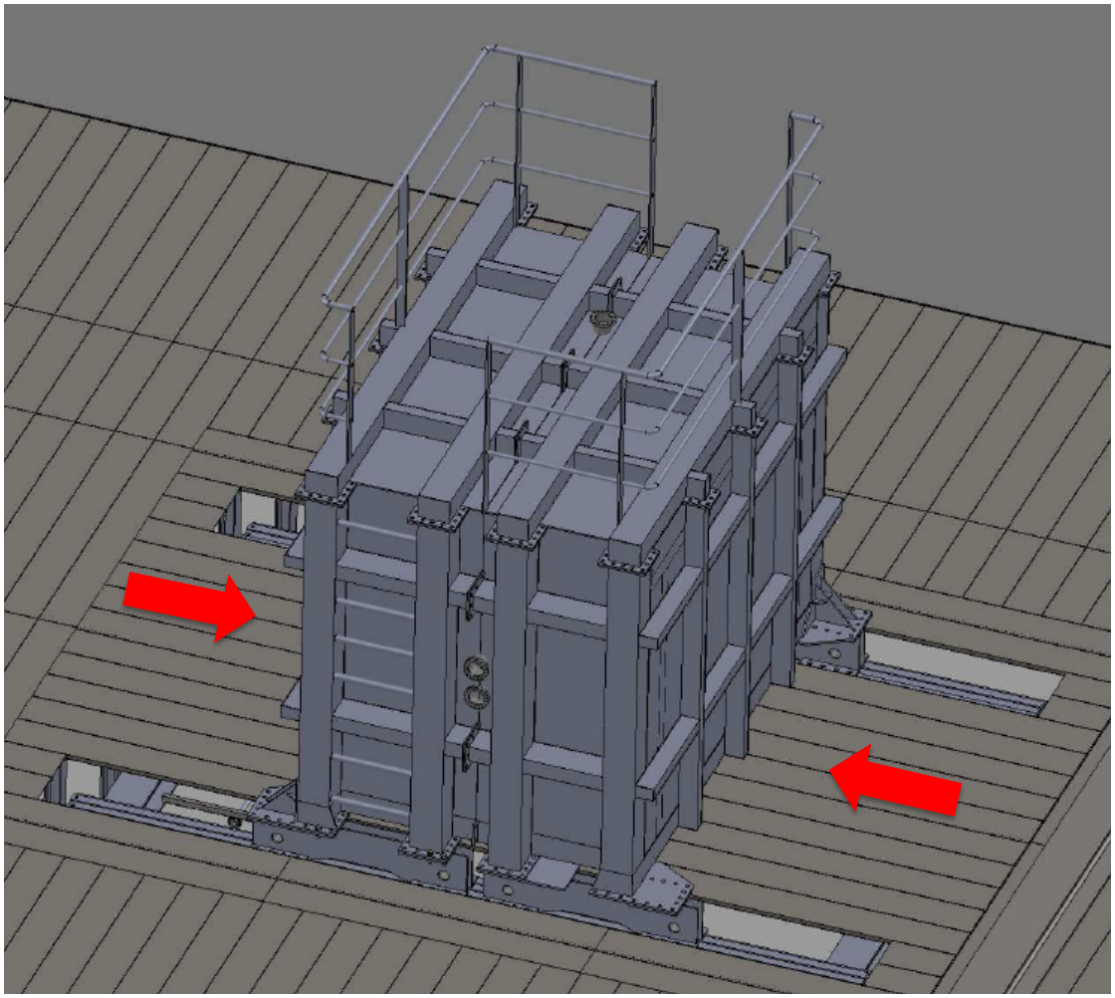

Figure 1.40: Three-dimensional view of lead castle closed

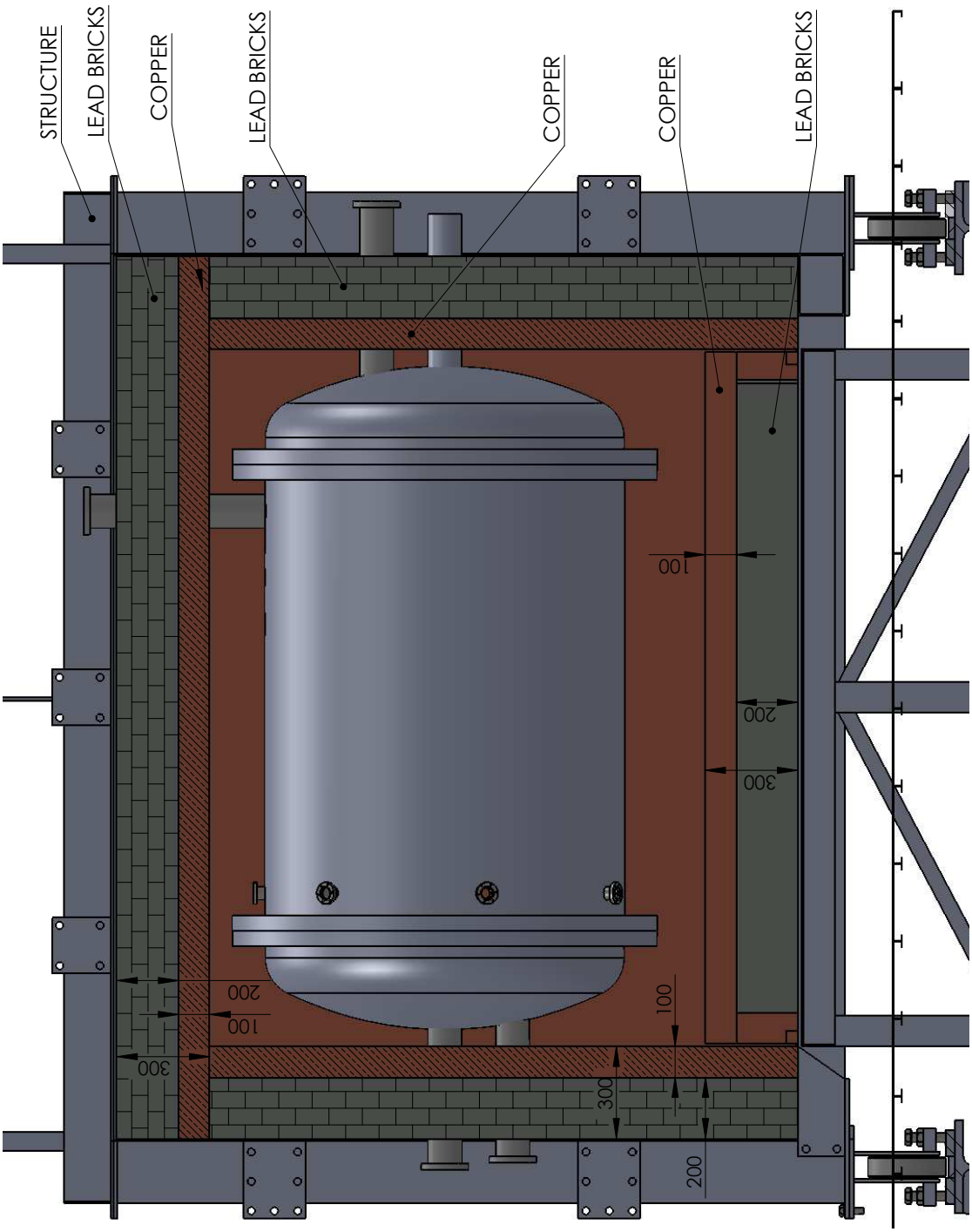

Figure 1.41: View of the lead castle

Chapter 2

Radiopurity and background model

2.1 Control of material radiopurity

A DBD experiment needs to be built of extremely radiopure components. To that end, we have conducted an initial compilation of the radiopurity of the materials expected to be used in the construction of NEXT-100. During the last six months we have also initiated a screening campaign that will continue during the next two years. We have also consulted the existing literature. Relevant materials for shielding, vessel, High Voltage and EL grids, detector components at the energy and tracking planes and others have been taken into consideration. This compilation is intended to:

- The optimal selection of radiopure materials, identifying if possible, the provider or a model of the component giving the lowest activities. Information on previous measurements helps to establish fair priorities in the use of Ge detectors.
- The construction on the NEXT-100 background model, providing reference activities to normalize simulations.

The techniques employed up to now for the radiopurity measurements performed for NEXT are GDMS (Glow-Discharge Mass Spectrometry) and germanium spectroscopy. GDMS measurements have been made by Shiva Technologies (Evans Analytical Group) in France; this method (very suitable for metals) is fast and requires only a small sample of the material, but as the output is only the concentration of elements, particular isotopes are not identified and broken secular equilibrium in the chains cannot be detected. Ge spectroscopy measurements have been made at the LSC using a $\sim$1 kg detector operated by the University of Zaragoza and the $\sim$2 kg detectors from the laboratory.

Results of all radiopurity measurements performed for NEXT are compiled at a database available for the collaboration by means of a web application [2], including all the available, relevant information.

2.2 Study of shielding materials

Lead samples from different providers (Mifer, Tecnibusa and COMETA) have been screen by GDMS. Results are shown at rows #1-5 in Table 2.1. Specifications on radiopurity of COMETA lead (row #2) agree with the measured activities and offer <100 mBq/kg of ^{210}Pb.

Copper samples from different origins (Luvata company with both hot and cold rolling, Sanmetal company and electroformed copper at University of Zaragoza) have been screen by GDMS. Results are shown at rows #6-10 in Table 2.1.

2.3 Study of vessel components

Ti grade 2 (or grade 3) was considered to be very radiopure and as a consequence it was identified, in our CDR, as the material of choice to build the PV. Unfortunately, our investigations, so far, do not confirm an extraordinary radiopurity for various samples, measured by us or available in the literature. Specifically, we considered:

- A sample from Nironit, grade 1, type A35, Titanium was measured for the XENON experiment using the GATOR detector at Gran Sasso Laboratory [7]. Results are shown at row #11 in Table 2.1.

- A Ti sample coming from the batch used in the LUX cryostat (type CP1) was screened using different techniques and after undergoing different treatments. Qualitative information on this sample was obtained also from PIXE (Particle Induced X-ray Emission) and RBS (Rutherford Back Scattering) analysis at the Centro Nacional de Aceleradores in Sevilla. Results are shown at rows #12-15 in Table 2.1, together with the values provided by LUX collaboration for a 8-kg sample using Ge detector MAEVE (ORO) [8]. An important surface contamination was produced at some step when handling the sample; after polishing it, removing a thin layer of ∼0.5 mm, the high activity levels were dramatically reduced (compare results at rows #14 and #15 in Table 2.1) but results coming from different techniques are not fully compatible.

- A sample of grade 2 Titanium coming from a Spanish provider, Titanio SMP[1], has been screened with one of the 2-kg Ge detectors (GeOroel) of the Canfranc Underground Laboratory. It consisted of 8 1-mm-thick cylinders having a total mass of 121 g. A standard cleaning protocol was including:

  1. Diamond cut.
  2. Diamond-sanding to remove the titanium oxide surface.
  3. Cleaning with acetone (alcohol was avoided because it can affect the mechanical properties).

[1] http://www.titaniosmp.com/

4. Acid-detergent.
5. Nitric acid-bat, to remove iron that may be on the surface without affecting the titanium).
6. Back to clean with acetone.
7. Saving in an hermetic plastic bag.

Preliminary results are shown at row #16 in Table 2.1.

- A sample of grade 2 Titanium from Titanium Metal Supply[2], as the one used by the LUX Collaboration, has been screened at the Canfranc Underground Laboratory with detector GeOroel. It consisted of three cubes ($50\times50\times50$ mm^3 corresponding to a mass of 0.57 kg each) and underwent the standard cleaning protocol fixed and described before. Preliminary results are shown at row #17 in Table 2.1.

The conclusion of our initial investigations is that the uncertainties about the radiopurity of titanium samples are large. Therefore we have also investigated stainless steel, as an alternative to build the PV. We have explored the following samples:

- One sample of type **304L** from Pfeiffer has been screened using the Ge detector from University of Zaragoza at Canfranc. Results are shown at row #18 in Table 2.1. Type AISI304L was also analyzed by Borexino [3].

- Type **316L** was studied using GDMS for the DRIFT experiment by UKDMC and results are reported at [16] and summarized at rows #19-20 in Table 2.1. Many samples of this type of steel were analyzed also at SNOLab [6] and results for one of the cleanest sample are quoted at row #21 in Table 2.1, but values up to one order of magnitude higher were also found.

- Material referenced as **austenitic 1.4571** (also 316L) has been extensively studied by GERDA and by XENON. Best values reported in Table 1 at [4] (measurement #7) are for stainless steel 316Ti supplied by Nironit, 1.5-mm-thick and used for the XENON cryostat wall; they are presented at row #22 in Table 2.1. Best results obtained by GERDA (sample #2) [5] are also quoted at row #23 in Table 2.1. According to these measurements, values or upper limits on activity at the level of even tenths of mBq/kg can be found for isotopes from the natural chains at the best case.

- Samples of different types and suppliers have been analyzed by several experiments, like for instance at SNOlab (NA Stainless, Nironit, Swagelok, 316L) [6].

The conclusion is that it appears possible to secure a batch of SS of less than 5 μBq/kg. As discussed later, this activity is acceptable when an ICL made of 12 cm of copper is added.

[2] http://www.titaniummetalsupply.com

We have also investigated the bolts, that will be made of Inconel. Samples of Inconel 718 (diameter: 32 mm, height: 50 mm) and Inconel 625 (80×70×10 mm^3) from the Spanish company Mecanizados Kanter[3] have received the standard cleaning protocol and have been screened with one of the 2-kg Ge detectors (GeOroel) of the Canfranc Underground Laboratory. Preliminary results are shown at rows #25-26 in Table 2.1.

Concerning the joints and gaskets we have investigated the literature, to find:

PCTFE: EXO has screened a PCTFE sample, reported as "Saint Gobain supplied Daikin Neoflon PCTFE (Kel-F), M-400H, raw material" at measurement #50 at [9]. Results are shown at row #27 in Table 2.1.

Viton: a sample for O-ring seal was screened by EXO (measurement #154 at [9]). Results are shown at row #28 in Table 2.1.

Electron beam, TIG or MIG are possibilities for the welding. A sample referenced as "Stainless steel TIG" from Harris Product Group has been screened at SNOlab and results are quoted at row #24 in Table 2.1. EXO has reported (measurement #6 at [9]) the concentrations of Th and U after TIG welding on a copper sample: <9.8 pg/cm of Th, 10.2±3.4 pg/cm of U. A filler for TIG soldering, made of Ti grade 2 (diameter: 2 mm) supplied by ETM company is being screened at Canfranc Underground Laboratory.

2.4 High Voltage and EL grids components

The main components of the *field cage* will be copper rings, resistors and peek. High density polyethylene could also be used.

Peek: a sample (18 bars) from Sanmetal company has been screened using the Ge detector from University of Zaragoza at Canfranc. Values obtained are shown at row #29 in Table 2.1. Results from another measurement on peek presented at [10] are quoted at row #30 in Table 2.1.

Resistors: surface mount precision plate resistors supplied by Finechem were screened by XENON (measurement #44 at Table 1 in [4]). Results are shown at row #31 in Table 2.1. SMD resistors from Farnell have been also measured at Canfranc with the Ge detector from University of Zaragoza and results are presented at row #32 in Table 2.1.

Polyethylene: samples of material to be used as neutron moderator in shieldings have been screened for different dark matter experiments; best results from EDELWEISS (supplier Plastiques du Rhone) presented at [16] and from XENON (supplier in2plastic, measurement #14 in Table 1 at [4]) are shown at rows #33-34 in Table 2.1. More results are available at [16]. Polyethylene insulator from cables has been analyzed by EXO and values from measurement #199 at [9] are quoted at row #35 in Table 2.1.

The *High Voltage feedthroughs* will consist of a metal rod pressed into a plastic tube (Tefzel or FEP). Copper shields could be used.

For the *EL grids*, the mesh will be made of stainless steel.

The *light tube* will be made of Tetratex fixed over a 3M substrate, coated with TPB. ArDM has screened specifically PTFE Tetratex from Donaldson Membranes by

[3] http://www.mecanizados-kanter.es/

ICPMS [11]. Results are summarized at row #36 in Table 2.1. TPB from two different manufacturers have been measured at SNOlab [6] and results are presented at rows #37-38 in Table 2.1.
Teflon: samples from many different origins have been screened in the context of several experiments (a compilation is available at the documentation page of the website [2]).

- The cleanest one we are aware of is DuPont Teflon TE-6472, for which raw material has been measured by EXO using Neutron Activation Analysis (NAA) (measurement #43 in Table 3 at [9]); these results are summarized at row #39 in Table 2.1.

- GERDA has also reported results for a clean Teflon sample (Dyneon TF 1620) [12], quoted at row #40 in Table 2.1; at [13], where slightly different activities are reported for this PTFE, it is said that it was sintered on special request in a clean way by ElringKlinger Kunstofftechnik GmbH.

2.5 Detector components

2.5.1 Energy plane

Different models of *photomultipliers* have been under consideration.

- **Hamamatsu R8520-406**: many different batches of model R8520 have been screened in the context of the XENON100 experiment; an average of measured activities has been made using results in Table 1 at [4] (considering batches from 1 to 17 excluding 3, 5 and 6) and is shown at row #41 in Table 2.1. Activities on a custom base for this PMT model are also reported at measurement #40 in Table 1 at [4] and summarized at row #42 in Table 2.1.

- **Hamamatsu R7378A:** activity is $\sim$50 mBq/PMT of ^{238}U and ^{232}Th [14].

- **Hamamatsu R11410MOD:** XENON (measurement #38 in Table 1 at [4]) and LUX [15] have measured activities for this photomultiplier, quoted at rows #43-44 in Table 2.1. Specifications provided by Hamamatsu for this model are also shown at row #45 in Table 2.1.

Sapphire and quartz have been proposed as possible materials for the *windows* coupling PMTs to the vessel.
Sapphire: sapphire crystals from different origin have been screened within the ROSEBUD experiment; best results from [16] are summarized at rows #46-47 in Table 2.1. Sapphire windows have been measured by EXO (from Swiss Jewel Company, substrate for EXO high voltage resistors). Results obtained using NAA (measurement #155 in [9]) are quoted at row #48 in Table 2.1.
Quartz (or fused silica): different kinds of quartz have been screened by EXO (measurements #61 to #67 at [9]) using NAA. One of the cleanest sample is Heraeus 2, having activities reported at row #49 in Table 2.1.

2.5.2 Tracking plane

The *daughter boards* for *SiPM* will be made of cuflon coated with TPB.
Cuflon: a circuit board made of cuflon was screened for the EDELWEISS experiment and the results taken from [16] are shown at row #50 in Table 2.1. GERDA has reported more stringent results for cuflon at [12], shown at row #51 in Table 2.1. A cuflon sample was analyzed by ICPMS and Ge gamma spectroscopy at [17], and results are shown at rows #52-53 in Table 2.1; even independent results for Cu and Teflon have been reported from ICPMS.

For the *mother boards*, many different types of circuit boards from several providers have been screened for different experiments, like EDELWEISS. Results taken from [16] are shown at rows #54-62 in Table 2.1.

For *SiPM Electronics*, wires, digitizers, multiplexers, optical transceiver or optical links are expected to be used. A collection of some measurements of radiopurity of connectors, resistors, capacitors, wires,... was made and is available at the documentation page of the website [2].

2.6 Others

Xe gas: activities of ^{238}U and ^{232}Th chains were estimated by means of $\beta\alpha$ (BiPo sequences) and $\alpha\alpha$ coincidences at the Gotthard experiment [18], being of 0.11 mBq/kg of ^{238}U and 0.02 mBq/kg of ^{232}Th. Information on activities of ^{85}Kr and ^{39}Ar could be deduced from the purity measurements performed for both natural and enriched xenon by EXO200 [19].

Regarding the *gas system*, pipes and valves as well as temperature, pressure or flux sensors located inside the shielding and moreover inside the vessel must be controlled. Just as an example, the HF4000 CARTEN valve ($\sim$47.7 kg), used for turbomolecular pump and mostly made of 316L stainless steel, would be close to the vessel requiring possibly to be inside a radiopure cap.

Materials for other elements of the experimental set-up still to be defined, like the calibration or the slow control systems, should be also considered. Radiopurity of a huge amount of adhesives (Araldite, Epoxy,...) was made at [20].

2.7 Summary

Using the extensive information collected from the literature and our initial screening measurements we can already construct a first background model for NEXT.

The two dominant sources of activity are the vessel system and the energy plane system, since PMTs are considerably more radioactive that the cuflon boards that will made the bulk of the activity in the tracking plane (notice that the FE electronics will be shielded behind the ICS).

For the PV we consider 5 mBq/kg in the uranium series and 5 μBq/kg in the thorium series as the maximum acceptable activity of the PV stainless steel. Taking into account

the activity of LUVATA copper we believe that the activity of the ICS will be ∼10 μBq/kg (possibly slightly more in the uranium series and significantly less in the thorium series). The ICS will attenuate the activity of the PV by roughly a factor 100. Thus, the residual activity from the PV will be about 50 μBq/kg. The total mass of the PV is 1.2 tons, and therefore the residual activity will be 60 mBq (in each of the series). The mass of the ICS is 9 tons, resulting in 100 mBq of activity due to the uranium series and possibly up to a factor 2 less in the thorium series.

The photomultipliers chosen for NEXT-100 are the R11410-10 (also called R11410MOD) model from Hamamatsu. Their levels of activity are of the order of 3 mBq per unit in the uranium series (U) and 2 mBq per unit in the thorium series (Th) There will be 60 such PMTs, resulting in 180 mBq (U) and 120 mBq (T). This activity is comparable to the ∼160 mBq from the PV+ICS system.

To complete our background model, we will continue our screening campaign, with the following priorities:

- Intensive screening of stainless steel batches until we can identify one with acceptable activity.
- Screening of R11410-10 PMTs, to check with our own measurements the information existing in the literature.
- Screening of full DBs (with MPPCs soldered to the board and a layer of TPB) to assess the total activity of the DB system.
- Screening of Inconel bolts.
- Screening of the selected gaskets and seals.
- Screening of resistors, capacitors and other electronic components as we identify them.

Table 2.1: Activities of ^{238}U , ^{232}Th and ^{40}K measured in relevant materials and following different techniques.

#	Material	Technique	Unit	^{238}U	^{232}Th	^{40}K	Ref.
	Shielding						
1	Pb, Cometa	GDMS	mBq/kg	0.37	0.073	<0.31	NEXT
2	Pb, Cometa		mBq/kg	<0.5	<0.5	<1	Cometa
3	Pb, Mifer	GDMS	mBq/kg	1.24	0.32		NEXT
4	Pb, Mifer, new provider	GDMS	mBq/kg	0.33	0.10	1.21	NEXT
5	Pb, Tecnibusa	GDMS	mBq/kg	0.73	0.14	0.91	NEXT
6	Cu, Luvata C10100	Ge (by UZ)	mBq/kg	<11.0*	<9.7*	<17.7*	NEXT
7	Cu, Luvata C10100 hot rolled	GDMS	mBq/kg	<0.012	<0.004	0.061	NEXT
8	Cu, Luvata C10100 cold rolled	GDMS	mBq/kg	<0.012	<0.004	0.091	NEXT
9	Cu, Electroformed	GDMS	mBq/kg	<0.062	<0.020		NEXT
10	Cu, ETP Sanmetal	GDMS	mBq/kg	<0.062	<0.020		NEXT
	Vessel						
11	Ti, Nironit, XENON	Ge	mBq/kg	0.93±0.24 (b)	0.22±0.10	0.90±0.30	[7]
12	Ti, LUX	Ge	mBq/kg	6.2±1.2, <0.19	<0.25	<0.9	[8]
13	Ti, LUX	GDMS	mBq/kg	52	2.5	<1.5	NEXT
14	Ti, LUX	Ge (by UZ)	mBq/kg	238±28	417±54	49±11	NEXT
15	Ti, LUX, after polishing	Ge (by UZ)	mBq/kg	<15*	4.2±1.4	<22*	NEXT
16	Ti, SMP	Ge (by LSC)	mBq/kg	<9.4 (e)	<9.4 (f)	<19	NEXT (+)
17	Ti, Ti Metal Supply	Ge (by LSC)	mBq/kg	<0.30 (e)	3.2±0.3 (f)	<0.52	NEXT (+)
18	Stainless Steel, Pfeiffer 304L	Ge by UZ	mBq/kg	14.8±2.8 (a)	10.4±2.0 (a)	<16.6	NEXT
19	Stainless steel 316L, Elantic, UK, DRIFT	GDMS	mBq/kg	17.4±1.2	3.3±0.4	<9.3	[16]
20	Stainless steel 316L, block, Italy, DRIFT	GDMS	mBq/kg	<6.2	8.2±0.8	<9.9	[16]
21	Stainless steel 316L, SNOlab	Ge	mBq/kg	0.63±0.15 (b)	0.62±0.15	<0.97	[6]

(Follows at next page)

(Continuation)

#	Material	Technique	Unit	^{238}U	^{232}Th	^{40}K	Ref.
22	Stainless steel 316Ti, Nironit, XENON	Ge	mBq/kg	<1.9 (b)	<1.0 (d)	10±4	[4]
23	Stainless steel Austenitic 1.4571, GERDA	Ge	mBq/kg	<0.24 (b)	<0.11 (d)	<0.93	[5]
24	Stainless steel TIG, SNOlab	Ge	mBq/kg	1.01±0.71 (b)	2.8±0.8	<1.45	[6]
25	Inconel 718	Ge (by LSC)	mBq/kg	<5.6 (e)	<4.6 (f)	<11	NEXT (+)
26	Inconel 625	Ge (by LSC)	mBq/kg	<1.8 (e)	<2.0 (f)	<2.6	NEXT (+)
27	PCTFE, Daikin Neoflon, EXO	Ge	mBq/kg	5.6±1.2	<2.3	<30	[9]
28	Viton, O-ring seal, Johannsen AG, EXO	Ge	mBq/kg	868±87	130	2170±226	[9]
	HV and EL components						
29	Peek, Sanmetal	Ge (by UZ)	mBq/kg	36.3±4.3	11.7±2.2	8.3±3.0	NEXT
30	Peek	Ge	mBq/kg	<70 (b)	<50 (d)	<260	[10]
31	SM5D, 700MΩ resistors, Finechem, XENON	Ge	mBq/pc	0.027±0.003 (b)	0.014±0.003 (d)	0.19±0.03	[4]
32	SMD resistors, Farnell	Ge by UZ	mBq/pc	0.15±0.04 (e)	0.28±0.06 (f)	0.19±0.08	NEXT
33	Polyethylene, EDELWEISS	Ge	mBq/kg	16±10 (e)	<6 (f)	70±50	[16]
34	Polyethylene, XENON	Ge	mBq/kg	0.23±0.05 (b)	<0.14 (d)	0.7±0.4	[4]
35	Polyethylene insulator, EXO	NAA	mBq/kg	<2.9	<0.57	1.46±0.22	[9]
36	Tetratex, ArDM	ICPMS	mBq/kg	12.4±3.7	<1.6	<16	[11]
37	TPB, Sigma-Aldrich, SNOlab	Ge	mBq/kg	1.63±1.01 (b)	0.47±1.11	8.22±12.03	[6]
38	TPB, American Chemicals, SNOlab	Ge	mBq/kg	<4.33 (b)	<1.69	<36.29	[6]
39	Teflon, Du Pont TE-6472, EXO	NAA	mBq/kg	<0.0096	<0.0011	0.0558±0.0062	[9]
40	PTFE, Dyneon TF 1620, GERDA	Ge	mBq/kg	0.025±0.009 (b)	0.031±0.014 (d)	0.60±0.11	[12]
	Detector components: energy plane						
41	PMT, Hamamatsu R8520, XENON	Ge	mBq/PMT	0.19±0.01 (b)	0.20±0.02(d)	9.9±0.4	[4]
42	PMT base, Hamamatsu R8520, XENON	Ge	mBq/base	0.16±0.02 (b)	0.07±0.02 (d)	<0.16	[4]

(Follows at next page)

(Continuation)

#	Material	Technique	Unit	^{238}U	^{232}Th	^{40}K	Ref.
43	PMT, Hamamatsu R11410MOD, XENON	Ge	mBq/PMT	<2.4 (b)	<2.6 (d)	13±4	[4]
44	PMT, Hamamatsu R11410MOD, LUX		mBq/PMT	<0.4	<0.3	<8.3	[15]
45	PMT, Hamamatsu R11410MOD		mBq/PMT	3.3	2.3	5.7	Hamamatsu
46	Sapphire, Czochralsky Type, ROSEBUD	Ge	mBq/kg	<5 (e)	<5(f)	<30	[16]
47	Sapphire, Verneuil Type, ROSEBUD	Ge	mBq/kg	<3 (e)	<3(f)	<12	[16]
48	Sapphire window, EXO	NAA	mBq/kg	<0.31	0.123±0.029	<0.20	[9]
49	Quartz, Heraeus 2, EXO	NAA	mBq/kg	0.068±0.027	0.027±0.005	0.062±0.016	[9]
	Detector components: tracking plane						
50	Cuflon, circuit board, EDELWEISS	Ge	mBq/kg	<23 (e)	<30 (f)	400±200	[16]
51	Cuflon, Crane Polyflon, GERDA	Ge	mBq/kg	<0.85 (b)	<1.9 (d)	±15	[12]
52	Cuflon	Ge	mBq/kg	<0.84 (b)	<1.9	48±15	[17]
53	Cuflon	ICPMS	mBq/kg	$0.36^{+0.07}_{-0.04}$	$0.28^{+0.04}_{-0.03}$	6^{+9}_{-2}	[17]
54	ARJOPROX, ARLON	Ge	Bq/kg	<0.044 (e)	<0.065 (f)	0.3±0.2	[16]
55	ARAMID paper, CIMULEC	Ge	Bq/kg	<0.06 (e)	0.04±0.03 (f)	0.15±0.14	[16]
56	Kapton, AXON	Ge	Bq/kg	0.07±0.03 (e)		0.3±0.2	[16]
57	Kapton+Cu, KAPPA Industrie	Ge	Bq/kg	0.014±0.012 (e)	0.013±0.012 (f)	<0.09	[16]
58	Kapton+Cu, SOGGEG (g)	Ge	Bq/kg	<0.08 (e)	0.05±0.04 (f)	<0.9	[16]
59	Kapton+Cu, CIRE (g)	Ge	Bq/kg	0.09±0.05 (e)	<0.08 (f)	0.7±0.4	[16]
60	Kapton+Cu, CIRE (g)	Ge	Bq/kg	0.28±0.26 (e)	0.3±0.2 (f)	<2.1	[16]
61	Kapton+Cu ATLANTEK (g)	Ge	Bq/kg	<0.06 (e)	<0.02 (f)	0.4±0.2	[16]
62	Polyamide+Cu VISHAY	Ge	Bq/kg	9.1±0.2 (e)	3.3±0.2 (f)	7.0±0.7	[16]

(Follows at next page)

(Continuation)

#	Material	Technique	Unit	^{238}U	^{232}Th	^{40}K	Ref.
	(a) Average on different isotopes						
	(b) Activity of ^{226}Ra						
	(c) Two values for early/late part of chain						
	(d) Activity of ^{228}Th						
	(e) Activity from ^{214}Bi						
	(f) Activity from ^{208}Tl						
	(g) Special fabrication						
	(*) Level obtained from the minimum detectable activity of the detector (MDA)						
	(+) Preliminary result.						

Bibliography

[1] G. Luzn et al., "Characterization of the Canfranc Underground Laboratory: Status and future plans", proceedings of the 6th International Workshop on Identification of Dark Matter, World Scientific, 514.

[2] http://gifna.unizar.es/nextrp

[3] C. Arpesella et al, "Measurements of extremely low radioactivity levels in BOREXINO", Astroparticle Physics 18 (2002) 1-25.

[4] E. Aprile et al, "Material screening and selection for XENON100", Astropart. Phys. 35 (2011) 43-49.

[5] W. Maneschg et al, "Measurements of extremely low radioactivity levels in stainless steel for GERDA", NIMA 593 (2008) 448.

[6] I. Lawson and B. Cleveland, "Low Background Counting At SNOLAB", Topical Workshop on Low Radioactivity Techniques LRT 2010, AIP Conf. Proc. 1338 (2011) 68-77.

[7] Communication from L. Baudis.

[8] LUX Collaboration, communication from J. White.

[9] S. Leonard et al, "Systematic study of trace radioactive impurities in candidate construction materials for EXO-200", NIMA 591 (2008) 490.

[10] P. Finnerty et al, "Low-background gamma counting at the Kimballton Underground Research Facility", Nucl. Instrum. Meth. A 642 (2011) 65-69.

[11] V. Boccone et al, "Development of wavelength shifter coated reflectors for the ArDM argon dark matter detector", JINST 4 (2009) P06001, [arXiv:0904.0246].

[12] D. Budjas et al, "Gamma-ray spectrometry of ultra low levels of radioactivity within the material screening program for the GERDA experiment", Applied Radiation and Isotopes 67 (2009) 755.

[13] D. Budjas et al, "Highly sensitive gamma-spectrometers of GERDA for material screening: Part I", Proceedings of the XIV International Baksan School Particles and Cosmology Baksan Valley, Kabardino-Balkaria, Russia, April 16-21, 2007, [arxiv:0812.0723].

[14] NEXT Collaboration, Conceptual Design Report, "The NEXT-100 experiment for $\beta\beta0\nu$ searches at LSC', arXiv:1106.3630 [physics.ins-det].

[15] C. Faham, Presentation "Performance and Radioactivity Measurements of the PMTs for the LUX and LZ Dark Matter Experiments'" at TIPP2011, http://conferences.fnal.gov/tipp11/.

[16] ILIAS Database, http://radiopurity.in2p3.fr.

[17] S. Nisi et al, "Comparison of inductively coupled mass spectrimetry and ultra low-level gamma-ray spectroscopy for ultra low background material selection", Applied Radiation and Isotopes 67 (2009) 828.

[18] R. Luescher et al, "Search for bb decay in ^{136}Xe: new results from the Gotthard experiment", Physics Letters B 434 (1998) 407-414.

[19] A. Dobi et al, "Xenon purity analysis for EXO-200 via mass spectrometry", arXiv:1109.1046v1 [physics.ins-det].

[20] J. Busto et al, "Radioactivity measurements of a large number of adhesives", NIMA 492 (2002) 35-42.

[21] V. S. Uras et al, " Radon(Rn222) emanation results", SNO-STR-94-024 (1994)

[22] M. Liu et al (SNO), "Rn222 emanation into vacuum", Nuclear Instruments and Methods in Physics Research A329 (1993) 291.

[23] G. Zuzel, H. Simgen (GERDA), "High Sensitivity radon Emanation Measurements", Applied radiation and isotopes 67 (2009)889.

[24] F.J. Iguaz "Development of a Time projection Chamber with MicroMegas technology for the search of the Double Beta Decay of ^{136}Xe, THesis work, Zaragoza 2010.

Chapter 3

Next Project

3.1 NEXT Project

The NEXT project (NP) refers to the sharing, organization, coordination, tracking and resource management of the different tasks related with the construction, commissioning and operation of the NEXT-100 detector.

The NP defines the following main projects (there are a number of other projects related with R&D for a future upgrade of the detector not listed here).

1. **SHL:** Design and construction of lead castle, seismic structure and working platform.
2. **PV:** Design and construction of the NEXT-100 pressure vessel and inner copper shield.
3. **EL:** Design and construction of the field cage, EL grids, Light Tube and High Voltage feedthroughs.
4. **EP:** Design and construction of the energy plane enclosures and manifold.
5. **TP:** Design and construction of the tracking plane DBs and honeycomb support structure.
6. **PMT:** Procurement and characterization of PMTs.
7. **MPPC:** Procurement and characterization of MPPCs.
8. **FE-PMT:** Front end electronics for PMTs.
9. **FE-MPPC:** Front end electronics for MPPCs.
10. **GAS:** Gas system.
11. **DAQ:** Data acquisition and online monitoring.

12. **SLW:** Slow controls.
13. **RPY:** Screening of components, radiopurity measurements.
14. **RAD:** Radon depuration and monitoring.
15. **OFS:** Offline software (reconstruction, data processing).
16. **ONS:** Online software (DAQ, monitoring).
17. **QLTY:** Quality control.
18. **MC:** Monte Carlo simulation.
19. **CAL:** Calibration.

In addition, the NP defines the following super-projects (SP):

1. **INF:** Infrastructures: it includes the construction of lead castle, seismic structure and working platform (SHL), the construction and installation of the gas system (GAS) and radon systems (RAD), and the installation of miscellaneous services (gas, water, clean tent).
2. **DET:** Detector: it includes the construction of the pressure vessel (PV), field cage, EL grids, Light Tube and High Voltage feedthroughs (EL).
3. **ENE:** Energy plane: PMT procuration and characterization (PMT), construction of the energy plane enclosures and manifold (EP), coating of PMT windows.
4. **TRK:** Tracking plane: MPPC procuration, construction, testing and coating of DBs.
5. **ELE:** Front-end electronics for MPPCs and PMTs, DAQ.
6. **SSS:** Several software systems: It includes offline software (OFS), online software (ONS), slow control (SLW).
7. **BKG:** radiopurity measurements (RPY) background model, Monte Carlo implementation of background model.
8. **INT:** Integration (includes interface between the shielding and the pressure vessel, electrical services and gas services), as well as safety and risk analysis.
9. **ANA:** Services for analysis: It includes detector calibration (CAL) and quality control (QLTY).

In the following sections we describe these projects in more details

3.2 INT: Integration

Three closely related tasks during the construction phase of NEXT-100 are the technical coordination, the integration of the different systems at the LSC and the link with LSC staff. Rather than nominating different persons we have decided to nominate two technical coordinators (TC) that will share the three tasks. At the time of writing this TDR NEXT-100 technical coordinators are I. Liubarsky, from IFIC and T. Dafni, from UNIZAR. The INT project defines a group that includes the two TC, a coordinating engineer from UdG for the shielding, a coordinating engineer from IFIC for the apparatus, an a coordinating engineer from UPV for the electronics, in addition of the LSC staff.

3.3 INF: Infrastructures

The infrastructures super-project includes the construction of the working platform for NEXT (a requirement of the LSC), the construction of the lead castle, gas system (including recovery and emergency recovery) and radon system, and a number of miscellaneous services: water, electricity, gases such as argon and nitrogen, working clean room (in site) for detector maintenance) etc. Below we describe the three main projects in this SP.

3.3.1 SHL: Design and construction of lead castle, seismic structure and working platform

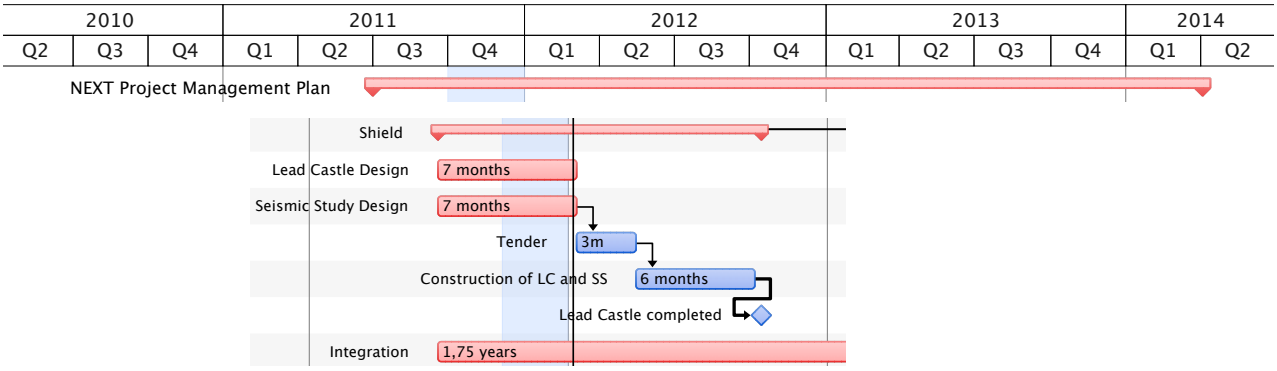

Figure 3.1: SLD project

The design of the three systems has been described in chapter 9 and chapter **??**. The project is jointly coordinated by UPV and UdG. This project requires very close coordination with the LSC and thus involves heavily the two TC.

The project status in summarized in Figure 3.1. The design of the shielding, detector pedestal and platform has been completed by the NEXT collaboration, taking into account our own seismic study and we are now interacting with LSC stuff to define the final details of construction and installation. Constructive drawings should be available

early in 2012 and tender for the construction of the platform could start no later than February, 2012. We are also ready to proceed to the procurement and conditioning of lead bricks. Construction of the lead castle can proceed at the same time than the platform.

This project requires very close coordination with the LSC and thus involves heavily the two TC.

None of the systems integrating this project were budgeted in the CUP proposal. Thus funding other than CUP is needed to finance them.

3.3.2 GAS: Gas system

The design, construction and installation at LSC of the gas system is a join project between UNIZAR and IFIC. The design of the gas system is now essentially completed, and procurement of the parts has already started (chapter 8). The gas system will be payed by CUP. The system needed in 2013 is almost identical to the systems developed at UNIZAR and IFIC for the large NEXT prototypes, with the exception of the pump, which will be triple diaphragm, all-metal seal. A suitable manufacturer for the NEXT-100 pump has already been identified and the process of purchasing will start early next year. The first version of the gas system will be operative no later than September 2012 and gradual improvements will continue for about a year. Our goal is to have a system ready for enriched xenon by mid 2013.

3.3.3 RAD: Radon monitoring and suppression

The design, construction and installation at LSC of the radon monitoring and suppression system is a UNIZAR project. Preliminary design of the system (which does not need to be in place during initial operation) has also been described in chapter 8. Our goal is to have a system ready by mid 2013.

3.4 DET: Detector

The detector super-project refers to the construction of the NEXT-100 apparatus itself (chapter 4). It includes the construction of the pressure vessel and inner copper shield (PV), and the electrical and optical system: field cage, EL grids, HVFT and light tube.

3.4.1 PV: Design and construction of the NEXT-100 pressure vessel and inner copper shield

The PV project is jointly coordinated by LBNL and IFIC. Its status in summarized in Figure 3.2. The design has been completed and the construction specifications, according to the ASME norm have been defined. The project is now in the final phase of identifying a suitable contractor to build the chamber (we have already identified two experienced companies and will decide soon between them). Tendering should proceed no later than February, 2012. The construction firms estimated 3 months as the needed construction

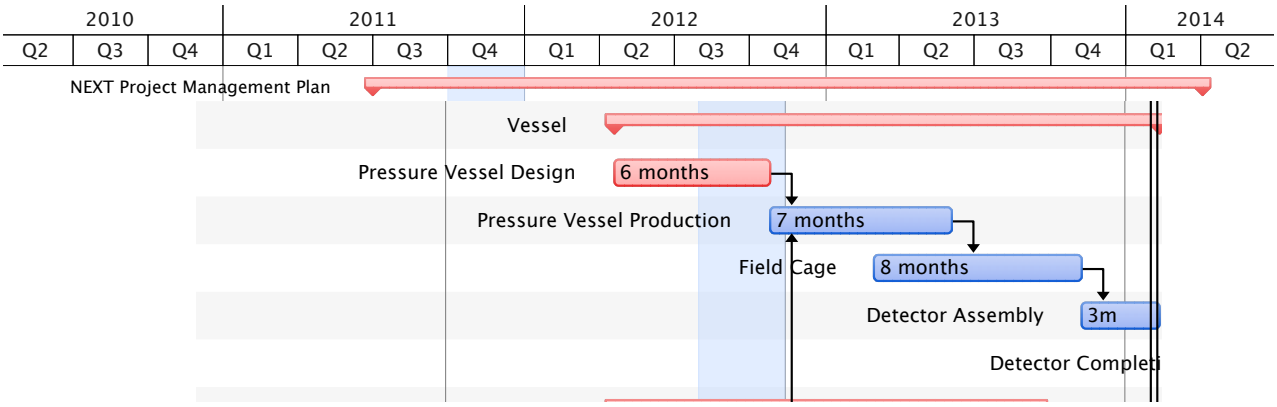

Figure 3.2: PV+EL projects

time (the short construction time is possible thanks to the choice of stainless steel as construction material). Allowing 2 months for contingency, the PV should be ready in July 2012. We foresee stress and pressure tests during September and October at the factory. The PV can then be shipped to the LSC by November 2012.

The cost of the chamber will be covered by CUP. The cost of the ICS was not foreseen in CUP. Thus funding other than CUP is needed to finance it.

3.4.2 EL: Design and construction of the field cage, EL grids, Light Tube and High Voltage feedthroughs

The design of the FC, EL grids, LT and HVFT has been described in chapter 4. TAMU coordinates and is the main force behind this project. The group from Texas has built the same elements for the NEXT-DEMO detector and has extensive experience in each of the aspects involved. The design of the FC+LT is well advanced, and the HVFT will be very similar to those already tested by NEXT-DEMO. Some R&D is still necessary to decide on optimal solutions for the EL grids. However, all the relevant parts should be built and shipped to LSC before the end of 2012, as shown in Figure 3.2.

The cost of the systems will be covered by US funds.

3.5 ENE: Energy plane

The energy plane super-project includes the procurement and characterization of the PMTs, and the fabrication of the PMT enclosures, and central manifold.

3.5.1 EP: Design and construction of the energy plane enclosures and manifold

The design and construction of the energy plane (Figure 3.4) cans and manifold has been described in chapter 4. LBNL coordinates and is the main force behind this project.

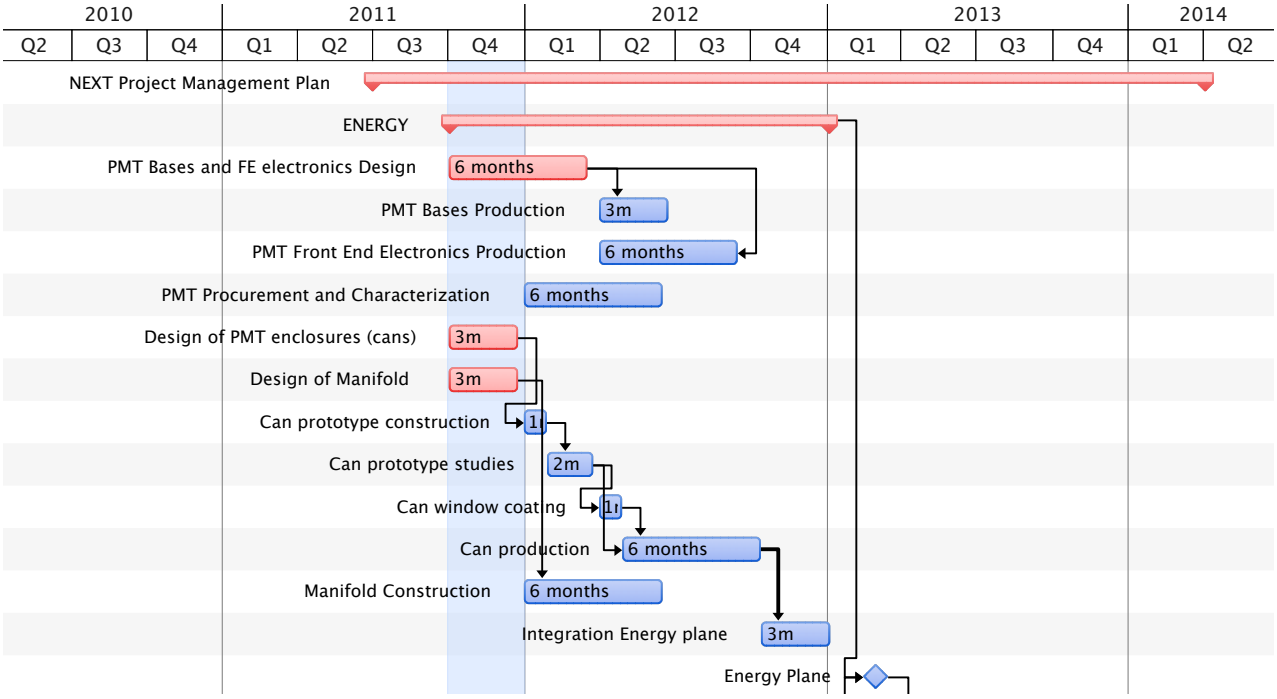

Figure 3.3: EP project

The design of the enclosures and manifold is essentially completed and prototypes are being built. Our goal is to complete construction and testing of the full system before the end of 2012.

The cost of the system will be covered by US funds.

3.5.2 PMT: Procurement and characterization of PMTs

The PMTs are being ordered by IFIC and payed using CUP funds. A testing procedure to certify the response of the PMTs is under development at IFIC. Calibration of the PMTs will be done in the detector itself, using light diodes to measure the single photoelectron peak and thus the gain of each individual device connected to the full electronics chain. However some 20% of the PMTs will be fully characterized also at the IFIC laboratory.

3.6 TRK: Tracking plane

The tracking plane super-project refers to the procuration of the MPPCs, and the construction, testing, coating and assembly of the DBs.

3.6.1 TP: Design and construction of the tracking plane DBs and honeycomb support structure

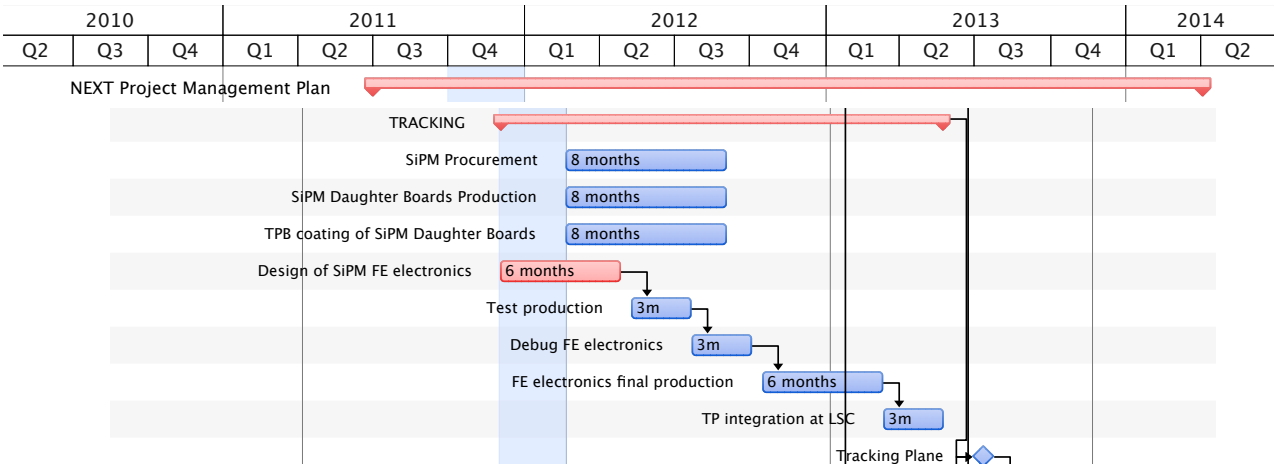

Figure 3.4: TP project

Figure **??** shows the evolution of the TP project. The design of the NEXT-100 DB is now under way at IFIC (which designed the DB for NEXT-DEMO). IFIC will also design and build the honeycomb structure to hold the DBs.

The MPPCs will be delivered during a period of 7 months, starting in early 2012 and at a rate of 1 000 a months. DBs will be fabricated and tested, at a ratio of about 15 a month during the same period. DBs will be shipped to IFIC once fabricated and tested, for coating, final testing and quality certification and vacuum storage.

The cost of the MPPCs, tracking plane support structure and DBs will be payed by CUP and by UAN.

3.7 ELE: Electronics and DAQ

3.7.1 Data acquisition and online monitoring

This project will be coordinated by UPV. The DAQ for NEXT-100 will be very similar to the DAQ developed for NEXT-DEMO, which is currently working very well. It has the advantage of being part of a large collaborative development in the contest of the RD51 collaboration. Details of the final DAQ solutions together with the construction plan will be defined in the second part of this TDR.

3.7.2 Front end electronics for PMTs

The design of the FE electronics and radiopure bases for the PMTs is a join project between IFIC and LBNL. The FE electronics for the PMT will be very similar to the FE electronics developed for NEXT-DEMO (chapter 6).

3.7.3 Front end electronics for MPPCs

The design of low-background FE electronics for the MPPCs to be installed inside the chamber is a join project between UPV and LBNL. The design is discussed in chapter 6.

3.8 Coating of DB, PMT enclosure windows and light tube with TPB

This is a join project between IFIC, ICMOL and LBNL. IFIC has developed the expertise to coat surfaces by evaporation. A precision evaporation machine available at ICMOL allows the coating of DBs and sapphire windows, while the large evaporator, available also at IFIC will be used to coat the light tube.

LBNL will be studying the technique of coating by polymer matrix containing TPB, as an alternative (faster) solution for coating sapphire windows.

With the expertise available in both institutes, TPB coating can proceed on schedule. DBs will be shipped from UAN once mounted and tested and cleaned, coated and stored at IFIC. Sapphire windows will be coated by evaporation of polymer matrix before mounting them in the PMT envelopes. The light tube will be coated in the large evaporator before final installation at LSC.

3.9 Screening of components, radiopurity measurements

The screening of materials for NEXT-100, including measurements at the LSC and elsewhere, as well as the elaboration of the background model is a shared project between UNIZAR and UAM, with the help of the LSC. The current status of the radiopurity measurements and the initial background model for NEXT has been discussed in chapter 2. The UNIZAR group has a long experience in this area and has been leading the studies so far. The UAM group, which has just joined NEXT has developed experience working with Ge detectors in the context of the Super-Kamiokande (Gazooks) project and will contribute to the intensive program of measurements and analysis.

3.10 SSS: Software

3.10.1 Offline software and quality control

The development of the offline reconstruction software and the Monte Carlo, including the Monte Carlo model will be a join project between IFIC (reconstruction framework, software tools, Monte Carlo toolkit), U. Santiago (reconstruction algorithms), U. A. Nario (reconstruction, Monte Carlo background model) and U. Zaragoza (background model). In addition, data quality control will be the responsibility of U. Santiago, U. Aveiro and U. Coimbra.

3.11 SSS: ANA

3.11.1 Calibration

The development of calibration strategies (and equipment where needed) for NEXT will be the responsibility of Iowa State University.

3.12 Slow controls

This project will be the responsibility of the groups of Coimbra and Aveiro.

Part II

Technical chapters

Chapter 4

Pressure vessel and field cage

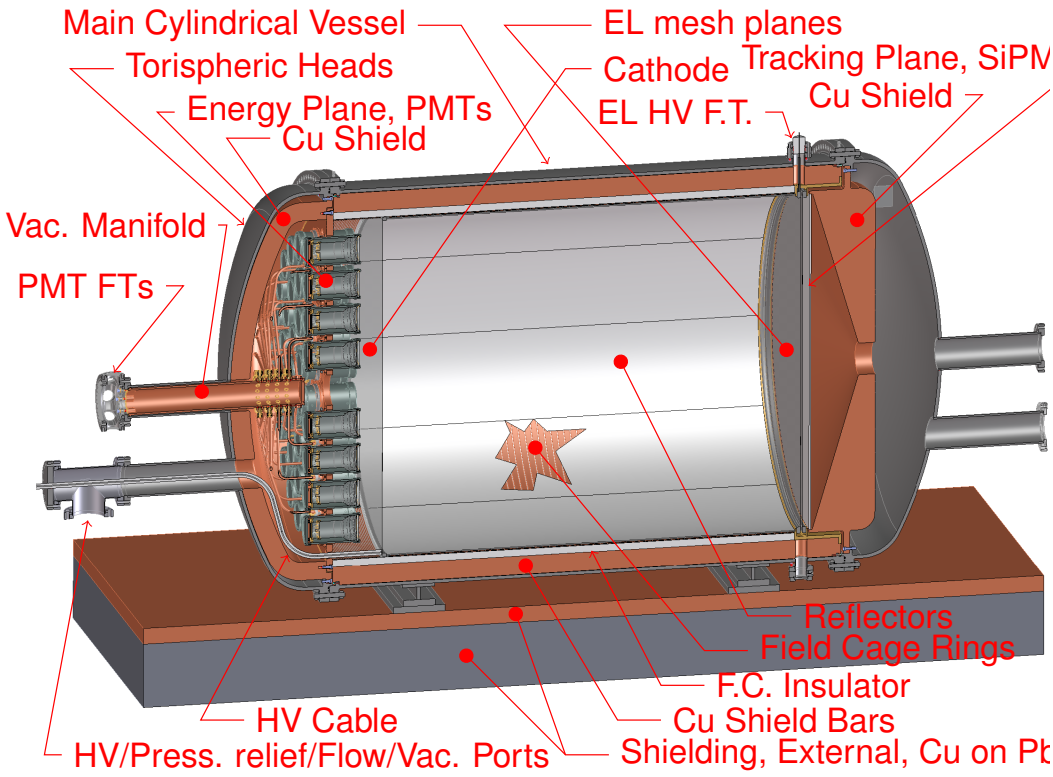

Figure 4.1: The NEXT-100 apparatus.

We define the NEXT-100 apparatus (Figure 4.1, and Figure 4.2) as composed by the following subsystems:

1. The pressure vessel (PV).

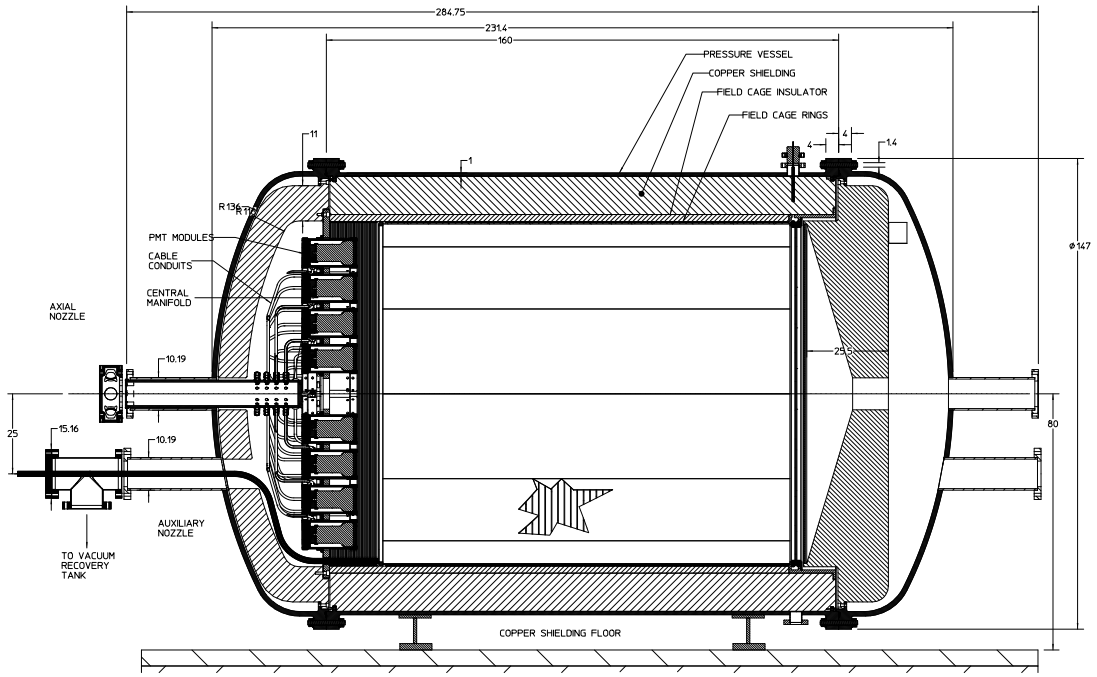

Figure 4.2: NEXT-100, longitudinal cross section

2. The inner copper shielding (ICS).

3. The field cage (FC).

4. The EL grids (ELG).

5. The light tube (LT).

6. The high voltage feedthroughs (HVFT).

In this chapter we describe the detailed design of each one of this subsystems. The energy and tracking plane are described in a separate chapter devoted to sensors.

4.1 The pressure vessel and the inner copper shielding

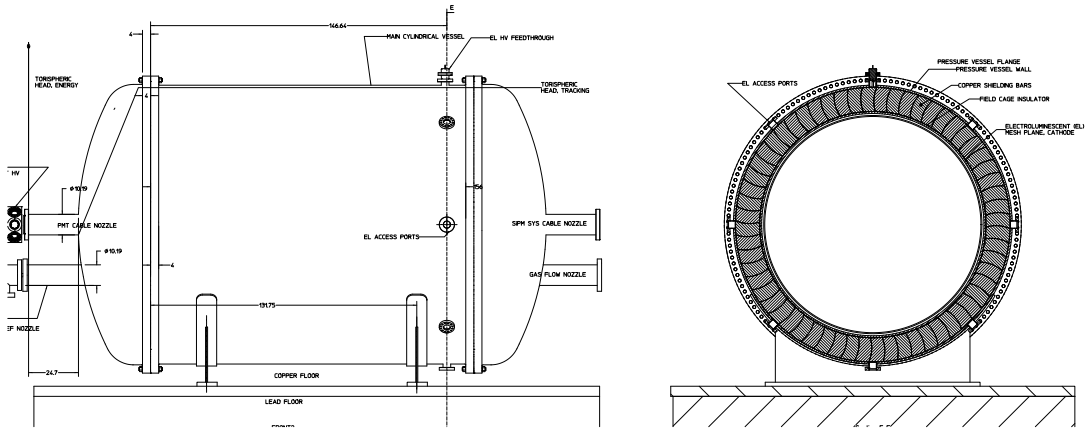

Figure 4.3: Pressure Vessel/Detector, Side and End Cross Section Views

The design of the pressure vessel (PV) has undergone significants changes and simplifications since the publication of the CDR. These are:

- Vessel design simplified.
- Vessel axis changed from vertical to horizontal
- Vessel material changed from titanium to stainless steel.
- Inner copper shield added to attenuate the background coming from the vessel and the residual background coming from the lead shield.
- PMT enclosures independent of the head.

The PV (Figure 4.2) consists of a cylindrical main section having near identical torispheric heads on each end. Both heads are convex (as viewed from outside) and each have two nozzles, one for for services (power and signal cabling) and the other for gas flow/pressure relief. The PMT enclosures are independent from the head, and located fully inside the vessel allowing for a much simpler head design. The vessel orientation is horizontal, so as to minimize the overall height, which reduces the shielding cost and allows essentially unlimited length on each end for cabling and service expansion.

The vessel supports all internal components, and the design is quite modular; one head fully supports and contains the entire PMT system (energy plane), the other head fully supports and contains the SiPM system (tracking plane), and the main vessel fully supports and contains the field cage and mesh plane system. The drift section cathode plane high voltage feedthrough is integrated into the energy plane head and makes contact with the cathode plane when the head is assembled. The supports for these internal systems are a set of internal flanges, one incorporated into each main flange (4 total).

The simpler vessel design will significantly reduce cost, time, and risk in the fabrication; it is now very similar to a standard pressure vessel, which all qualified manufacturers will be familiar with. The decoupling of the vessel from the internal systems allows us to get an early start on the vessel fabrication, and allows for further refinement and development of these systems, should this be necessary.

The vessel material is now 304L or 316L Stainless steel. There are several reasons why we have abandoned titanium as construction material for the first version of the NEXT-100 detectors. These are:

1. Measurements of the activity of several samples of titanium, carried out by our collaboration as well as by other groups have not yield conclusive results, as shown in chapter 2. Specifically, our requirements were a maximum activity in uranium and thorium of the order of 100 μBq/kg, that would have resulted in a total PV activity of about 0.4 Bq. Contrarily to our expectations none of the measured sampled verified this condition, and most of them were found to have a level of activity 3 to 10 times larger.

2. Conversely, existing measurements of stainless steel, in particular by the XENON collaboration (see chapter **??**) show that it is possible to secure SS with an activity in the range of 1-2 mBq/kg, which is of the same order than the activity measured in some titanium samples.

3. While titanium has many attractive features, including its lightness and (for some grades) its resistance to stress, it has also a number of disadvantages with respect to SS, including: (a) a much higher cost, (b) more complexity in the fabrication process, that eliminated many potential manufacturers and increased the construction risks, (c) much restricted availability of parts, (d) more difficulties to accommodate the ASME standards, and (e) more difficulties for the risk assessment study, since titanium PV are way less common that SS PV.

Last, but not least, we realized that our shield design included a thick copper shield, which was essential to attenuate the residual radiation arising from the external lead shield. On the other hand, moving the copper shield *inside* the PV has the obvious benefit of reducing the copper surface needed (thus the total mass, and therefore the cost), and in addition it attenuates the activity arising from the PV by two orders of magnitude. Consequently we decided to follow the approach taken by the XENON collaboration and fabricate a reasonably radiopure stainless steel vessel lined with an inner copper shield (ICS).

It appears feasible to obtain 304L/316L stainless steel of an activity less than $\sim$5 mBq/kg in the uranium and thorium series. After the ICS the residual activity would be reduced to some 50 μBq/kg, for a total vessel mass of 1.2 tons, which is also lighter than in the titanium vessel version (in spite of the higher density of SS) due to the elimination of the heavy service flanges. Thus the residual activity due to the PV (after the ICS) is smaller than 0.1 Bq. One needs to ad the residual activity of the ICS itself which is also smaller than 0.1 Bq (using copper of $\sim$10 μBq/kg, which is available from a number of suppliers, see chapter 2). Thus, the resulting activity of the whole system is smaller than that foreseen in the CDR.

The ICS will be made of straight copper bars, and where relevant flat plates, which are straightforward to fabricate. It does not introduce any significant complication in the design.

The basic parameters and dimensions of the pressure vessel are shown in table 4.1. The vessel will be built strictly to ASME pressure Vessel Design Code, sec VIII.

4.1.1 Sealing

All pressure sealing flange joints that are exposed to atmosphere on the outside are sealed using double O-rings in grooves. The inner O-ring is for pressure sealing; the outer O-ring serves not only as a backup, but also to create a sealed annulus which can be continuously monitored for leakage by pulling a vacuum on it with an RGA monitor (sense port). Figure 4.1.1 shows a cross section detail of the head to vessel flanges; nozzle flanges are similar.

Xenon will permeate (very slowly) through these O-rings and will need to be recovered by a cold trap (see below). The total amount, using butyl O-rings is estimated to be $<$200 gram/year. This may be even further reduced by using an ultra-low permeability polymer such as PCTFE.

Double O-ring seals will also be used on the nozzle flanges, however, the flanges

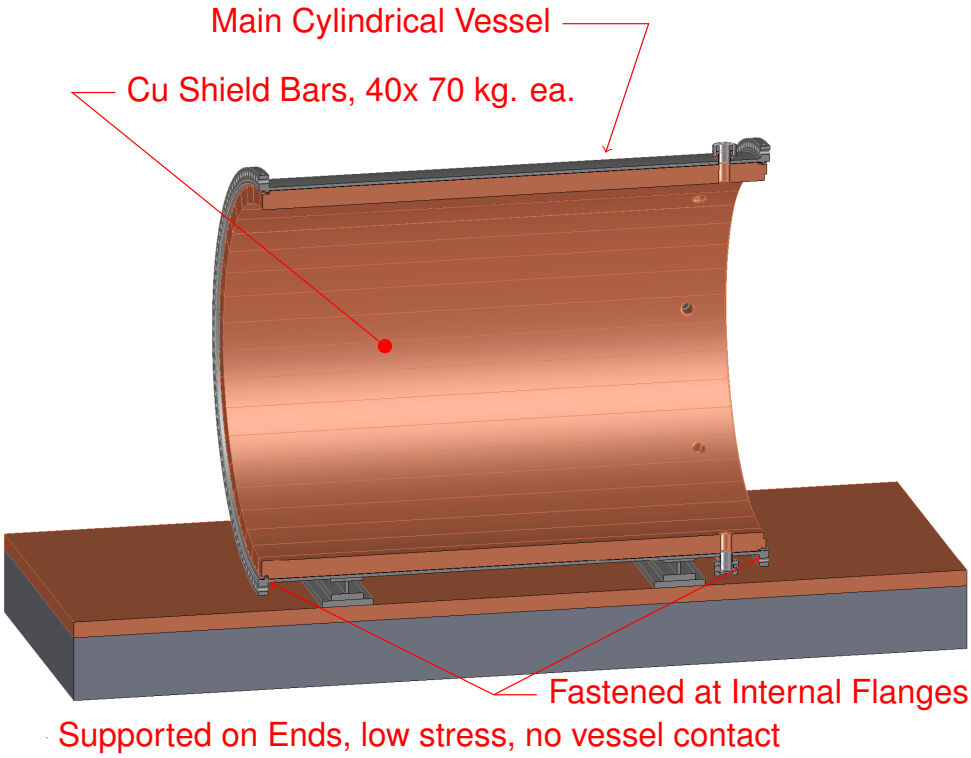

Figure 4.4: The NEXT-100 ICS

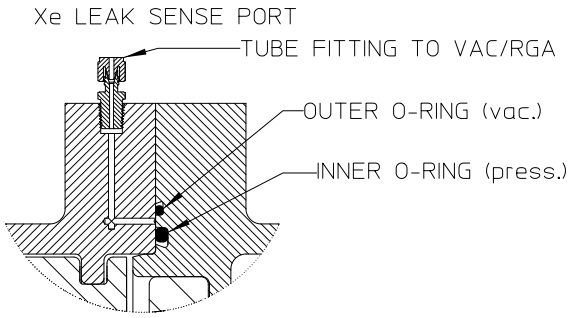

Figure 4.5: Double O-ring/sense port detail

Table 4.1: NEXT100 Pressure Vessel Parameters

Parameter	qty	units
Maximum Operating Pressure (MOP)	15.0	bar (abs)
Maximum Allowable Working pressure (MAWP)	16.4	bar (abs)
Minimum Allowable Pressure (external	1.5	bar (abs)
Inner diameter	130	cm
Outer Diameter, Vessel	131	cm
Outer Diameter, Flanges	147	cm
Length, inside shielding	2.22	m
Length, end to end, axial	2.85	m
Vessel and head wall thickness	10	mm
Head crown radius, internal	130	cm
Head knuckle radius, internal	13	cm
Flange thickness, head to vessel (both)	3.5	cm
Bolt Diameter, head to vessel flanges	14	mm
Bolt length, head to vessel flanges	9	cm
Number of Bolts, each head to vessel flange	150	
Mass, Vessel and both heads	1200	kg
Mass, Copper shielding	9000	kg

welded to the pressure vessel will be flat faced, and the O-ring grooves and sense ports will be added to an interface flange.

The central nozzle of the energy head (and possibly the tracking plane head) has a CF flange (DN100) as it is not a pressure sealing surface; instead pressure is sealed by the Central Manifold which bolts to the underside of this flange, inside the vessel. The central manifold seals with a single O-ring as there is a vacuum inside which leads to a large evacuated recovery cylinder, so any xenon leakage can be sensed and recovered in a cold trap. Figure 4.1.1 The recovery cylinder is large enough to vent the entire vessel of 15 bar such that the resulting pressure is no more than 1 bar absolute. The flange to octagon joint is however strong enough to withstand the full 15 bar.

4.1.2 Bolting

The head to vessel flange bolts are Inconel 718; this is the highest strength noncorrosive bolting material allowed in the ASME code and it appears to be reasonably radiopure (chapter 2). Flange thickness and outer diameter are substantially minimized by using highest possible strength bolting. The O-ring sealing also allows bolt tension to be reduced from the CDR design, and these bolts can be tighten by hand using large wrenches. There are 120 bolts per flange.

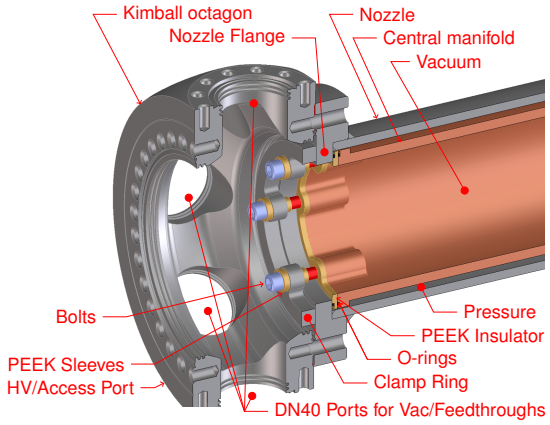

Figure 4.6: Central Manifold/ Nozzle Flange Seal

4.1.3 Pressure Relief

Pressure relief is provided though one or more of the auxiliary nozzles. Currently the energy plane head auxiliary nozzle is used and the port has a T-shaped interface to allow gas flow/pressure relief function to coexist with the drift cathode high voltage cable feedthrough. The auxiliary nozzles are designed to vent the pressure vessel to the recovery cylinder under 1 minute or less. The auxiliary port will have a fast acting pressure signal actuated high flow capacity pressure relief valve or burst disk on the auxiliary port which vent to the recovery cylinder. Proper activation should vent the vessel in approx. 1 minute, limiting loss of xenon through the broken feedthrough to no more than 10% of total. Reaction force is considerable, about 10 kN. The nozzle will require a rigid brace clamping it to the floor of the support frame, since the outside shielding disallows the addition of bracing gussets between the nozzle and the head shell.

Apart from this, it is required to have a passive relief valve as well, this will also vent to the evacuated recovery cylinder. This valve is of a smaller flow capacity, since the only known condition creating an overpressure would be a fire in the LSC hall or broken supply regulator. We have only a limited amount of xenon, so a broken regulator cannot create an overpressure condition. Sizing for fire, using API methodology a 1 cm diameter vent line is required. Reaction force for this condition is very small.

The vessel and detector are mounted on a movable seismically isolated platform, and they connect to the recovery cylinder which is too large to share space on the seismic platform, which must be mounted to the LSC hall floor. There can be relative motion of up to 100 mm between the platform and the LSC hall, so the connection to the recovery cylinder, will be by a pressure rated flexible couplings. The piping ends of the recovery cylinder also need to be rigidly braced to the LSC hall floor.

4.1.4 Assembly

The central cylindrical vessel will be bolted through the shielding floor to the seismic platform below. Footings will be welded to the vessel wall, as is standard practice. The heads will be attached to movable carriages that slide on precision rails bolted to the floor.

4.1.5 Vessel Construction

The vessel will be fabricated following the ASME standards. In particular, welding will be done using the gas tungsten arc (GTAW) process. particular care will be take to avoid use of thoriated tungsten electrodes, (and guns used with such).

To assure that the high dimensional tolerances are achieved, particular care in the construction sequence will be made, in particular, several stress relieving treatments will be required, some or all of them a full solution anneal (driving all carbides back into solid solution). Details will be worked out with the manufacturer, and specified in the User Design Specification, (available in the NEXT web page).

4.2 Field Cage, EL, HVFT and LT

Parameter	Value
E/P	3.0 $kV*cm^{-1}*bar^{-1}$
Drift field	0.3 kV/cm
Pressure	15.0 bar
EL grid gap	0.5 cm
Drift length	127 cm
Gate grid voltage	-22.5 kV
Anode grid voltage	0
Cathode voltage	-58 kV
Optical gain	2500 photons/e^-

Table 4.2: NEXT-100 EL grid parameters

The NEXT-100 field cage (FC) is shown in Figure 4.7 and the EL parameters are shown in Table 4.2. The main body of the FC will be a high density polyethylene (HDPE) cylindrical shell with a 2.5 cm wall thickness. The drift region will consist of OFHC copper strips connected with low background resistors. There is also a buffer region between the cathode and PMTs which will be used to degrade the high cathode voltage safely to ground. Figures 4.8 shows the field lines defining the fiducial volume in the drift region of the TPC. Using the parameters in Table tab.TL, the electric field varies <3% across the fiducial volume. The light tube will consist of thin sheets of Tetratex^{TM} (TTX), fixed over a 3M^{TM} substrate. The TTX will be vacuum coated with

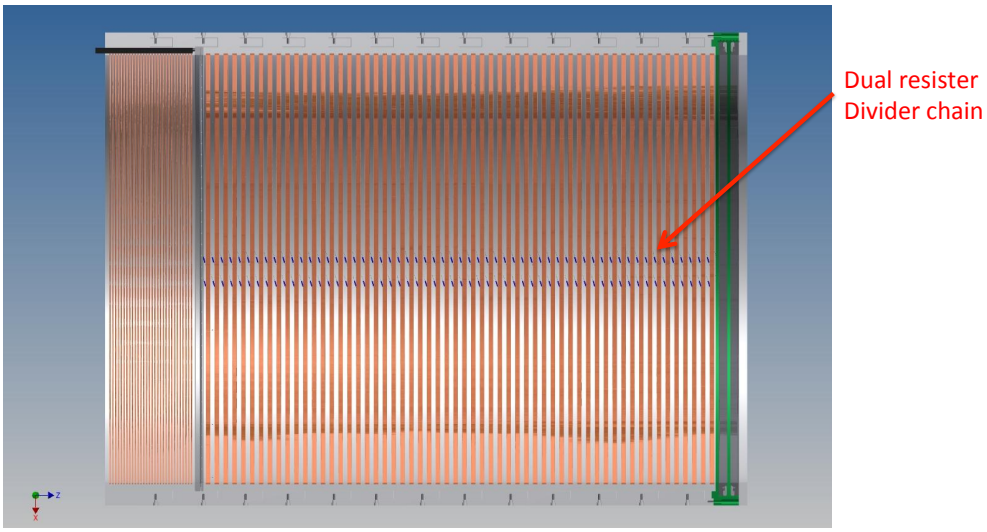

Figure 4.7: NEXT-100 Field Cage

tetraphenyl butadiene (TPB) wavelength shifter to maximize the light yield. The ArDM collaboration has measured a reflectance coefficient at 430 nm close to 97% for a wide range of coating thicknesses. In addition, the light yield measurements showed no aging effects (see chapter 7 for more details).

4.2.1 High Voltage Feedthrough

The cathode high voltage feedthrough (HVFT) will be constructed using a compression seal approach as illustrated in Figures 4.9 and 4.10. A metal rod is pressed into a plastic tube (Tefzel or FEP, which have a high dielectric strength) which is then clamped using plastic ferrules from both the pressure side and air side. A sniffer port is placed between the seals to assure that xenon is not leaking. The feedthrough will be attached to a flange located on the energy plane end-cap. A shielded cable will be connected to the feedthrough and placed through the PMT support plate. The unshielded portion of the cable, with an additional resistive coating, will then run along the inside of the buffer field rings and mate with the cathode via a spring loaded junction. This approach, with the exception of the resistive coating, has been used in NEXT-DEMO, where a cathode voltage of 45 kV has been achieved. A smaller prototype was tested to 100 kV in vacuum and 70 kV in nitrogen at 3 bar. It has been demonstrated to be leak tight at 10 bar xenon and 10^{-7} mbar vacuum.

Figure 4.8: Electric field lines (*red vertical lines*) and equipotential contours are shown in a 50 cm section of the drift region. The lines are fairly uniform starting from a distance of approx. 2 cm from the field cage inner wall surface.

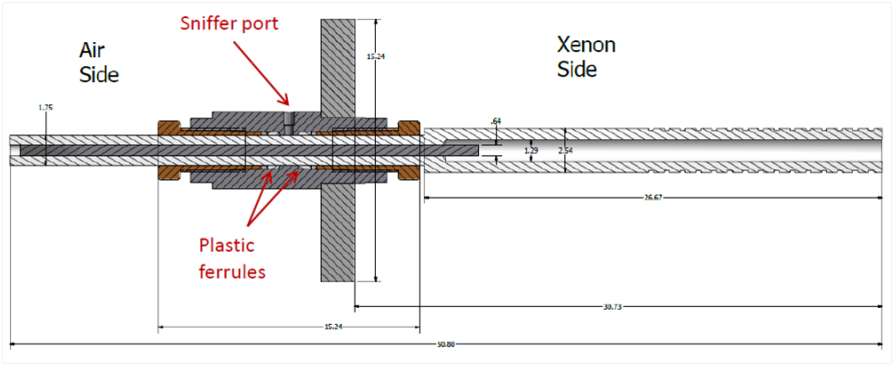

Figure 4.9: Cathode high voltage feedthrough (HVFT) designed for up to 100 kV operating voltage.

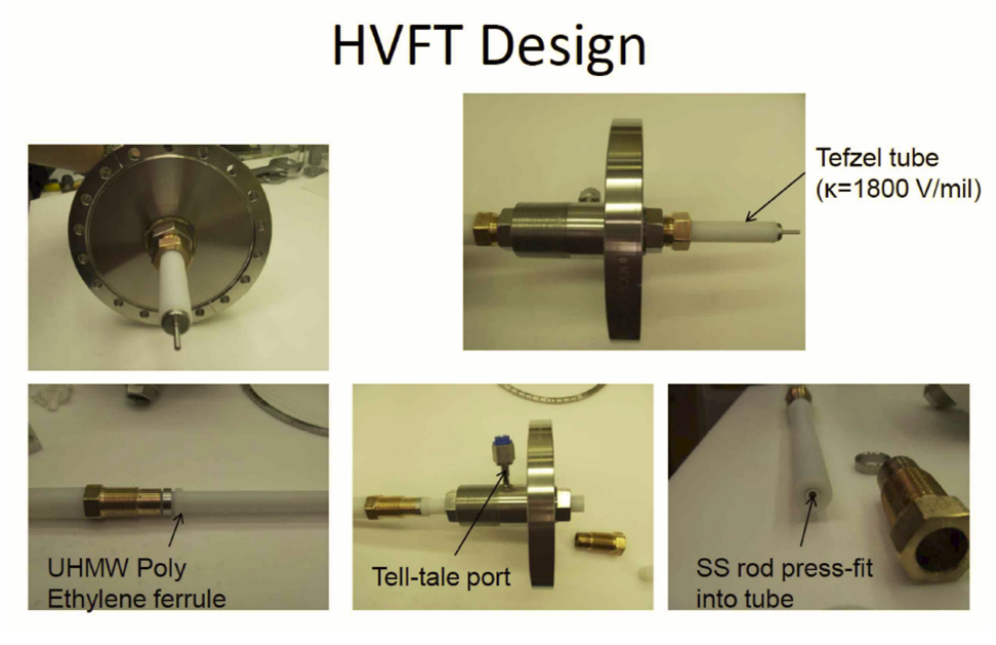

Figure 4.10: Cathode HVFT used in NEXT-DEMO.

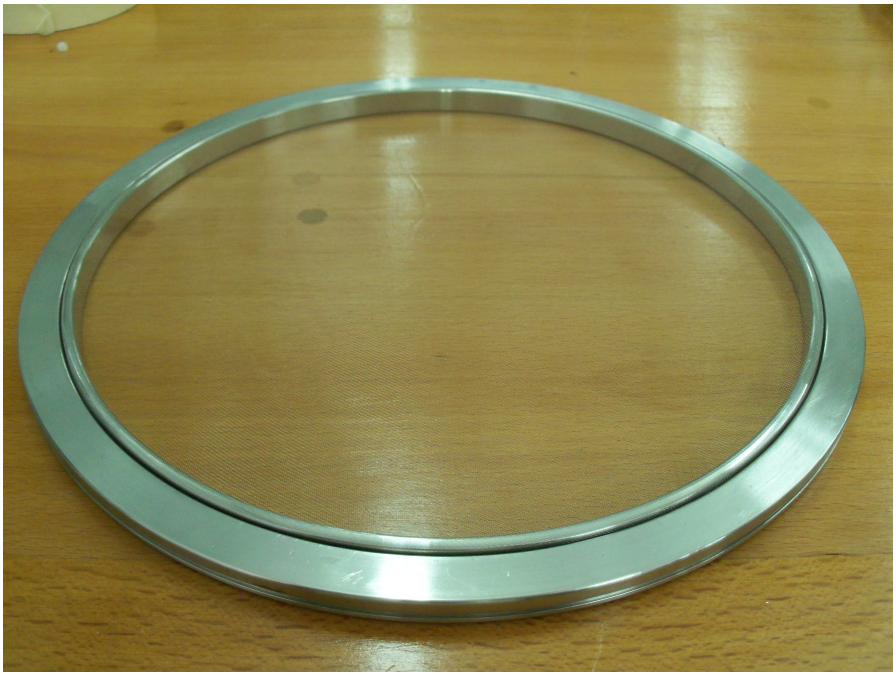

Figure 4.11: EL grids used in NEXT-DEMO

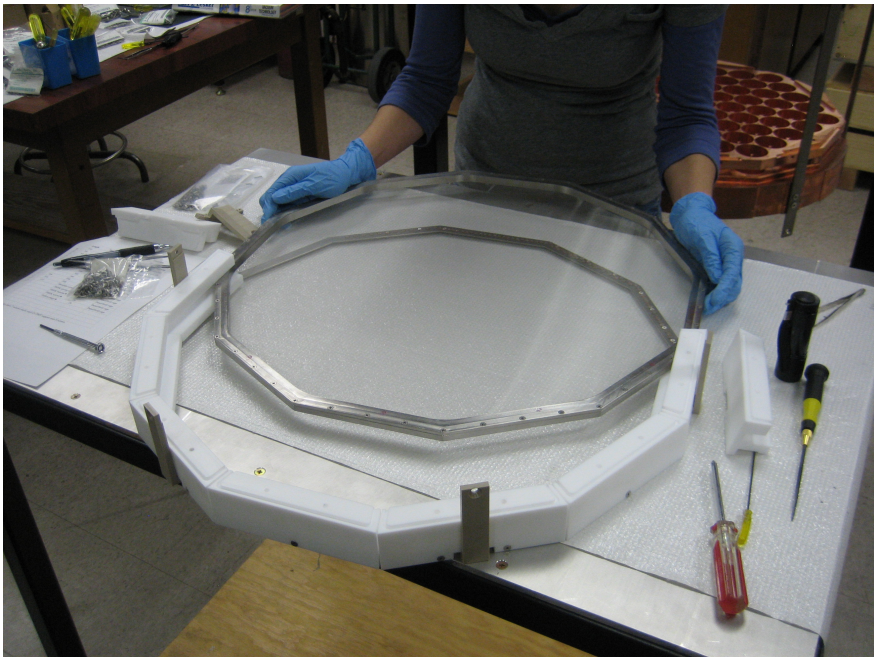

Figure 4.12: EL grids built for LUX by the Texas A&M (TAMU) group

4.3 Electroluminescent Grids

Figure 4.11 shows the electroluminescent (EL) grids built for the NEXT-DEMO prototype. The grids were constructed using a stainless steel mesh with pitch 0.5 mm and wire diameter 30 microns, which results in an open area of 88%. The grids are formed by clamping in a ring with a tongue and groove to hold the mesh and using a tensioning ring that is torqued with set screws to achieve the optimum tension. One important issue is that for the large diameter required in NEXT-100, preliminary estimates show that electrostatic attraction will cause the EL grids to bow considerably. This can be remedied by using a larger gauge wire. For example, a wire mesh is available with 90 micron wire diameter made from titanium with a similar open area. We are also investigating the use of titanium or copper grid frames to minimize the radioactive budget. In any case, the TAMU group, responsible of the design and construction of the NEXT-100 grids has already built the LUX grids (Figure 4.12) which have similar size en spacing.

Chapter 5

Sensors

5.1 The energy plane

5.1.1 Choice of the photomultiplier

The photomultipliers chosen for NEXT-100 are the R11410-10 (also called R11410MOD) model from Hamamatsu (Figure 5.1). This are large tubes, with a 3" photocathode and low levels of activity of the order of 3 mBq per unit in the Uranium and 2 mBq per unit in the Thorium series, the only relevant backgrounds for NEXT (Figure 5.2). The QE of the R11410-10 model is around 25% both in the VUV and in the blue region (Figure 5.3).

5.1.2 PMT coverage

The PMT's have a double function in NEXT. They are used to detect the fast scintillation signal (S_1) needed to localize the event in the z coordinate and they measure the total energy of the event. Therefore they have to count enough fast scintillation photons to establish unambiguously the existence of a S_1 signal, and they have to count enough secondary (EL) photons per primary electron as to minimize the contribution of the sensor (e.g., compared to the Fano factor) to the energy resolution.

Let's first consider the detection of scintillation light. The number of photons that arrive to the PMT housing windows depend of the properties of the reflector as well as the transparency of the EL grids. Our simulation shows that a light tube of 90% reflectivity (e.g., TTX coated with TPB) will transfer 9% of the primary VUV photons to the energy plane.

Assume now that an event is produced near the EL grids (the worst scenario for the detection of primary scintillation light with the cathode PMTs). The number of primary scintillation photons produced per MeV is 13158 [7]. The number of photoelectrons (pes) detected by the PMTs at the cathode is then:

$$(13158\ photons/MeV) \times C \times T_R \times T_W \times QE$$

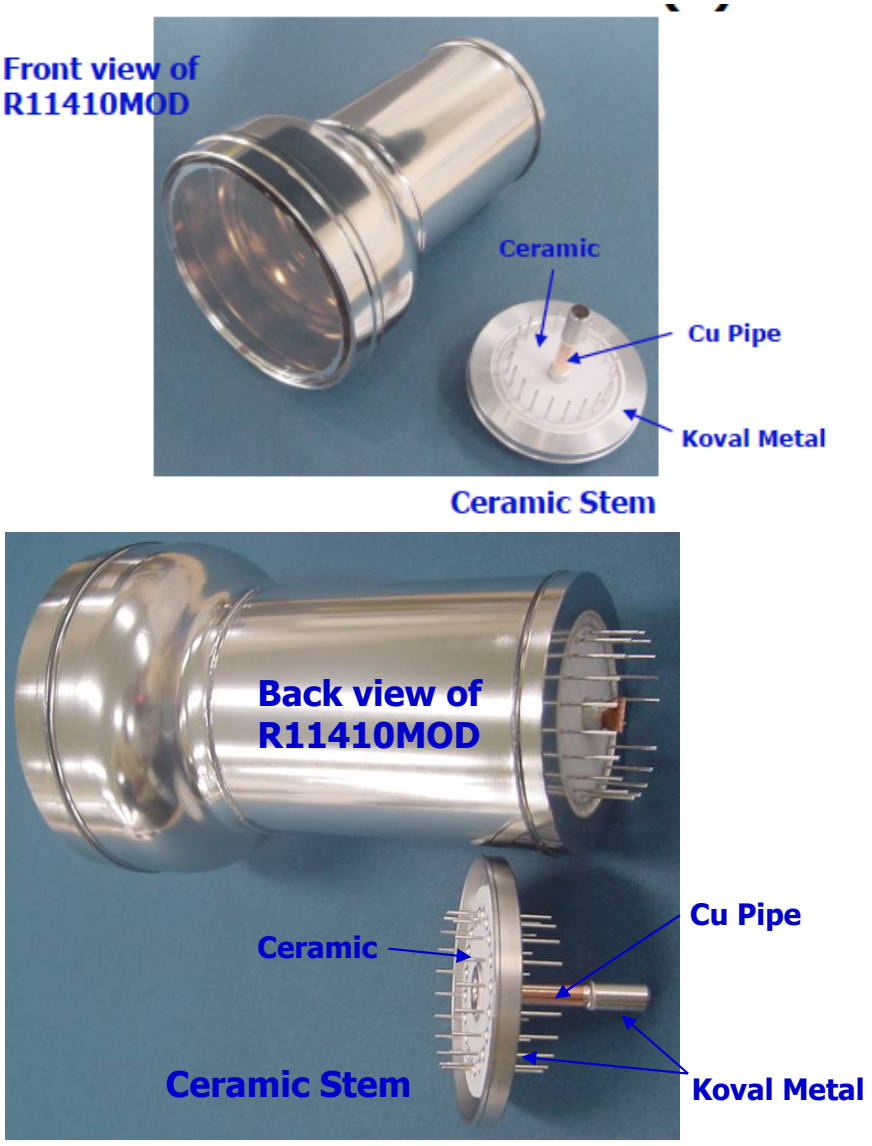

Figure 5.1: The Hamamatsu R11410-10 phototube. This is a large PMT, 3" in diameter, with an average radioactivity of 3.3 mBq for the U chain and 2.3 mBq for the Th chain.

RI Level for R11410MOD

Estimated RI level

< Unit : mBq/PMT >

Materials	Weight (g)	40K	U	Th	Co60	Sub Total
Quartz Faceplate	35	0.0	0.2	0.4	0.1	0.7
Metal Bulb	95	5.7	2.9	1.0	3.5	13.1
Stem (ceramic)	25	0.0	0.0	0.7	5.5	6.2
Insulating Plates	16	0.0	0.1	0.2	0.0	0.3
Electrodes	31	0.0	0.1	0.0	0.0	0.1
Total	202	5.7	3.3	2.3	9.1	20.4

Expected RI level : 10~30 mBq/PMT

Figure 5.2: Activity of the R11410-10 phototube.

Typical QE Curve

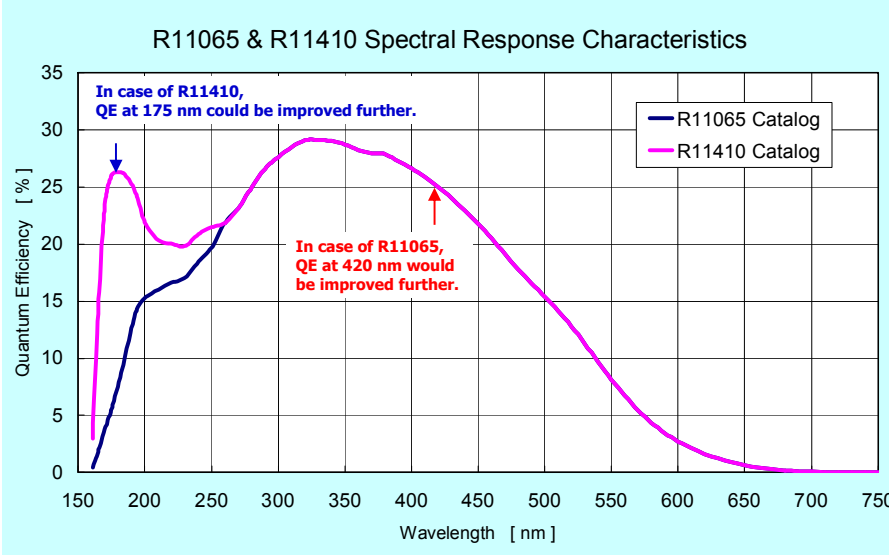

Figure 5.3: QE of the R11410-10 phototube.

where C is the cathode coverage, T_R is the reflector transfer function (0.09), T_W is the housing window transfer function (0.4 for a sapphire window coated with TPB) and QE is the PMT quantum efficiency (0.25). We obtain then:

$$(13158 photons/MeV) \times C \times 0.09 \times 0.5 \times 0.25 \sim 1.5 \times C \ (pes/keV)$$

for a signal of 10 keV NEXT detects, therefore, $15 \times C$ pes. A coverage of 30% results in 5 pes. PMTs can count single photoelectrons. A signal with 45photoelectrons can be identified by our pattern recognition program with an efficiency larger than 95%. Thus, $C = 0.3$ allows to detect S_1 in the full $\beta\beta$ spectrum, and in fact it allows to looks for weak signals such as those expected for WIMPS.

Consider now EL light. As shown in our CDR [7] we need about 10 pes per primary electron to optimize resolution at $Q_{\beta\beta}$. The optical gain of NEXT-100 is near 2×10^3. The number of pes per electron for 35% coverage and 90% reflector is:

$$3 \times 10^3 \ (photons/electron) 0.3 \times 0.09 \times 0.5 \times 0.25 \sim 10.1 \ (pes/electron)$$

Thus, a coverage of 30% is sufficient for NEXT-100 purposes. This can be achieved by an energy plane with 60 PMTs.

5.1.3 PMT enclosures

The R11410-10 has been developed for use in cryogenic noble liquid detectors for dark matter searches and cannot resist high pressure. Therefore the PMTs will be housed in pressure-resistant enclosures.

These enclosures (a.k.a. *cans*) are shown in Figure 5.4. The concept is similar to that shown in the CDR. but they are no longer welded into the torispheric head as in the original design. Instead, both the pressure vessel and the PMT system are simplified by moving the enclosures fully inside the vessel. This allows the PMT system to be developed independently of the vessel. The cans are now mounted into a single carrier plate which itself is then attached to an inside flange of one head of the pressure vessel.

The enclosures are fabricated from grade 1 titanium pipe, having a sapphire window on one end, and a simple cap on the other end. The sapphire window and back cap are sealed to the enclosure using O-rings. The ends of the enclosure are threaded and a screw-down ring is used to apply the sealing force. Special spanner wrenches are used, and the threads on each ring are PTFE anodized to prevent galling. This has the advantage of maintaining a smaller profile and may allow use of Titanium pipe instead of bar stock. Leakage thorough O-rings (total for 60 cans) is calculated to be no more than 300 grams per year which will be recovered using a cold trap in the vacuum system, as described in chapter 8.

Furthermore, tests are underway to see if a Helicoflex metal gasket (C-ring) can seal against the sapphire without damage; if so, a lower leak rate will be advantageous. Grade 1 titanium shows acceptable radiopurity, which we estimate of the order of 300 μBq/kg, in both the uranium and thorium series. Required wall thickness for pressure is 2mm; the actual wall thickness is 5mm. The weight of each can is 1.5 kg, and therefore we

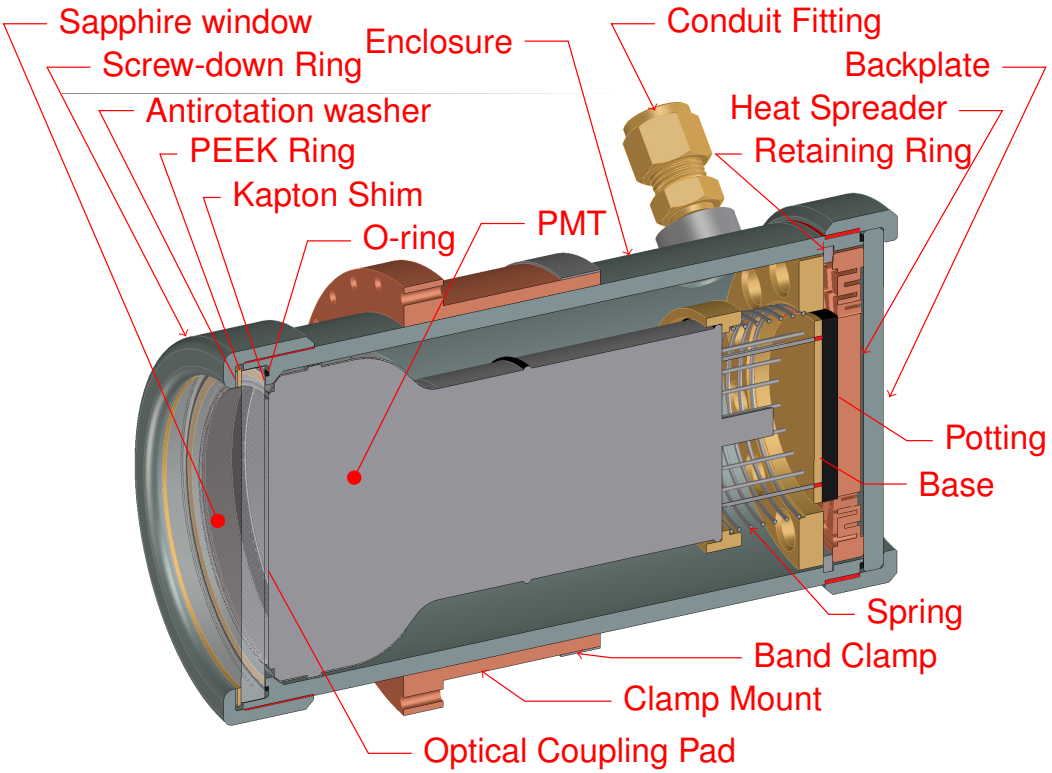

Figure 5.4: A PMT inside its enclosure.

expect them to contribute about 0.5 mBq per unit to the radioactive budget. This is to be compared with ∼3 mBq/unit emanating from the PMTs themselves. The titanium batch from which cans will be fabricated will be of the order of 100 kg and will be carefully screened to select the lowest possible background.

The windows are inserted from the front side and the PMT is inserted from the backside. This is required in order to use pipe, as there is an internal flange for the window to bear against, containing the O ring groove. This apparent disadvantage has an advantage: the window may be replaced without affecting the PMT and vice versa. The PMT is optically coupled to the window backside using silicone optical pads of 2-3mm thickness; use of grease is not advisable since any type of grit between the window and the PMT face can scratch the window where tensile stress from pressure is highest, leading to premature window failure (see window section below).

The PMT is held against the optical pad by a spring on the backside; this spring (with PEEK interface collars) bears against a circlip held in a groove machined into the ID of the enclosure. Thus the PMT can be installed independently from the base, and the base can be serviced or replaced without disturbing the optical coupling of the PMT to the window.

Cables from the PMT exit through a vacuum tight fitting into a copper tube that serves as both a cable conduit and a vacuum port for the interior. Conduit fittings screw into a welded-on boss in the side of the enclosure, this location allows the back cap to be removed for PMT and base access without disturbing the conduit fitting. these bosses are shown welded in at right angles to the enclosure axis.

5.1.4 Sapphire Windows

The sapphire windows will first be coated on one side with indium tin oxide to form a transparent (410nm and above) conductive coating. The conductivity is required to prevent electric field penetration into the PMT. Over this coating a layer of TPB is evaporated, which will shift any direct light (EL or S1) to a wavelength that has high transmission through the sapphire window and the optical coupling pad.

Sapphire is chosen over other possible radiopure materials such as Suprasil synthetic quartz, due to its much higher strength; this allows a reasonable window thickness of several mm which improves light acceptance. Finished window cost is lower than Suprasil for equivalent strength and finish. One can find typical strength numbers for sapphire in manufacturer's literature, however, sapphire, like other brittle materials, has an actual strength that is not only a function of the intrinsic material strength, but also a strong function of the flaw content present (unlike ductile materials, like metals, where intrinsic material strength is the primary determinant of actual strength). For windows stressed in bending, where maximum tensile stress is highest at the surface, surface flaws are more important than internal flaws, and the degree of polish has a strong effect on strength. Also large windows show a reduced strength compared to smaller equivalents since the chance of having a critical size flaw present goes up with increased (stressed) area. Crack growth is the failure mechanism, as no ductility is present which can act to blunt the crack tip. In ductile materials like metals, cracks primarily grow from cyclic

stresses, but in ceramics, crack growth is primarily caused by the phenomenon of stress corrosion cracking wherein the presence of moisture, in conjunction with high stresses at the crack tip act to dissociate the atomic bonds, and cyclic stresses do not seem to have a significant effect. The degree of polishing, and the size of the window, affect the resulting strength to a significant degree, as crack growth rates are a function of initial flaw sizes. Typically, the crack growth rate is slow until a critical size is reached (at the given stress level), then growth rate accelerates quickly to failure. This crack growth phenomenon is quantified using the methods of linear elastic fracture mechanics (LEFM).

Window reliability against breakage is assured by following a two step method:

First we use LEFM to determining a test-to-actual pressure ratio that will assure that any window which survives the test pressure for a short time, will not contain a flaw large enough to grow at a rate that will lead to failure at the operating pressure after a long time (10 years or more). We still need to determine an appropriate stress level for our window. This is done by using the methodology of Weibull distributions.

We use the Weibull distribution methodology [**?**], [**?**], giving the probability of failure as a function of applied stress and stressed area to determine a thickness whereby 95% of all windows purchased will not fail at the test pressure. We choose this initial survival probability as a balance between excessive test breakage and excessive window thickness. We do not have a strong requirement to minimize thickness for optical transmission, and window cost is dominated by polishing, not material cost. We gain further reliability by specifying a finer polish (20/10) than the typical (60/40) scratch/dig which was used as the basis of the published Weibull parameters. For more detail see the full document available in NEXT web page.

5.1.5 Overview of the energy plane

A brief overview of the energy plane (Figure 5.5) system is as follows:

- The energy plane is made of 60 low-background, high-QE PMTs, model R11410-10 from Hamamatsu.
- PMTs are sealed into individual pressure resistant, vacuum tight titanium enclosures (PMT enclosure or can).
- The PMT cans are all mounted to a common carrier plate that attaches to an internal flange of the pressure vessel head.
- Sapphire windows are secured with titanium screw-down rings and O-ring sealed to the front end of the enclosure. A similar system seals the back side of the enclosure
- PMT bases are potted with heat conducting epoxy to flexible copper heat spreaders which connect to the enclosures.
- PMT cables are enclosed in individual pressure resistant,vacuum tight tubing conduits.

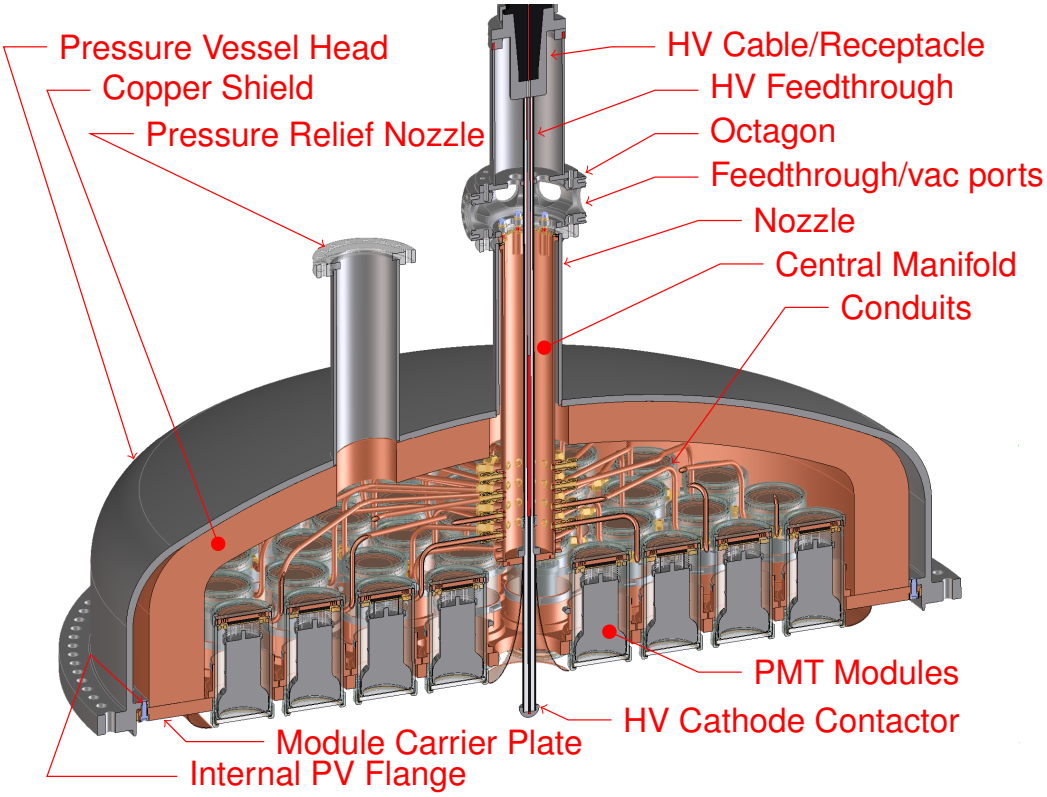

Figure 5.5: The full energy plane.

- Conduits all lead to a central manifold. The central manifold is cantilevered from the nozzle flange.
- PMT cables route through central manifold to 41 pin CF feedthroughs on a CF octagon, outside the lead shielding.
- High vacuum($< 10^{-6}$ torr) is applied at octagon port; good vacuum ($< 10^{-4}$ torr) is maintained inside enclosures through conduits, well below Paschen minimum, avoiding sparkover or glow discharge across PMT pins.
- A large vacuum tank buffer volume exists to limit pressure build in central manifold in case of sapphire window failure (avoids Super-K chain reaction failure mode). Xenon permeation through seals is recovered with a cold trap.
- Vacuum inside enclosure requires good thermal management, base cooling is by conduction into enclosure through a special low force heat spreader plate.
- PMT Modules are clamped into copper heat conduction flanges attached to the copper carrier plate.
- Heat is carried to pressure vessel flange by conduction through copper carrier plate; 7 C total temp rise.
- Carrier plate and central manifold can be electrically (but not thermally) isolated from the pressure vessel, to allow the PMTs to be operated with cathodes at full negative voltage, with anodes and signals at low voltage
- Alternately, the cathodes can be grounded, and the anodes and signal run at high positive voltage using only the central 21 pins of each 41 pin feedthrough, to avoid flashover.

This design requires a vacuum inside the enclosure, so as to detect the presence of any xenon leakage. Without vacuum the enclosure would eventually pressurize and destroy the PMT. The primary concern with vacuum is possible flashover across the PMT pins; this is avoided by maintaining enough conductance through each conduit (with cable inside) in conjunction with a high vacuum in the central manifold to keep enclosure pressure several orders of magnitude below the Paschen minimum (for Xe).

We considered the alternative of backfilling the enclosure with inert gas such as CO2 or N2, but this could be a source of contamination for xenon, and complicates both recovery of xenon, and PMT to PMT pressure isolation. We also considered the alternative of fully potting bases to PMTs but concluded this would reduce serviceability and possibly increase background radiation. We also considered the possibility of hermetically sealing each PMT and base into the enclosure, as this might be possible using niobium enclosures which can be diffusion bonded to sapphire. This option entails significant R&D to assure window seal integrity from pressure cycling. It also requires the development of a radiopure electrical feedthrough, possibly also using niobium and sapphire, since commercial feedthroughs with brazed alumina insulators typically show high background radioactivity.

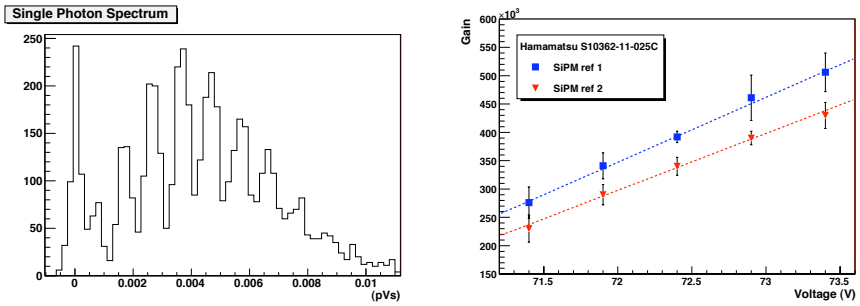

Figure 5.6: Left: Single Photon Spectrum of Si-PM. Right: Gain of two Si-PMs Hamamatsu S10362-11-025C measured as a function of the operative voltage.

5.2 The tracking plane

5.2.1 MPPCs

In NEXT the tracking function is provided by a plane of multi-pixel photon counters (MPPCs) operating as a light-pixels and located behind the transparent EL grids. The MPPCs will be manufactured by Hamamatsu and the chosen model is S10362-11-050P. This small device has an area of 1mm^2, 400 pixels per sensor and very large particle detection efficiency (PDE) in the blue region ($\sim$ 50%). It is very cost effective (less than 12.5 euros per unit for large orders) and its activity is expected to be low, given its composition (mainly silica).

A multi-pixel photon counter (MPPC), also called silicon photomultiplier (SiPM) is a photon-counting device consisting of an array of APD pixels operating in Geiger mode. Each APD of the MPPC array outputs a pulse signal when it detects one photon. The signal output from the Si-PM is the sum of all the APDs in the array.

The gain of a MPPC is very high, of the order of $10^5 - 10^6$. Figure 5.6 (left) shows the typical Single Photon Spectrum (SPS) response of these devices when are illuminated at low intensity with a 400 nm LED's. Figure 5.6 (right), shows the linear dependence of the gain of these devices with the bias voltage.

5.2.2 Dice Boards (DB)

The MPPCs will be mounted in Dice Boards (DB). This are square boards made of *cuflon* (PTFE fixed to a copper back plane). Figure 5.7 shows on of the DB of the NEXT-DEMO prototype, each one holding 4×4 pixels. NEXT-100 DB will be similar, but containing 8×8 pixels.

In NEXT-DEMO, the DB are fixed to a Mother Board (MB) (Figure 5.8). In NEXT-100, the DB will be fixed to a light honeycomb structure and connected directly to the FE electronics (Figure 5.9).

Each DB is supplied with a common bias voltage. A dedicated setup was prepared

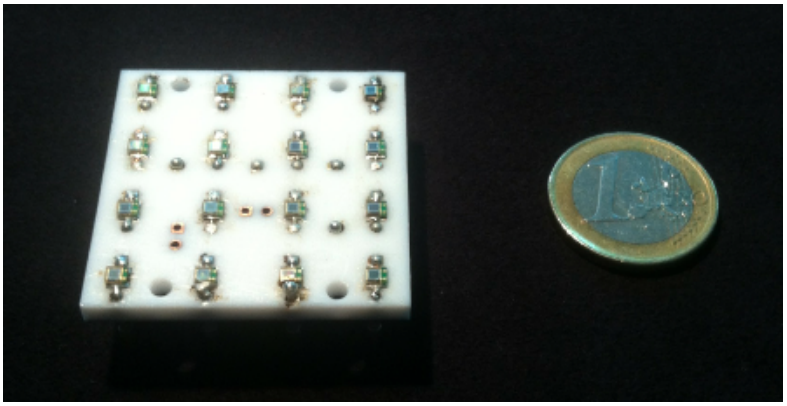

Figure 5.7: Dice Board containing 16 (4×4) MPPCs

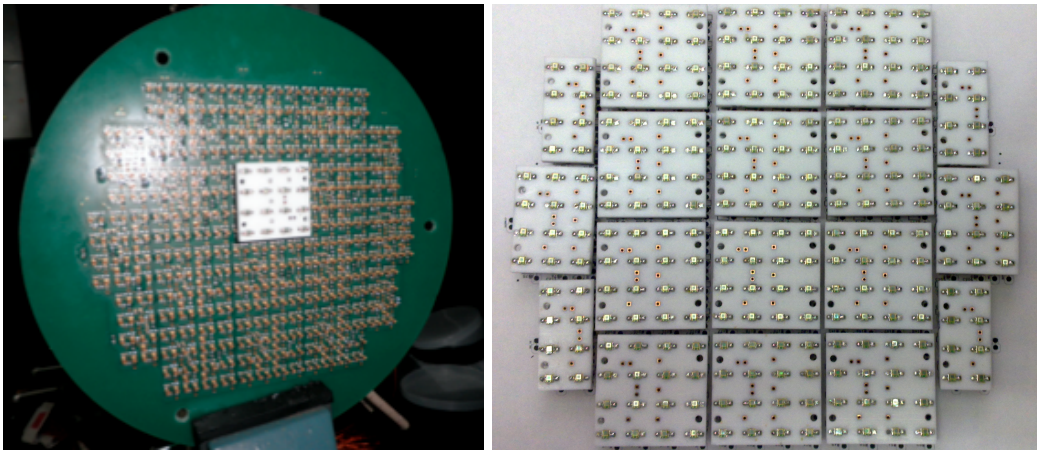

Figure 5.8: Left: Mother-Board with the front-end electronics on which center one of the Daughter-Boards is connected. Right: MPPCs DB arranged following the structure of NEXT-DEMO tracking plane.

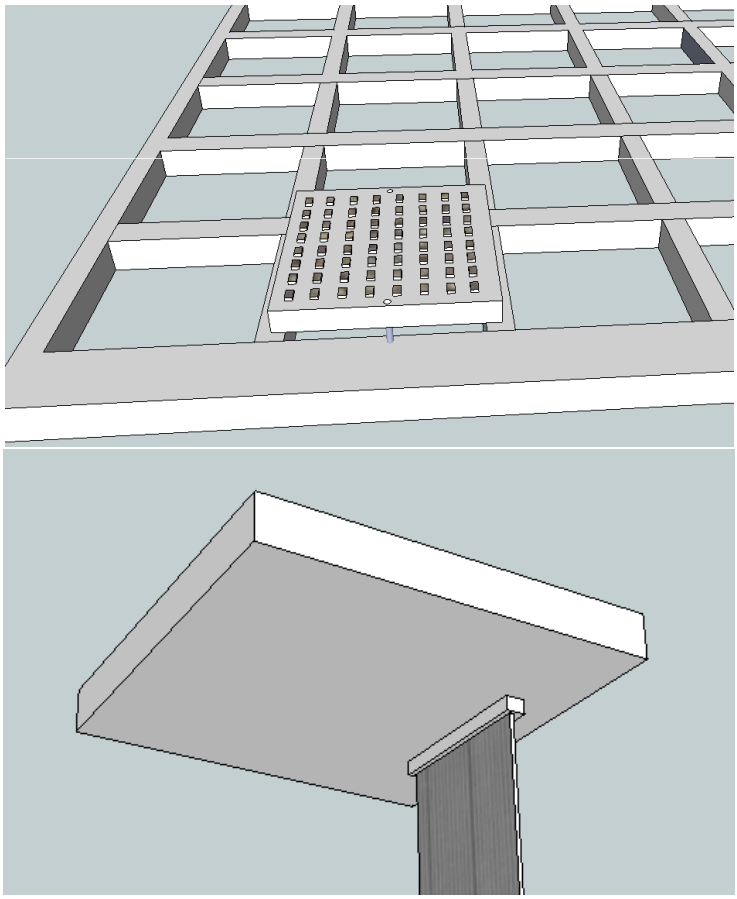

Figure 5.9: Left: In NEXT-100 DB will be fixed to a light honeycomb structure made of teflon. Right: DB will connect directly to the FE electronics.

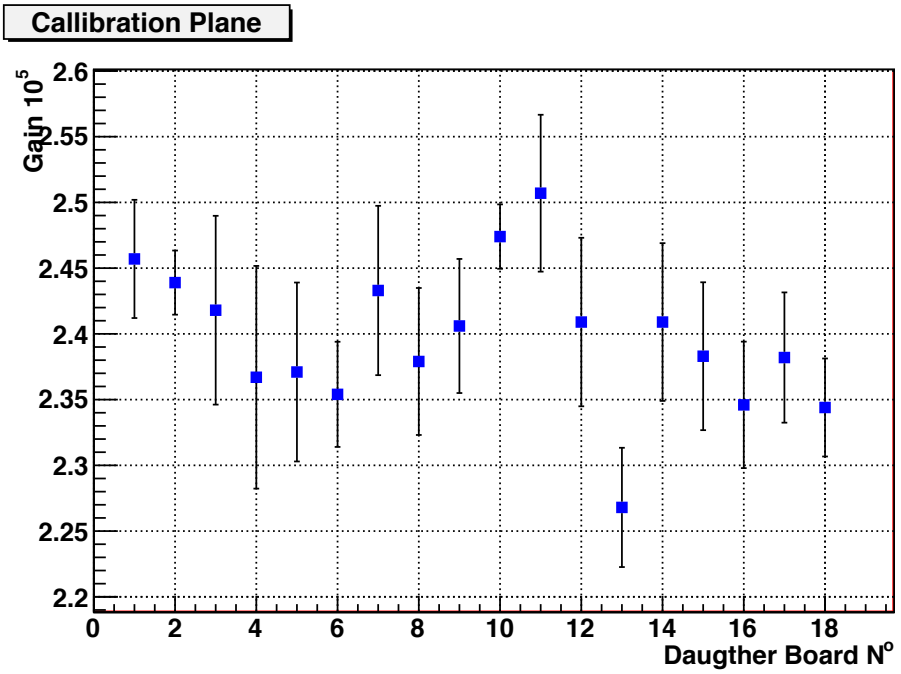

Figure 5.10: Values of Average and Spread in Gain of every Daughter Board.

to to measure the spread in gain of every single DB. As shown in Figure 5.10, spread in gain in every DB keep always below 4%, while the average in gain is (2.27 - 2.50) 10^5. These values provide a homogeneous response of the plane, and ensure the correct x-y resolution for the reconstruction of $\beta\beta$ events.

5.2.3 Dark Current

Figure **??** shows the typical dark current measured in our MPPCs as a function of the bias voltage and for three different temperatures. The level of the dark current is at about 5 photoelectrons. In NEXT-100 a digital threshold at the 4 - 6 p.e. level should lead to an insignificant noise rate. An automatic system to compensate temperature differences by adjusting the bias voltage has also been tested successfully and will be implemented in NEXT-100.

5.2.4 Pitch

The pitch of the NEXT-100 tracking planes is a compromise between several constrains imposed by the physics:

1. An electron moving in dense gas does not behave exactly as a minimum ionizing particle. Instead, it loses a significant part of its energy by the emission of discreet

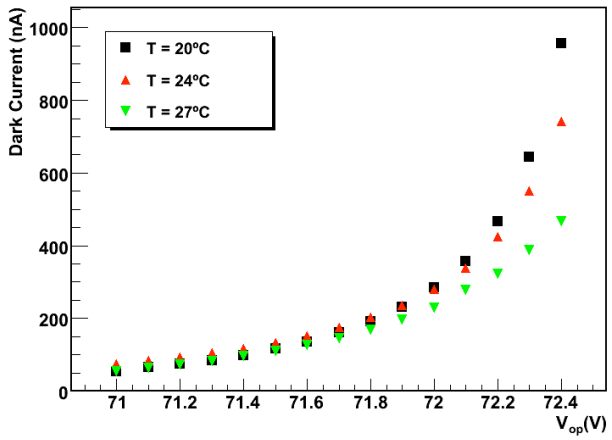

Figure 5.11: Dark current of one NEXT MPPC as a function of operative voltage and for three different temperatures T.

delta rays and bremsstrahlung radiation. The "photon cloud" associated to the electron has an rms distribution of the order of 1 cm.

2. Transverse diffusion in pure xenon is large, and the typical rms of the charge distribution for electrons produced in the center of the chamber is of the order of 1 cm.

3. Identifying low-energy photons (e.g, x-rays of 35 keV) nearby the electron track is an extra handle to label background events (e.g, photoelectric events in the ^{214}Bi peak). Photon-track separation is directly proportional to pitch.

A pitch significantly smaller than 1 cm is not useful due to charge dispersion and the photon cloud. Conversely, as the pitch increases the background rejection capability decreases. Monte Carlo studies show that a reasonable tradeoff may be found for pitches between 1 cm and 1.5,*cm*. While physics performance appears not to degrade too much with pitch in that region, the number of pixels decreases with the square of the pitch. A reasonable compromise appears to be 1.2 cm, which in turn requires about 7 000 pixels.

5.2.5 Tracking with MPPCs

Each primary electron entering the meshes produces EL light for a time interval given by the gap size divided by the drift velocity. For E/p $\sim$ 3.5 kV/cm bar, this time interval is about 3 μs. Typically, 600–1200 electrons contribute to the track imaging at any moment. Tracks less parallel to the TPC axis contribute the higher number of electrons within the EL gap. With so many primary electrons per mm, the statistical contribution to spatial resolution is $\sim$1 mm rms, even for the maximum possible diffusion within the chamber.

With an EL gain of around 3000 and a track population of ∼1000 electrons within the EL meshes, the total EL luminosity is in the range of 3×10^6 photons per μs (counting only the forward-going photons). A detection element of 1 mm^2 at a distance of 5 mm from the luminous region will subtend a solid angle fraction of ∼0.003. Hence, about 3,000 photons per μs will impinge on such a 1 mm^2 detection area.

Monte Carlo simulations indicate that about 1/3 of these photons will be transferred to the blue and to the MPPC active window by the TPB coating (see chapter 7). Thus, about 1 000 photons per microsecond, or 100 photons per 100 ns (the recovery time of a MPPC pixel) hit the MPPC. The S10362-11-025P model, used for NEXT-DEMO has a 1 600 cells and therefore a very small occupancy of 100/1600 = 0.06. The S10362-11-050P selected for NEXT-100 has 400 cells and still a very acceptable occupancy (for maximum energy deposition) of 0.25. In exchange the PDE of the S10362-11-050P is twice as large as that of the S10362-11-025P, and allows to detect low energy x-rays, up to energies of about 10 keV.

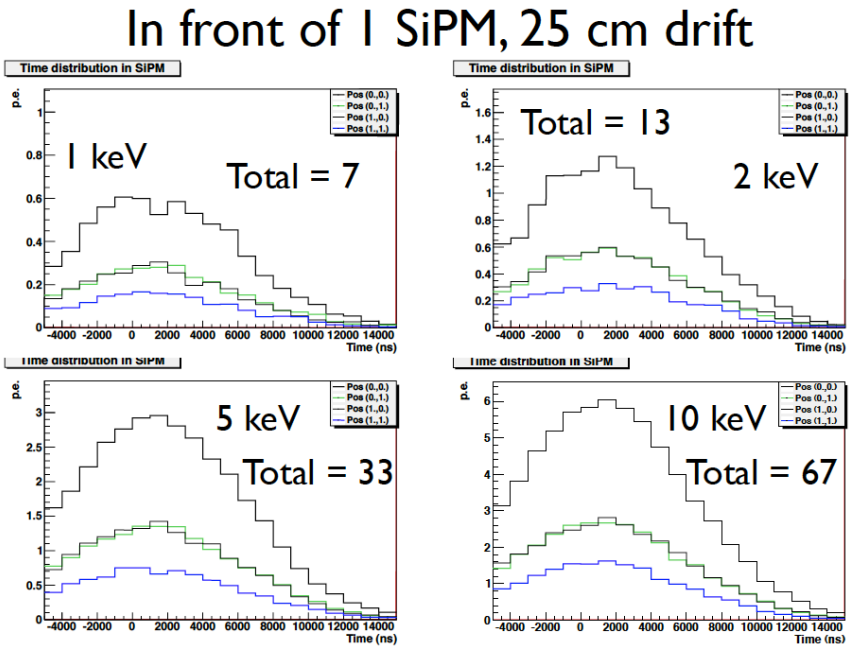

Figure 5.12: Light received in an array of 4 MPPCs (labeled (0,0), (0,1), (1,0) and (1,1)) when gammas of various energies produce light in an EL region of 5 mm at E/P of 4. In each case the signal is shown for the four MPPCs of the array as a function of time. A suitable cut to get rid of the dark current in a SiPM is 3–4 p.e., thus, with a count of 7 p.e, for the 1 keV case, the MPPCs are sensitive to small energy deposits.

In a more quantitative way, Figure 5.12 shows the Monte Carlo simulation of the light received in an array of 4 MPPCs (labeled (0,0), (0,1), (1,0) and (1,1)) when gammas of various energies produce light in an EL region of 5 mm at E/p of 4. In each case the signal is shown for the four MPPCs of the array as a function of time. A suitable cut to

get rid of the dark current in a MPPCs is 3–4 p.e., thus, with a count of 7 p.e, for the 1 keV case, the MPPCs are sensitive to small energy deposits.

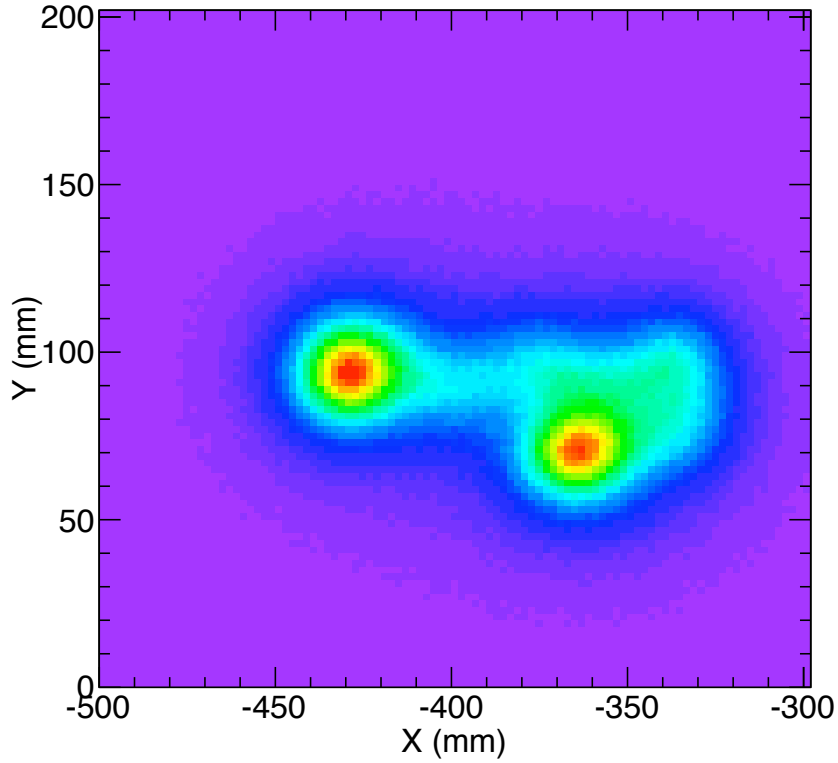

Figure 5.13: Monte Carlo simulation of the image of $\beta\beta0\nu$ event in a plane of SiPMs.

Figure 5.13 shows a Monte Carlo simulation of an event tracked by SiPMs. The light background collected by cells outside the track is at most 10^{-4} of the total track, and 10^{-5}–10^{-6} for most cells. Thus, good tracking is possible.

Chapter 6

Front end electronics and DAQ

6.1 FE readout electronics for the PMTs

The FE electronics for the PMTs in NEXT-100 will be very similar to the one developed for the NEXT-DEMO and NEXT-DBDM prototypes. The first step is to shape and filter the fast signals produced by the PMTs (less than 5 ns wide) to match the digitizer and eliminate the high frequency noise. An integrator is implemented by simply adding a capacitor and a resistor to the PMT base. The charge integration capacitor shunting the anode lengthens the pulse and reduces the primary signal peak voltage accordingly. The integrating signal is then fed to a low-pass filter amplifier.

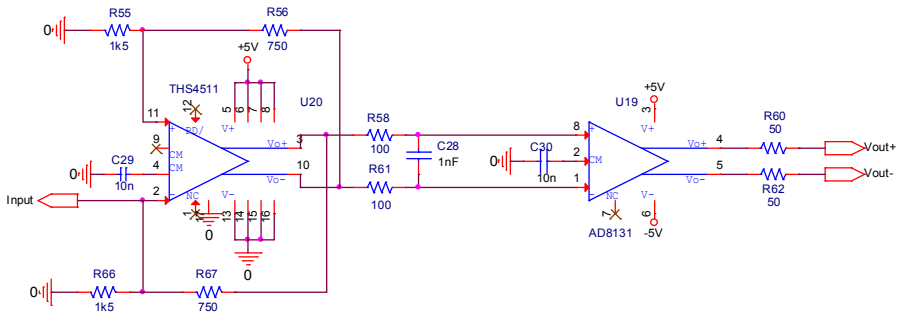

Figure 6.1: FE electronics schematics for one channel of the energy plane of NEXT-DEMO. A similar scheme will be implemented for NEXT-100.

6.2 FE readout electronics for the NEXT-DEMO

The front-end electronics for NEXT-DEMO is the baseline for NEXT-100. The design, shown in Figure 6.1 uses a single amplification stage based on the fully differential amplifier THS4511, which features low noise ($2\text{nV}/\sqrt{\text{Hz}}$) and provides enough gain to compensate for the attenuation in the following stage, based on a passive RC filter with

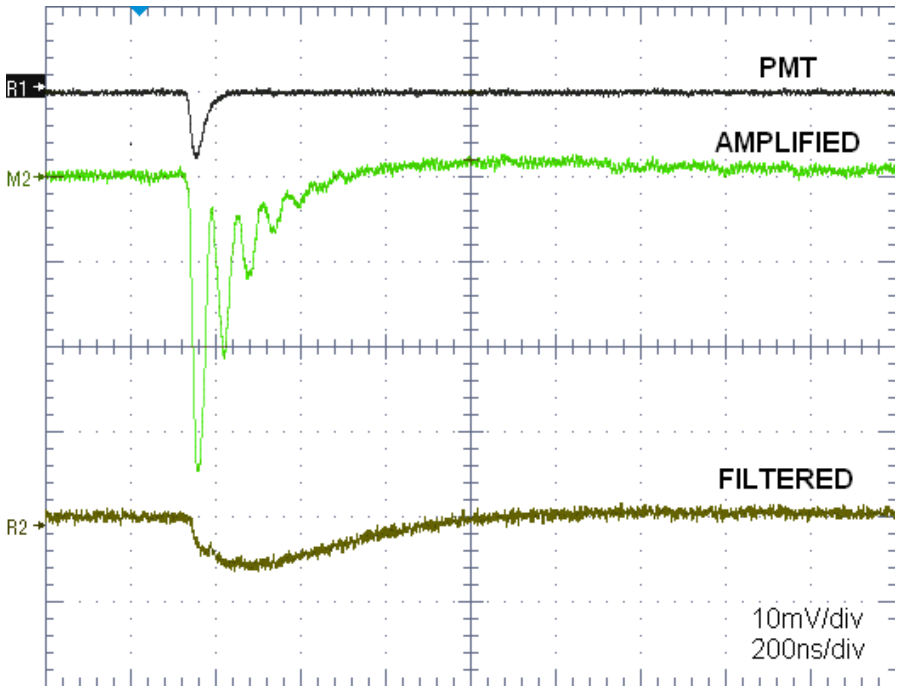

Figure 6.2: Single photo-electron signal directly from the PMT anode, amplified by the THS4511 and filtered with the passive RC filter.

a cut frequency of 800 kHz. This filtering produces enough signal stretching to allow taking many samples per single photo-electron at 40MHz, as illustrated in Figure 6.2.The AD8131 driver follows to provide enough current capabilities for the cable transmission of the signal to the ADC board. The gain for the current to voltage conversion is set by the feedback resistors. The input impedance of the front-end is given basically by the parallel resistors R66 and R67 in Figure 6.1. Usually R55 and R66 should have equal values to balance the differential amplifier, however the variation of R55 provides additional offset that may be useful to adjust the baseline level if necessary.

The energy resolution of the front-end circuit for a single photo-electron signal (with a typical charge of 1pC) using an oscilloscope is close to 5.9 %, with a SNR of 26 dB.

6.3 Digitization

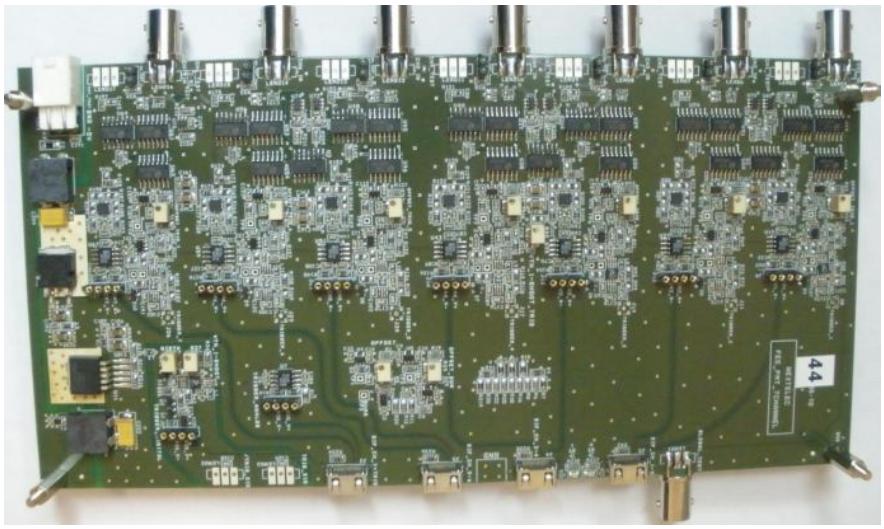

Figure 6.3: NEXT-DEMO front-end card with 7 analog channels.

The front-end circuit presented was implemented in 7 channel boards (Figure 6.3) and connected via HDMI cables to 12-bit 40-MHz digitizer cards. These digitizers are read out by FPGA-based DAQ modules that buffer, format and send event fragments to the DAQ PCs via gigabit Ethernet links.

Both the 16-channel digitizer card and the DAQ module (Front-End Concentrator, FEC) have been designed as a joint effort between CERN and the NEXT collaboration in the framework of the Scalable Readout System (SRS) for the RD51 R&D program, as describe in our CDR. These two cards are edge mounted to form a standard 6U×220 mm eurocard. The FEC module can interface different kinds of front-end electronics by using the appropriate plug-in card.

An additional FEC module with a different plug-in card is used as trigger module.

Besides forwarding a common clock and commands to all the DAQ modules, it receives trigger candidates from the DAQ modules, runs a trigger algorithm in the FPGA and distributes a trigger signal.

Up to two front-end cards can be read out by a single DAQ module through an ADC card. This readout system can be easily scaled up by simple addition of FEC cards.

6.4 Response of the FE electronics

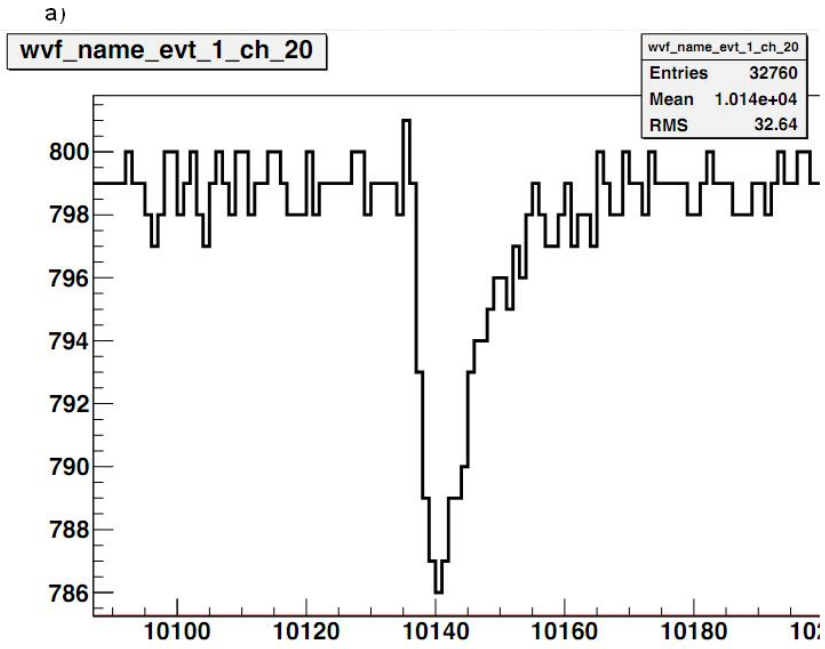

Figure 6.4: S1 signal in NEXT-DEMO. The signal is stretched over a few hundred nanoseconds, allowing confortable sampling.

As seen in Figure 6.4, with the NEXT-DEMO front-end electronics the scintillation pulse is sampled with 25-30 samples (some of them in the leading edge), achieving a high resolution digitization, and a high efficiency in the detection of the scintillation light. Noise levels of the baseline after digitalization is typically less than two counts. Measurements with test signals from a pulse generator reveal an energy resolution of 0.26 % for events with charge of 600 pC and 5 μs width.

To summarize, a low noise differential amplifier is used to obtain good resolution in the digitization of the primary scintillation, which provides high detection efficiency. The energy resolution of the front-end circuit using test input signals with charge values close to the ones expected from EL signals is of the order of 0.26%, which will provide precise energy measurement of the EL events in the TPC. The solution adopted for the DAQ system guarantees the scalability of the system for NEXT-100.

6.5 Design and performance of MPPC FE electronics for NEXT-DEMO

As described in chapter 4 the NEXT-DEMO tracking plane is an array of 248 SiPM sensors (Hamamatsu MPPC, 1mm^2 active area, SMD type model S10362-11-025P) uniformly spaced with a pitch of 1 cm.

A variable number of sensors (up to 16) are mounted on a daughter board and share bias voltage (provided by a high-voltage DC supply module from ISEG APS series) and ground reference. The gain dispersion in each daughter board is better than 4% while the average gain of each board is in 2.50×10^5 (chapter 5). This ensures a uniform plane response. A total of 18 daughter boards are mounted on top of a 238-mm diameter mother board for mechanical support and electrical connections. Figure 6.5, shows the chosen connection scheme for each SiPM sensor.

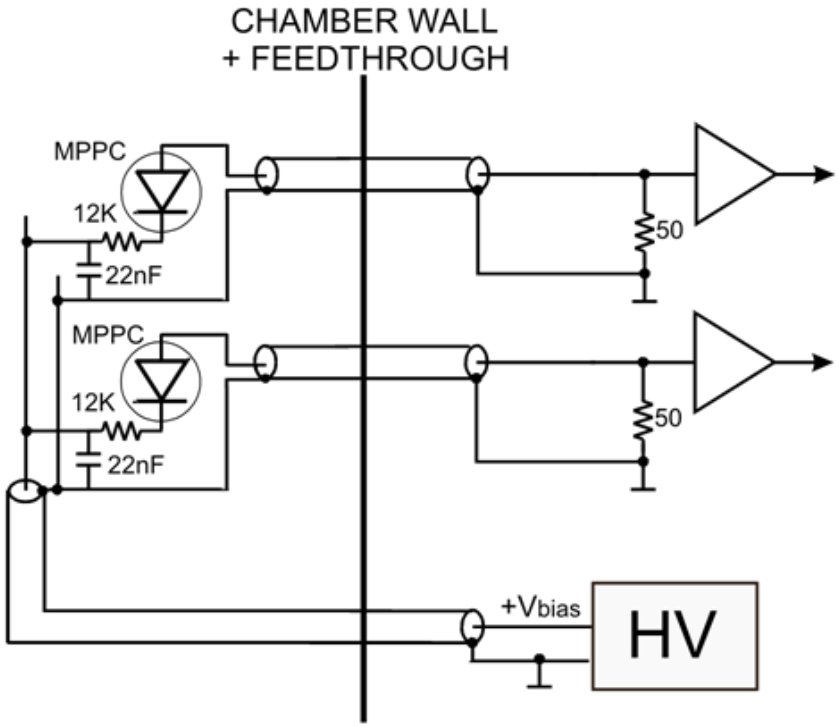

Figure 6.5: Connection scheme for a SiPM channel

From the mechanical point of view ribbon cables are easier to handle and connect than coaxial cables. As the crosstalk is additive, the induced crosstalk in a ribbon cable tends to be large due to the contribution of the neighboring wires. Several configurations of ribbon cables and signal mapping have been tested: twisted and untwisted wires, single

ended and differential, common ground and individual grounds. Single-ended, untwisted, common ground configuration showed the worst performance; with approx. -20 dB crosstalk. The best results were measured on a twisted-pair, differential transmission configuration. Yet even in this case the measured crosstalk was large. As a result it was decided to use coaxial cables to minimize this problem.

6.5.1 The analog front-end

The primary electron paths can be reconstructed from time-resolved measurements of the light that arrives to the SiPM sensor plane. Our approach is to estimate how many photons have reached each SiPM sensor per time bucket by integrating the SiPM output current in a gated integrator. The time bucket is 1us, giving 1 mm resolution in z as the drift velocity in pure xenon is about 1 mm/μs.

Although an integrating front-end is more vulnerable to thermal and induced noise, it also provides higher signal levels necessary to read very low light events. Most of the induced noise is due to capacitive/inductive coupling from switching digital lines in the PCB and charge sharing effects in the integrator. As a consequence, most of the integrated induced noise turns out to be deterministic which allows an easy calibration procedure. Signals obtained at the front-end output are converted to digital domain using a 12-bit 1-MHz ADC.

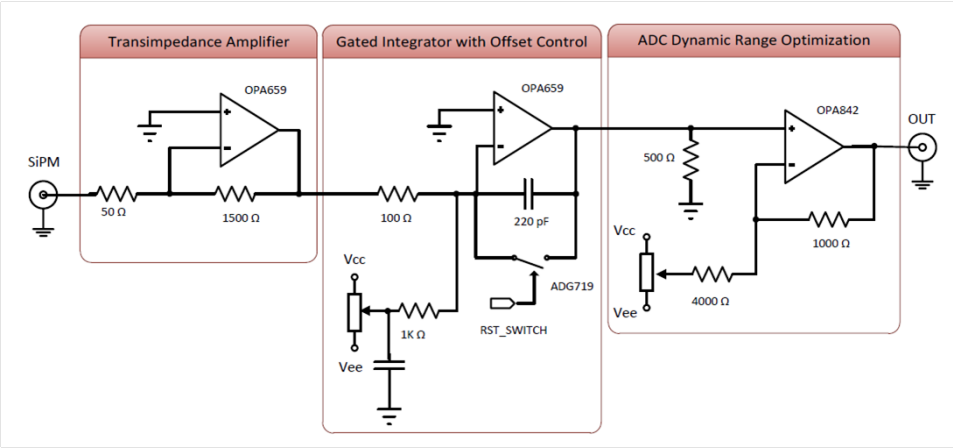

Figure 6.6: The amplifier and integrating circuit

The analog path consists of three different stages (Figure 6.6). The first stage is a transimpedance preamplifier with constant input impedance for line adaptation. Its bandwidth (45 MHz) is limited by input impedance (50 Ohm) and SiPM parasitic capacitance (70 pF). However OPA659 extended GBP (Gain-Bandwidth Product) provides a preamplifier intrinsic bandwidth over 70 MHz, which guarantees an efficient line adaptation over the final bandwidth. First stage gain (line impedance adaptation not included) is 1500 Ohm.

The second stage is a gated integrator with a variable integration time. The nominal value of this integration interval (1 μs) is related to the desired spatial resolution of the whole detector and the minimum will be limited by the maximum data rate of the uplink. Since we are using a positive bias voltage (Figure 6.5), first stage output is negative, which in turn produces a positive voltage at the integrator output. In order to discharge the integrating capacitor, ADG719 has been chosen since it is the fastest integrated switch available in a discrete implementation. It provides a discharge time of 10 ns which is only 1% of the nominal integration time. An offset correction is included since the integrator itself introduces an output offset: the switch control signal delivers a small quantity of charge into the feedback capacitor, producing a constant offset after every reset.

The third stage is a non-inverter amplifier with G = 2, required to produce a positive signal at the ADC input. It is designed to provide analog signal conditioning before AD conversion in order to fully exploit converter input dynamic range.

The gains in every stage have been defined to obtain 8 ADC counts between photoelectron peaks for a dynamic range of 250 pe. Although preamplifier noise response is quite good (OPA659 datasheet shows 8.9nV/sqrt(Hz)) it takes the largest part of the equivalent output noise (7 mV rms). The rest of the front-end shows lower noise levels. Finally the total equivalent output noise theoretically calculated and checked through simulation is below 10 mV rms. In order to provide a sufficient dynamic range and stay above the noise floor, gain values have been adjusted to obtain about 14 mV/pe.

6.5.2 The SiPM front-end board

We have designed and tested a 16-channel board that includes 16 analog paths and a digital section (Figure 6.7). The analog path circuit is described in the previous section.

The digital section is based on a small, low-power Xilinx Spartan-3 FPGA that reads sixteen 12-bit ADCs (AD7274), controls the switches in the gated integrators, builds a frame with the digitized data and communicates with the upstream readout stage using LVDS signals over standard RJ-45 connector and CAT6 cable. Careful PCB layout techniques ensure that the digital parts introduce very little noise in the analog section.

The FPGA has enough logic resources to implement some basic data processing, like zero suppression or a buffer to operate in triggered mode. Nevertheless, the readout is operated in raw continuous acquisition. A data packet containing the sixteen digitized values is sent to the DAQ each microsecond.

6.5.3 Interface to the DAQ

The upper stage in the readout chain is the Front-End Concentrator (FEC) card [**?**], designed as a joint collaboration between CERN and NEXT in the framework of the RD51 Collaboration readout system [**?**], [8]. Up to 16 front-end cards can be connected to the FEC, allowing for up to 256 SiPM channels, enough for NEXT-1. This readout system can be scaled up by simple addition of FEC cards. Data are sent to the DAQ PC via gigabit Ethernet links.

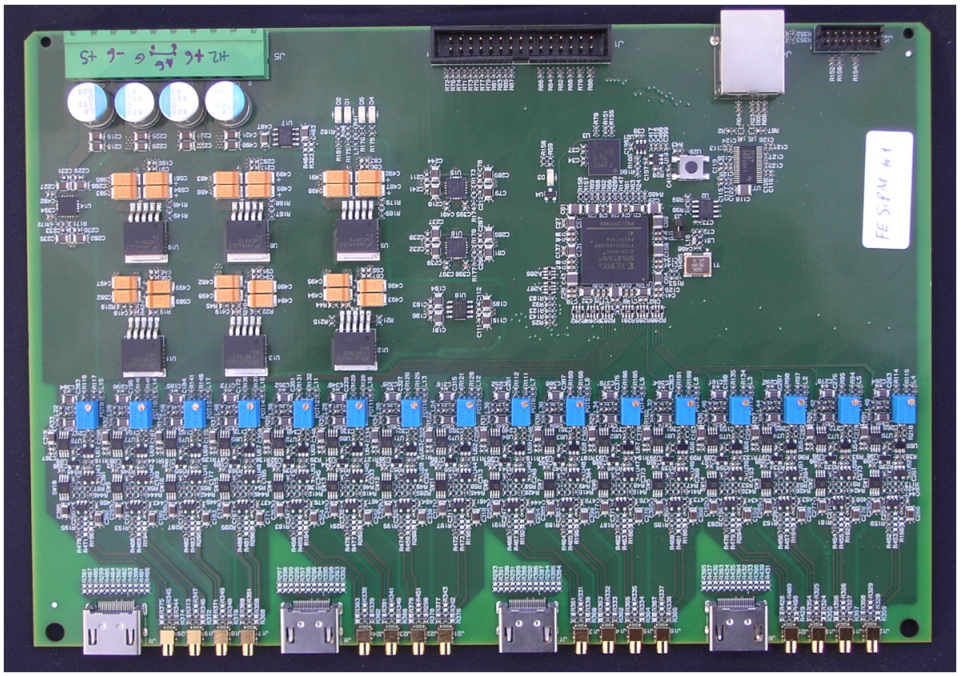

Figure 6.7: The FE-SiPM card. The digital section (top right) includes the FPGA and the RJ-45 142 socket. Voltage regulators are located at the top left corner. The bottom half of the board contains the 16 analog paths and the input connectors. Input signal options are miniature coax (single ended) or HDMI (differential)

The SiPM front-end board and the FEC card are connected by means of a high-speed full duplex link consisting of two LVDS pairs in each direction over a standard CAT-6 network cable. The FEC card sends a master clock to the front-end board FPGA over one of the LVDS pairs, thus providing system-level synchronization among the different front-end boards. A second downstream pair is used to send trigger and configuration commands to the front-end board.

The front-end FPGA sends the acquired data from the sixteen SiPM channels through the remaining two LVDS pairs (eight SiPM channels per pair). The bit rate of each serial link is 200 Mbps. Each data frame is composed of a 16-bit start of frame (SOF) header, a 16-bit identifier word, eight 16-bit words for the raw data and a 16-bit end of frame (EOF) trailer. The system sends a new frame each microsecond, resulting in an aggregated upstream data throughput of 352 Mb/s. A data recovery algorithm is used in the destination (FEC card) in order to avoid clock forwarding from the front -end [**?**].

The described link was validated in a test setup composed of one front-end board, one FEC card and a 15-meter CAT-6 network cable. No error in the link occurred during three consecutive days at the nominal 352 Mb/s load with PRBS data. The estimated BER is then lower than 1e-13 with a 99.99% confidence level. This result confirms the goodness of the link implementation.

6.5.4 Measurements

Our test setup consists of one daughter board, which comprises 16 channels (16 SiPMs), mounted on top of the motherboard. The 16 SiPM devices have been selected to have a uniform response, and are biased from a single voltage (71,14 V). The sensors were introduced inside a black box in order to reduce external noise.

A 400-nm LED was used to illuminate the daughter board at low intensity inside the black box. A suitable pulse generator was required to synchronize the emission of light with the trigger signal for the readout electronics. In each acquisition (384 μs), 10 pulses of light of 1 μs each were produced. Light pulses produce a variable number of detected photoelectrons, which are processed by the electronic chain, giving a response in ADC counts. Figure 6.8 shows the typical response in ADC counts for a single channel. Bins below a threshold (related to the base line level) are set to zero.

From this analysis we can easily obtain the linearity of our system. In fact, as can be seen from Figure 6.9, the behavior of the system with the number of photoelectrons produced in the device is linear, where the fit slope gives the conversion factor between ADC counts and photoelectrons (4.4 counts/pe in a dynamic range of 230 pe).

A few problems were found during the prototype measurements and have been corrected and tested for the final production version:

1. Large integrating capacitor discharge that produced a large error. This problem was due to a non-neglible input offset voltage in the integrating amplifier, and has been corrected (and tested) to very low levels by changing component values and modifying the circuit topology.

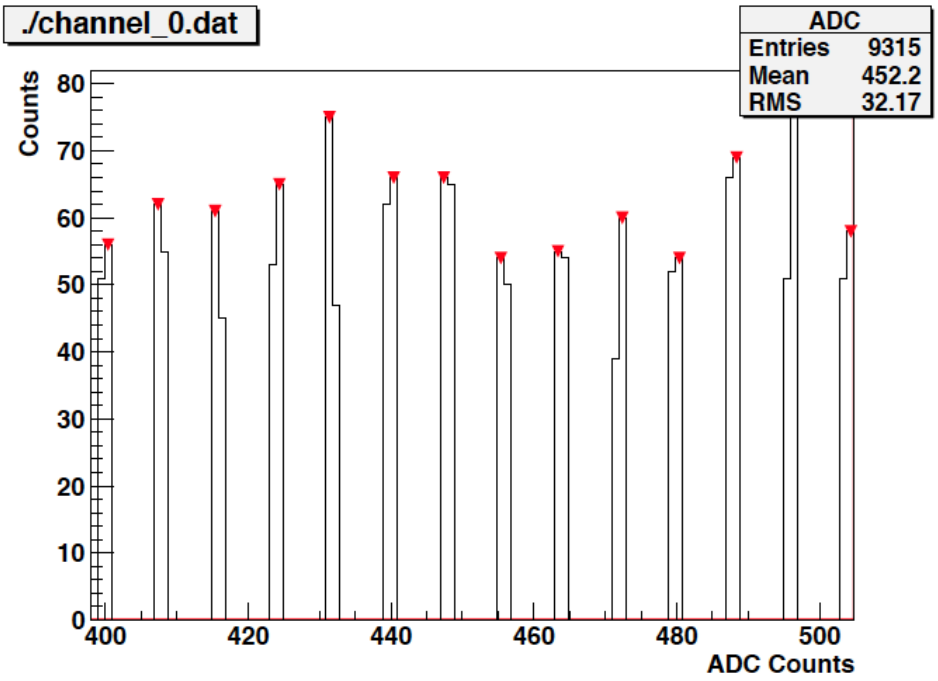

Figure 6.8: Histogram of the number of ADC counts produced by different photoelectrons in the final (production) circuit. Bins below a threshold (related to the base line level) are set to zero.

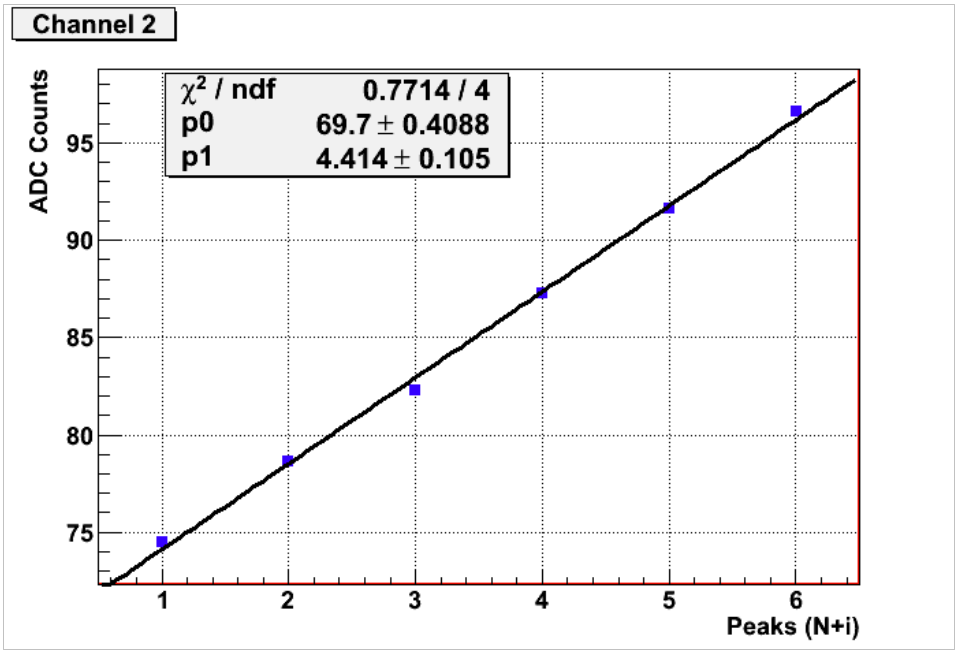

Figure 6.9: Linearity in the ADC dynamic range (1024 counts) for the final (production) circuit

2. Limited dynamic range due to a design error in the power supply for the last amplifying stage. This has been corrected in the final design.

3. A high number of channels had too much offset voltage (either positive or negative). This has been corrected (and tested) with an additional offset adjustment circuit at the output of the first amplifying stage.

6.5.5 Conclusions

In this section we have described the readout electronics for the SiPM plane in the NEXT-DEMO prototype. The readout is based on a gated integrator circuit that produces an output proportional to the number of photons that impinge on the SiPM sensor each microsecond. Data are then digitized and transmitted to the DAQ using RD51 electronics, developed jointly by the NEXT Collaboration and CERN for the RD51 Collaboration.

Performance tests with the first prototype show single photoelectron detection, good linearity and superb data transmission quality to the DAQ PC. A later increase in the dynamic range (as a result of new light simulations in the tracking plane) makes it impossible now to resolve the single photoelectron, which affects the calibration procedure for the SiPMs.

Scalability to 248 channels is straightforward, requiring sixteen front-end boards, two FEC cards (serving only 8 front-end cards each for a reduced load in the gigabit Ethernet link), two DAQ PCs and one trigger card to fan out clock and commands.

6.6 Towards a FE and readout solution for NEXT-100

While The FE electronics developed for NEXT-DEMO gives a base-line solution for NEXT-100, one should take into account the fact that the NEXT-100 tracking plane will have near 7 000 channels. Passing several thousand signal wires across feedthroughs is possible but challenging and probably not optimal. Consequently we are developing a new in-vessel FE electronics for that reduces the total number of feedthroughs to an acceptable level. In this section we present the new electronics readout architecture.

6.6.1 Initial considerations

The selected SiPM device for NEXT100 is the Hamamatsu MPPC, 1mm^2 active area, SMD type model S10362-11-050P. It has a higher gain than the device used in NEXT-DEMO, reducing the required gain in the front-end circuit. The driving requirements for the in-vessel electronics design are power, reliability, cost, radiopurity and outgassing.

Power

Very low power is a must as the heat is to be dissipated inside the vessel. The very front-end design and the ADCs are the key to low power, as the number of channels is 6.800

(assuming a 1.2 cm pitch). The weakest point in the NEXT-DEMO SiPM electronics is the high power consumption in the analog path that comprises three amplifier stages consuming each approx. 20 mA at +-5V, making a total of 600 mW per channel.

The solution that we are implementing for NEXT-100 implies to simplify the FE electronics. Our new design consists of a very simple front-end, very low power ADCs and a digital data merger stage (FPGA) to be placed inside the detector. This is achieved by replacing the gated integrator with a passive RC circuit and the power-hungry amplifiers with ultra low power devices. A preliminary estimation gives a total of 240 W for 6 800 channels. Additional power dissipation comes from drop in voltage regulators, FPGA (data handling and multiplexing) and transmission circuits required to reduce the number of feedthroughs in the TPC vessel. We estimate a total in-vessel electronics is 410 W.

To efficiently dissipate this heat we will attach the front-end cards to 10-cm-long copper fins radially mounted on the inner vessel surface. Since xenon is a bad heat conductor, most of the heat will be transferred from the fins to the vessel. A cooling circuit surrounding the detector would define an appropriate, constant vessel temperature. Simulations need to be carried out to validate how much power can be dissipated with this solution. Alternatively, liquid cooling inside the vessel could be used.

Reliability

Highest reliability is mandatory as servicing the front-end requires to open the vessel, an operation that must be avoided as much as possible. Reliable PCB manufacturing, including stress tests (like thermal cycling and vibration), PCB and component selection and careful design are required if we aim at highly reliable in-vessel electronics.

Besides this, manual channel-by-channel offset voltage adjustment turns out to be critical in the NEXT-100 electronics tests for a proper circuit operation and has to be avoided at an cost in NEXT-100. So, the effects offset voltage drift with temperature and aging needs to be considered in a design that cannot be easily accessed.

Cost

Low cost per channel is needed to reduce the electronics budget, as the number of channels is approx. 6,800. Thus, analog electronics and ADCs are the key elements in reducing overall cost. As an example, AD8005 amplifier is $1,64; AD8012 is $2,17 and AD7477A 10-bit ADC is $2,52 in 1k pieces. These are the main components in the currently evaluated circuit and make a subtotal of $6,33. Additional front-end components (linear regulators, resistors, capacitors) will increase the cost per channel to a maximum of $10 per channel, which is of the same order than the cost of the sensors themselves.

Radiopurity

Even if the in-vessel electronics will be separated from the active volume by a copper shield, careful component selection is required to reduce the background. Once the

passive component values are fixed, samples from several vendors can be tested to find out the cleanest ones. See chapter 2

6.7 Baseline design for the in-vessel front-end electronics amplifier

Taking the NEXT-DEMO electronics as a starting point, we have designed a three-stage circuit, with a gain of 10 in each stage. The first two stages are based on the AD8012 (two amplifiers per package, very low noise) and the last one on the AD8005 (ultra low power, 400 μA quiescent current). Total gain is (Rt is the input termination resistance) $1.000 \times Rt = 50.000$, as the first stage is a transimpedance amplifier with gain of $10 \times Rt = 500$. A passive, 2 μs time-constant RC circuit (200 pF, 10 kΩ between the second and the third stages acts as the circuit integrator.

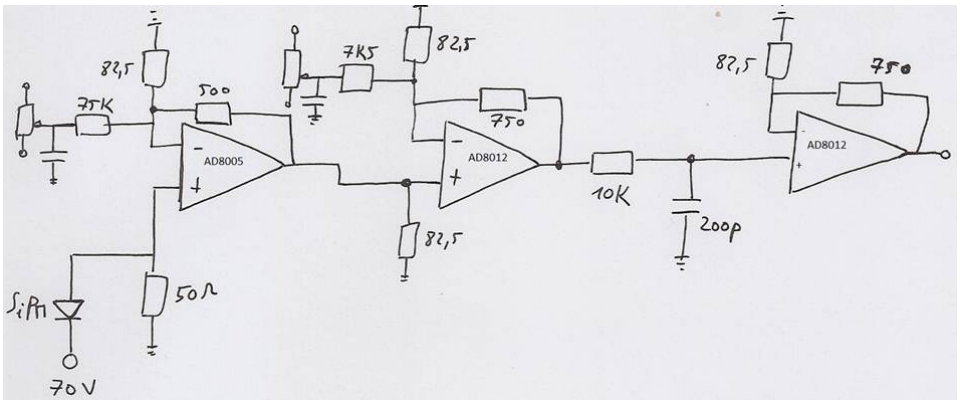

Figure 6.10: This low power amplifier circuit for NEXT100 features only approx. 30 mW power, 4mV/pe gain and 1.7mV rms noise

This gain will suffice to produce a 1V output for a 250-pe dynamic range.

6.7.1 Offset voltage adjustment

As it was previously mentioned, a solution has to be found that does not require adjustment by hand. Two options for automatic offset voltage adjustment, which can be complementary, are currently under evaluation:

- The 1V output for a 250 pe dynamic range leaves enough room in a typical 2.5-3 V input range ADC for offset voltage drift compensation either online (FPGA) or offline.
- Digital-to-analog converters (DAC) can be used for a coarse offset adjustement.

Total electronic noise in the amplifier circuit is very low according to the simulations: 1,7 mV rms. This is approx. 3 LSBs in a 12-bit ADC and sets the limit to the offset voltage adjustment.

6.7.2 Digitizing section

Two alternatives are currently under study:

- A single-channel 1-to-3 MHz low-power 12-bit ADCs (like AD7476), requiring only two lines (data and chip select) for readout. This solution is used in NEXT-DEMO. Total power dissipation (including amplifier and ADC) is approx. 35 mW per channel (a factor 18 less than the NEXT-DEMO solution). This value goes up to 60 mW after a conservative estimation for losses in voltage regulators and other auxiliary circuits (including FPGA readout and data transmission).

- A fast (40 MHz or higher) multi-channel ADC and an analog switch for multiplexing (Figure 6.11). This solution can lead to a reduced power consumption, though the effect of the noise induced by hundreds of switches inside the vessel has to be studied.

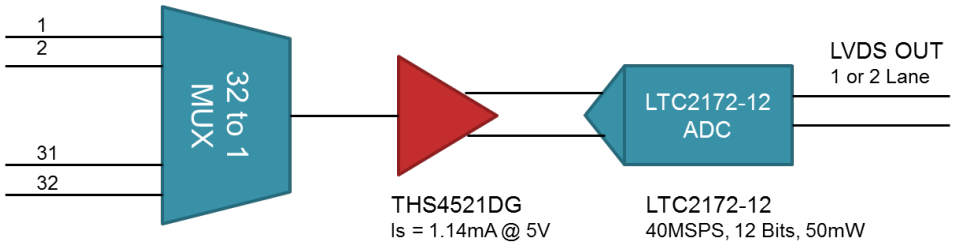

Figure 6.11: The multi-channel ADC option requires a large analog switch, a buffer and an ADC

6.7.3 Triggered vs. continuous (or push) readout

NEXT-DEMO SiPM electronics are read out in continuous (or push) mode. This means that there is no trigger at the front-end level. Every microsecond (the ADC sampling period), digitized and time-stamped data from all data channels above an adjustable threshold are simply sent to the DAQ module where data are stored in a circular buffer. No flow control is required. The DAQ modules are always available to receive data. Once a time-stamped trigger arrives to the DAQ module, the right data time interval is read from the circular buffer and sent to the DATE online system for event building. Flow control is needed at this level, but not at the front end.

This mode of operation simplifies the front-end hardware, as no buffers are needed at this level. Front-end FPGA firmware is also kept simple. We can afford using this mode as the reduced number of channels in the NEXT-DEMO SiPM plane (248) produces a moderate throughput. But this is not the case in NEXT-100, where data from the 6 800 SiPM channels must be sent across the TPC vessel. Minimizing the number of vacuum feedthroughs is a must, and this number is directly proportional to the aggregated throughput.

6.7.4 How can a triggered readout and zero suppression reduce the throughput?

We must first consider four design parameters for NEXT100:

1. There are 6 800 SiPMs in the tracking plane.
2. Drift length in the TPC is 1,3 m. This makes approx. 1,3 ms events for 1mm/μs electron drift speed.
3. Trigger will be based on S2 rather than on S1, as S1 may not work for low energy events (like WIMPs). So, large pre-trigger data (¿= 1.4 ms) must be acquired, as well as a post-trigger length (¿ 0.5 ms), making an estimated total of 2 ms data per event. As a result, each SiPM channel produces 2 ms/event * 12 bit/us = 24 000 bits or 3 000 Byte/event raw data.
4. In average, a SiPM is continuously illuminated for 10 μs in an event (thus 0,5% occupancy). This value can go up to something like 250 mus in some events (12,5% occupancy). Thus, 20% occupancy is a conservative estimate and to use it in our calculations.
5. Digitized SiPM data is required to be 12 bit resolution (although 14 bits is not at all discarded).
6. The target trigger rate is in the order of 10 Hz.

From these design parameters we can conclude that:

For 10 Hz trigger rate, 2 ms event size and 1 MHz sampling frequency, a triggered readout produces 50 times less throughput than a continuous readout. The benefits of the triggered readout are thus demonstrated. Of course a penalty must be paid: trigger must be fanned out inside the TPC and event buffers are required.

Taking into account channel occupancy, zero-suppression is really worth it, providing an additional reduction in a factor larger than 5 in the average throughput. Raw data mode must also be supported, of course.

6 800 channels produce approx. 20 MByte/event in raw data mode ($6.800 \times 3.000 \text{byte}/1024^2$). At 10 Hz rate this makes 200 MByte/s data, or 1,6 Gb/s throughput.

These three conclusions suggest a readout architecture sketched in the following section.

6.8 Readout architecture

6.8.1 FEB level (Front-End Board)

Consider a NEXT-100 DB with an 8×8 SiPM array. These DB cards equip the bias network and a few (maybe 4) connectors for low-cosstalk kapton ribbon cables. These

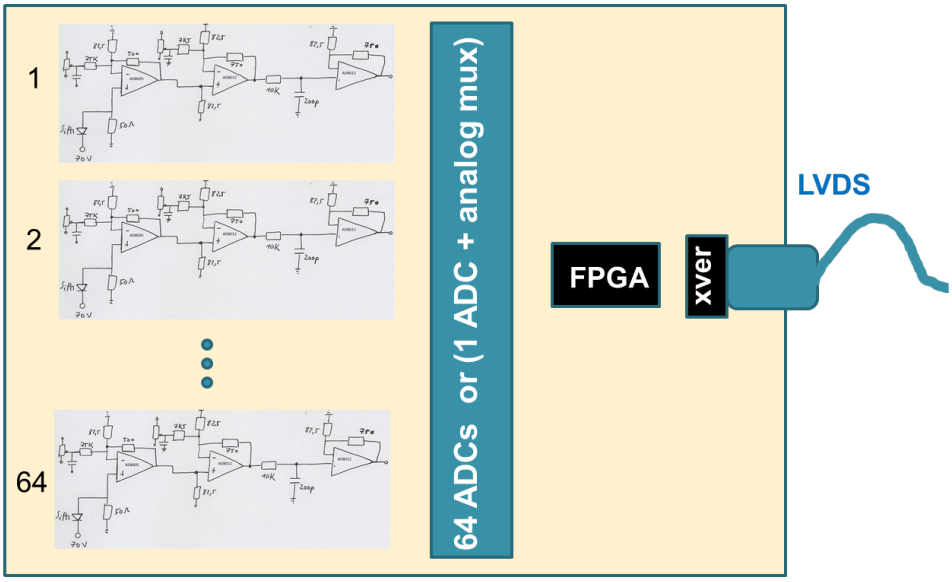

Figure 6.12: Functional blocks in the FEB card

cables arrive in a Front-End Board (FEB) that includes the analog stages, ADC converters, voltage regulators and an FPGA that handles, formats, buffers and transmits data to the outer DAQ. LVDS clock and trigger inputs are needed.

This 64-ch FEB is the key component in the in-vessel electronics. A total of 107 (6 800/64) FEBs are required. FEB size can be 15×15 cm, leaving 3.5 cm^2 board area per channel. This can easily accommodate the three amplifying stages and ADC per channel plus associated SMD passive components in one board side. The FPGA, voltage regulators and I/O connectors can sit in the opposite layer.

Power dissipation (as calculated in previous sections) is 60 mW per channel, or 3.84W/FEB (64 channels). The FEB plane will dissipate approx. $107 \times 384\text{W} = 410$ W.

6.8.2 Estimating buffer size for a zero dead time operation

One full event (2 000 samples) requires $2.000 \times 64 \times 12$ bit, slightly more than 1,5 Mbit (or 187,5 KByte). This is a first estimation for the size of the data buffer. It is available as true dual-ported memory in low-power FPGAs like Spartan-6 LX45 in 324-BGA (15×15mm) or in the low power, low cost, Xilinx Artix XC7A30T. Therefore no external memory is required.

Data are stored in a circular (ring) buffer in the FEB. Storing 1,5 Mbit data in 2 ms requires writing the buffer at 750 Mb/s. After framing, reading out at 200 Mb/s (maybe a limit for copper links across a vacuum feedthrough) takes 7,5 ms. So, from the 100 ms period (1/10Hz) the system spends in worst case 2 ms filling the buffer and 7.5 ms emptying it.

For zero-dead-time operation the buffer must be large enough to be continuously

filled, and so a 2+7,5= aprox. 10 ms buffer is needed. This means 1,5Mbit×10ms/2ms = 7,5 Mbit. This is still feasible with Xilinx Artix FPGAs (XC7A200T), that has an internal 13,5 Mbit memory. A trade-off between readout speed and buffer size must be found in order to minimize cost and power. Data links must a have a low speed for the sake of reduced power consumption, cheaper electronics, reduced FEB noise and enhanced signal integrity.

6.8.3 Data formatting and throughput at the FEB output

The FEB output frame format can be an evolution for the existing NEXT1 SiPM format. We propose to use a 16-bit word format. An event will be split into a number of frames containing each: SOF (start of frame), Board ID (unique FEB ID number), a number of data blocks, a CRC word and an EOF (End of Frame) word. Each data block contains a Timestamp word (including error flags) and 64 data words.

With a tentative number of data blocks per frame of 10, this makes 644 words per frame, or 10 304 bits. An event containing a maximum of 200 frames has a size of slightly less than 2 Mb.

In order to transfer these data in 10 ms (requiring 12 ms buffer in the FPGA), we need a link speed of 200 Mb/s. This is again a compromise between buffer size and link speed, and the sweep spot must be found.

If zero-dead-time operation is not required, operating at a 10 Hz rate, the required link throughput would be just 20 Mb/s.

Careful evaluation of copper and optical link solutions will provide the right compromise between buffer size, power dissipation, reliability and cost.

6.9 DAQ requirements for the tracking plane readout

The number of FEC cards and LDC PCs is determined by two numbers:

1. The tracking plane produces 1.6 Gb/s data. Setting a comfortable working point for the gigabit Ethernet links between the FECs and the LDCs in 400 Mb/s, 4 LDCs are required.

2. Assuming 200 Mb/s link speed (LVDS over copper) from the in-vessel electronics to the DAQ (the same speed and technology used in NEXT1 for the SiPM plane readout) the existing 16-link LVDS adapter card can be used. The 107 links coming from the vessel require then 107/16=7 FEC cards.

Combining these two points, we can think of 7 FECs and 4 LDCs as the size of the tracking DAQ partition. This is approx. the size of the full NEXT1 DAQ. The conclusion is that we are in very safe ground for the NEXT100 SiPM plane DAQ.

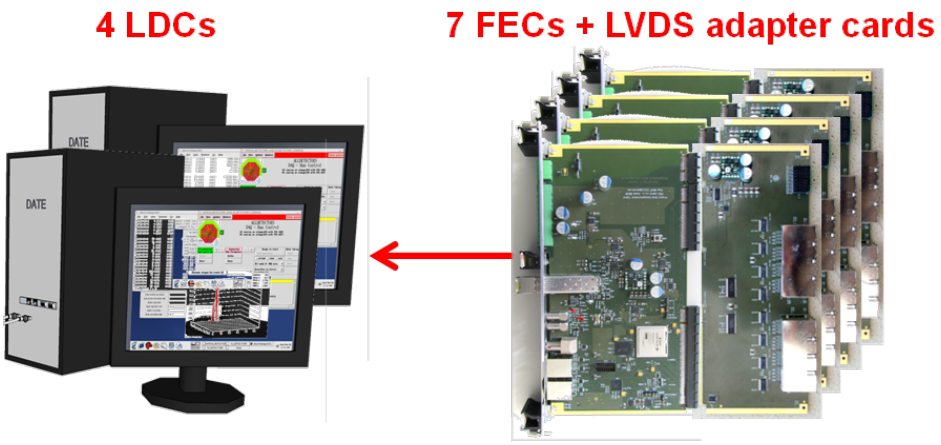

Figure 6.13: The NEXT-100 SiPM plane can be read out with 4 LDCs and 7 FECs

Chapter 7

TPB coating

7.1 Shifting the VUV light for NEXT

Xenon scintillates in the VUV range, with a peak at ∼175 nm. Although the NEXT PMTs have the same QE for light in this range and in the blue (about 25%), the MPPCs have a very low PDE below 200 nm. Therefore, it is imperative to use a wavelength shifter (WLS) on MPPCs. Furthermore, the reflectivity of the light tube (made of TTX, a Teflon cloth) is dramatically improved by coating the TTX with TPB. Last, but not least, our PMTs will be enclosed in cans coupled to the gas through sapphire windows. UV grade sapphire is extremely expensive, and thus coating the sapphire windows of the PMT enclosures with PMT appears also as mandatory.

Tetraphenyl-butadiene (TPB) of $\geq 99\%$ purity grade is an organic WLS widely used in many experiments to shift scintillation light produced in the UV by Liquid Argon or Liquid Xenon to the visible. It absorbs light in a wide UV range and re-emits it in the blue with an emission peak around 430 nm. TPB can be applied by vacuum evaporation from crystalline form directly onto surfaces. The TPB coating obtained that way is reported to be hard and durable with good adherence to the substrate and high resistance to mechanical abrasion. It is not soluble in water but may be degraded by humidity, and can be removed when necessary by the use of benzene or other organic solvents.

A TPB procedure to deposit a thin layer of TPC on flat (relatively small) surfaces, such as dice boards (DBs) and the sapphire windows of the PMT cans has been developed at ICMOL and IFIC. A second procedure to coat large surfaces, such as the NEXT-100 light tube has also been developed at IFIC.

7.2 TPB coating technique at ICMOL

The technique to deposit thin layers in flat surfaces —including glass, quartz, sapphire and teflon— has been developed at the coating facility of the Instituto de Ciencias de Materiales (ICMOL). Figure 7.1 shows the evaporator used. It is enclosed in a glove-chamber filled with with N_2 to insures the conservation of the organic compounds by

avoiding their oxidation and hydration. The coating setup consists in a vacuum chamber enclosing 4 ceramic crucibles used to contain and melt simultaneously up to 4 compounds. During the TPB evaporation campaign for NEXT the whole setup was cleaned to remove any traces of other molecules. One crucible only was used and filled with TPB pounder. It was heated by a cartridge with an adjustable current for monitoring the temperature and controlling the evaporation rate to avoid bubbling and sputtering of the TPB onto the exposed substrate.

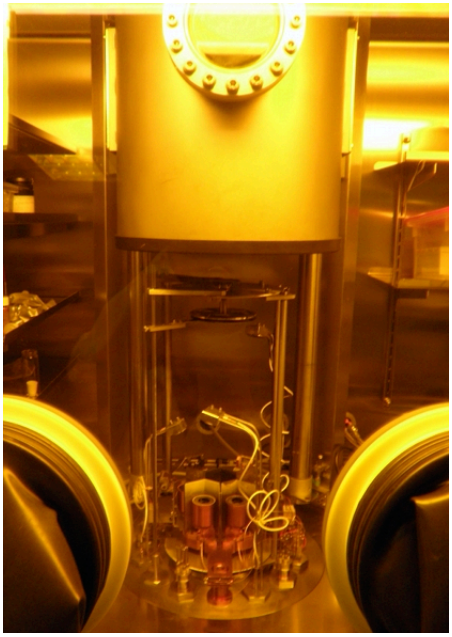

Figure 7.1: The Evaporator where one can distinguish from bottom to top, the crucibles and the deposition-sensors, the shutter, the sample-holder supported by a spinning disk and the vacuum chamber which is closed down during evacuation and coating.

The surface to be coated is positioned on a sample-holder located 15 cm above the crucible. This holder is fixed on a spinning disk which allows the rotation, at a constant velocity, of the samples during evaporation. Below the sample-holder a shutter allows to mask the exposed surfaces when stopping the TPB deposition is required. The TPB deposition thickness is recorded by a deposition sensor, located half-way between the crucible and the surface to be coated.

Prior to their introduction in the Evaporator, the samples are cleaned with alcohol at 150^oC and dried with pressurized N_2. After positioning of the clean samples in the Evaporator, the vacuum-chamber is closed and evacuation is started using a diaphragm and a turbomolecular pump. After the optimal vacuum-level is reached, typically 4×10^{-7} mbar, heating of the crucible is started while the shutter is maintained closed. The relevant parameters, such as the vacuum level, the temperature in the crucible, the deposition rate and the deposition thickness can be monitored during the evaporation

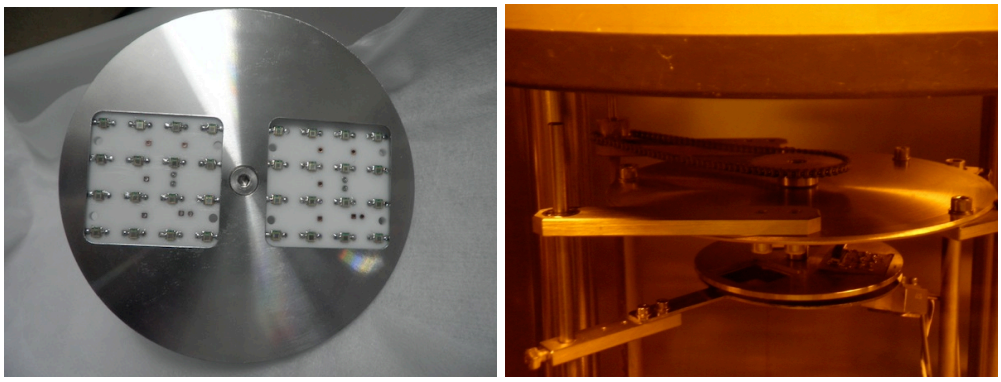

Figure 7.2: (Left) Two 16-MPPC DB positioned in their lodging in the sample-holder of the evaporator. (Right) The sample-holder fixed to the spinning disk of the evaporator. The shutter underneath covers the exposed surface of the samples.

process.

The TPB melting temperature is 203^{o}C at atmospheric pressure. At the operation vacuum level, TPB starts evaporation at about 75^{o}C. This is the temperature at which the deposition-sensor starts to record an increasing deposition thickness. The shutter is then opened when the deposition rate stabilizes around a constant value, typically between 1.8 and 2.4 Å/s. This is an indication that a steady evaporation process of the TPB is established. At the same time, the spinning of the sample-holder is initiated to insure a uniform deposition of the TPB on the exposed surface. When the desired thickness is reached the shutter is closed to avoid additional deposition on the coated surface.

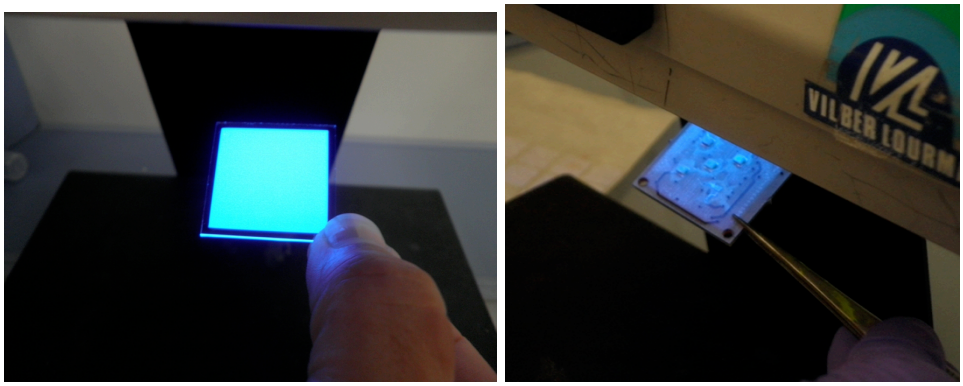

Figure 7.3: Illumination with 240 nm UV light of a glass-slice (left) and a 5-SiPM board (right) both coated with TPB.

Several successive depositions of a chosen thickness have been successfully produced on TiO_2 glass-slices and on several samples of MPPC dice boards. As an illustration, Figure 7.3 shows a glass-slice (left) and a prototype DB (right) coated with TPB and illu-

minated with UV light at 240 nm, clearly re-emitting in the blue. The coated glass-slices and DB samples have been tested and characterized at IFIC and ICMOL with different UV light sources. Some of the most relevant results are described in the following subsections (a detailed paper with more extensive details will be published shortly).

7.2.1 Transmittance of the TPB at its emission wavelength

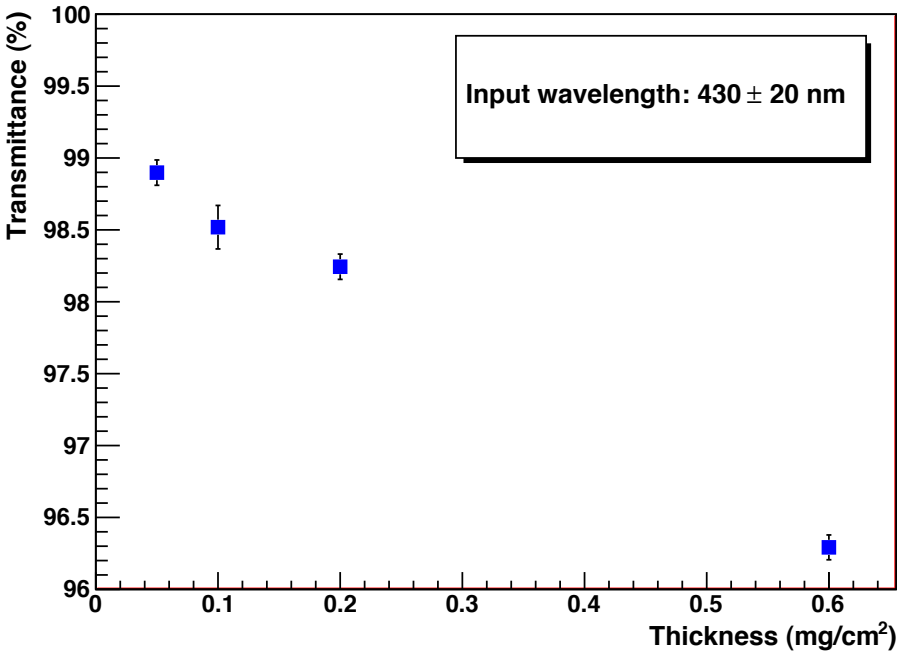

Figure 7.4: Transmittance of the TPB at its emission wavelength as a function of thickness.

The transmittance of the TPB at its emission wavelength has been measured as a function of the coating thickness using an LED emitting at 430±20 nm which illuminates successively four glass-slices of 3 cm × 3 cm coated with 0.05 mg/cm^2, 0.1 mg/cm^2, 0.2 mg/cm^2 and 0.6 mg/cm^2 of TPB. The non-coated side of the glass-slices was coupled to the window of a 1 inch PMT Hamamatsu R8520. The anode current of the PMT was measured for each TPB thickness and compared to the current measured with a non-coated glass-slice of the same size and thickness as the coated ones. The illumination conditions were kept unchanged for all the samples measured. The transmittance of the TPB coating shown in Figure 7.4 as a function of the thickness indicates a small increase of the absorption, which is however, always below 4%. A very important consequence of this result is that the thickness of the TPB layer is not, within reasonable bounds, a crucial parameter regarding light absorption. This is important for the coating of large

surfaces, such as the light tube sheets, since the large evaporator available at IFIC lab only allows an approximate control of such deposition thickness.

7.2.2 Response of coated MPPCs as a function of TPB thickness

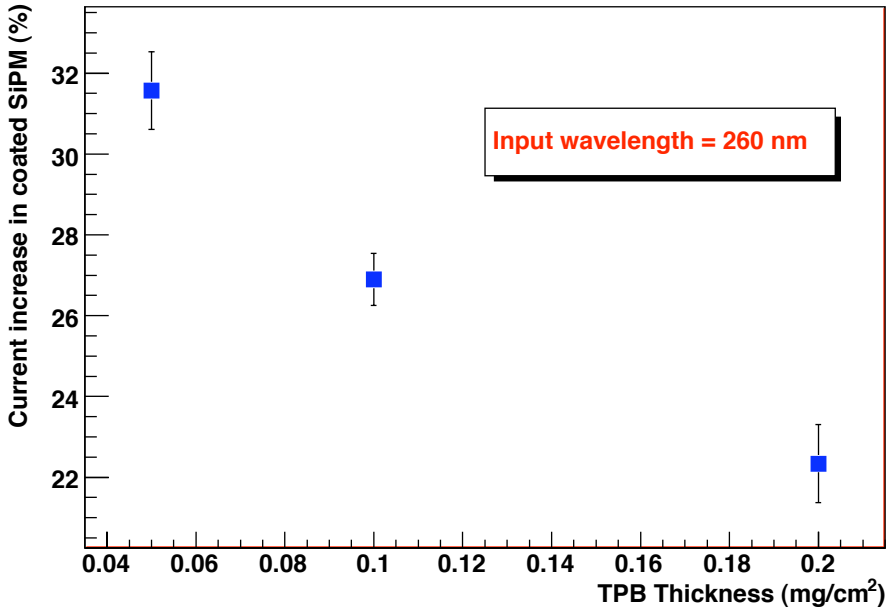

Figure 7.5: Response of the TPB coated SiPMs to UV light (260 nm) as a function of the coating thickness. For each thickness, the average of the currents measured in each of the 5 SiPMs of a board is represented.

An important parameter for the coating of the MPPCs is the coating thickness which allows the optimal conversion efficiency of the TPB. To establish it, depositions of various thickness of TPB were carried out on 5-MPPC boards which were then characterized using a collimated LED emitting at 260 nm. The current output from the coated MPPC was measured and compared to the current measured prior to coating with the same illumination and temperature conditions. In Figure 7.5 the increase of current of the MPPCs after coating when illuminated at 260 nm is shown as a function of the TPB thickness. This current increase similar to an increase of the photo-detection efficiency of the MPPCs depends on the coating thickness and is shown to have maximum value at 0.05 mg/cm^2. As a consequence, we find that the optimal deposition thickness in the DBs must be smaller than 0.1 mg/cm^2.

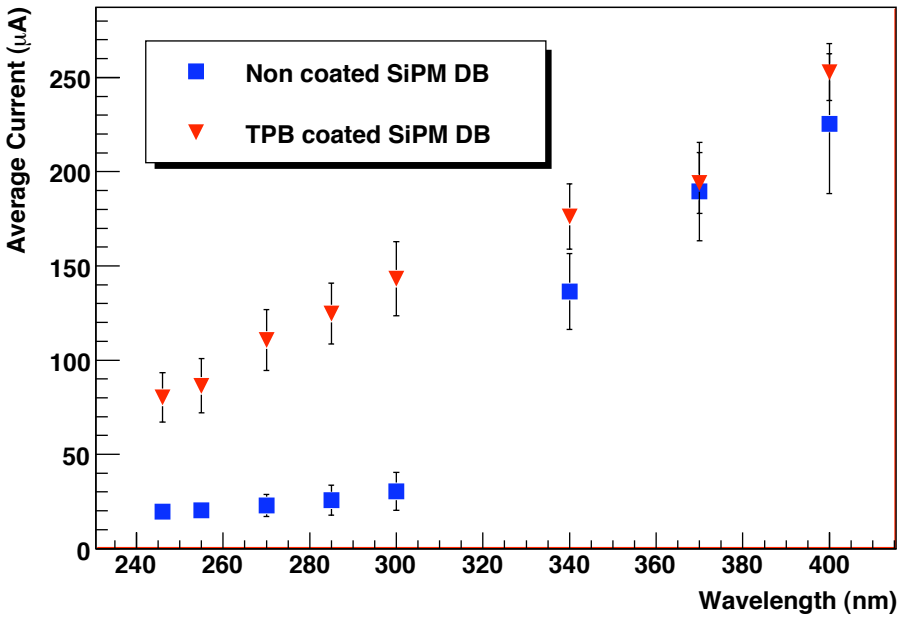

Figure 7.6: Average current in the TPB coated SiPMs DB compared to the average current of a non coated DB. Both DB are illuminated by the same Xenon Lamp coupled to a Monochromator to select the input wavelength.

7.2.3 Coating and testing of NEXT-DEMO DB

The 18 DB of NEXT-DEMO tracking plane were coated with 0.1 mg/cm^2 of TPB. The currents produced in the MPPCs measured before and after coating in the same illumination and temperature conditions are compared. The results are illustrated in Figure 7.6, where a significant increase of the current in the coated DBs is observed at input wavelengths below 340 nm.

7.2.4 Response after long-term storage

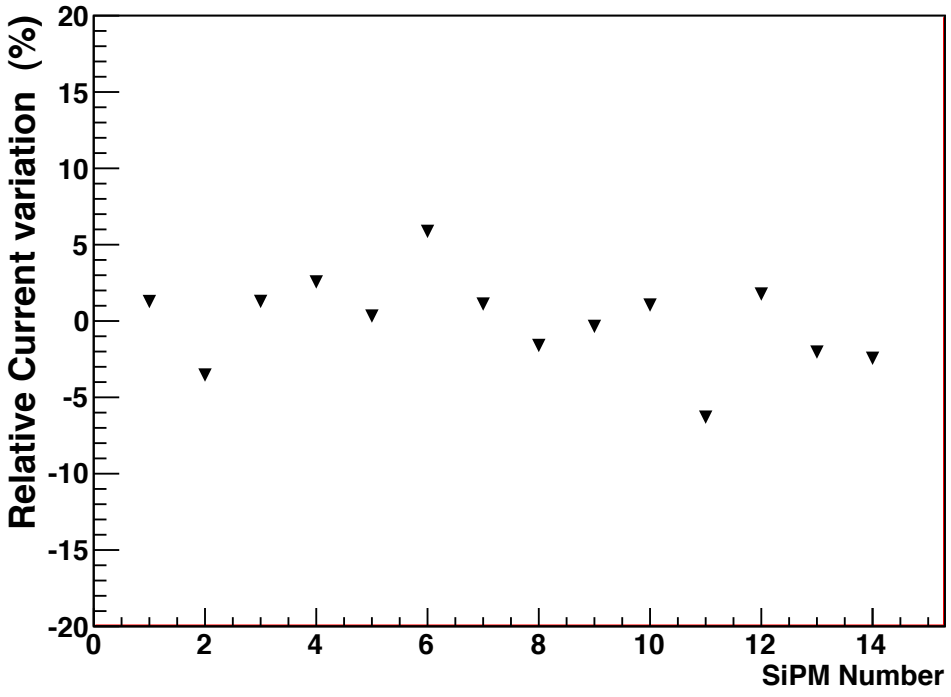

Figure 7.7: Relative current variation of 14 coated SiPMs, illuminated with a LED emitting at 240 nm, after 9 months storage in vacuum

The coated DB were stored in a vacuum chamber at pressure < 1 mbar. A sample of these DBs was re-tested after 9 months of storage using a LED emitting at 240 nm, and illuminating individually each of the 16 SiPMs of the coated DB. The current measured after storage was compared to that measured immediately after the coating process. The relative current variation of the 14 MPPCs tested is shown in figure 7.7. The average of all currents in the MPPCs has less than 1% relative variation, which is well within the experimental uncertainties. Indeed, considering the possible variation of LED intensity and ambient temperature after 9 months, the current variation of the coated MPPCs observed indicates no evidence of aging effects in the TPB coatings stored in a moderate

vacuum.

7.3 Coating of the NEXT-100 light tube

7.3.1 Light tube materials

The light tube will cover the inner part of the field cage. The presence of a strong electric field demands, therefore, non conductive material as the substrate for the wavelength shifter. We have chosen the same materials studied by the ArDm collaboartion [9, 10]. The light tube substrate will be ESR (Vikuiti^{T}M Enhanced Specular Reflector foil) from the company 3M^{T}M and Tetratex (TTX)from the company Donaldson Membranes. The ESR foil is a multilayer specular reflecting polymer measured to be highly radiopure [10]. Its appearance is that of a polished metal although the material is non conducting. It has a specular reflection coefficient of practically 100% in a large region of the optical spectrum. TTX is an aligned polytetrafluoroethylene (PTFE) fibrous cloth and is nearly a 100% diffuse Lambertian reflector. It is also radiopure (typically less than 1 ppb, which, given the very low mass involved, gives a negligible contribution to the radioactive budget) and has low degassing. The measured reflectivity of the ESR + TTX foils is about 97% at 430 nm.

7.3.2 The large evaporation chamber

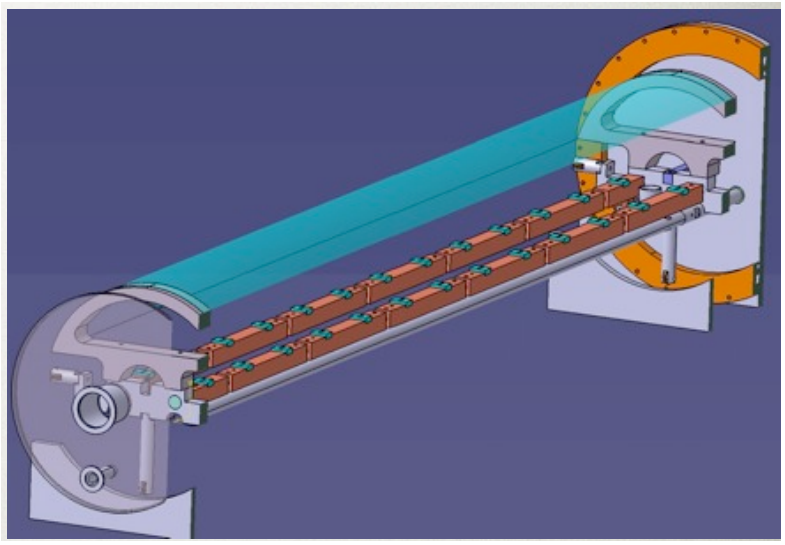

Figure 7.8: A diagram of the large evaporation chamber developed by the ArDM collaboration and currently used by NEXT.

The NEXT collaboration has acquired the large evaporation chamber developed by the ArDM collaboration (Figure 7.8), which is currently installed at the IFIC (Figure

Figure 7.9: The large evaporation chamber, details.

Figure 7.10: Response of the light tube foil (ESR+TTX) after coating, showing the characteristic blue light emission when illuminated by a UV lamp. In the upper part of the picture the same foil without coating.

7.9). This is a stainless steel vacuum chamber large enough to house reflector sheets of 120×25 cm^2 which have the right size for the NEXT-100 detector. The apparatus consists mainly of two parts, a horizontal tube with pumping connection on its closed end and a slide-in array of 13 crucibles mounted onto a Viton-sealed access flange. The crucibles are electrically connected in series for better uniformity and lower total supply current (10A). The reflector sheets are supported by 100μm wires in a crescent arrangement for constant distance to the crucibles. An evaporation cycle is started by filling the crucibles with TPB powder and positioning the TTX reflector sheet on its support.

After this preparation the sheets were inspected optically with a UV lamp (Figure 7.10) showing the characteristic re-emission in the blue.

7.4 Summary

TPB can efficiently absorb VUV radiation from xenon luminescence and re-emit in the blue, a wavelength suitable for detection with PMTs and MPPCs. We have developed two independent coating technique. One precision technique, suitable for small surfaces where a high control of the deposition is desired, and one bulk technique suitable for coating of large surfaces. The first technique can be used to coat DB and the sapphire windows of the PMT cans. The second technique is suitable for coating the large sheets that will be used to built the detector light tube. All the facilities are available at IFIC and ICMOL, in Valencia.

Chapter 8

The gas system

8.1 Description

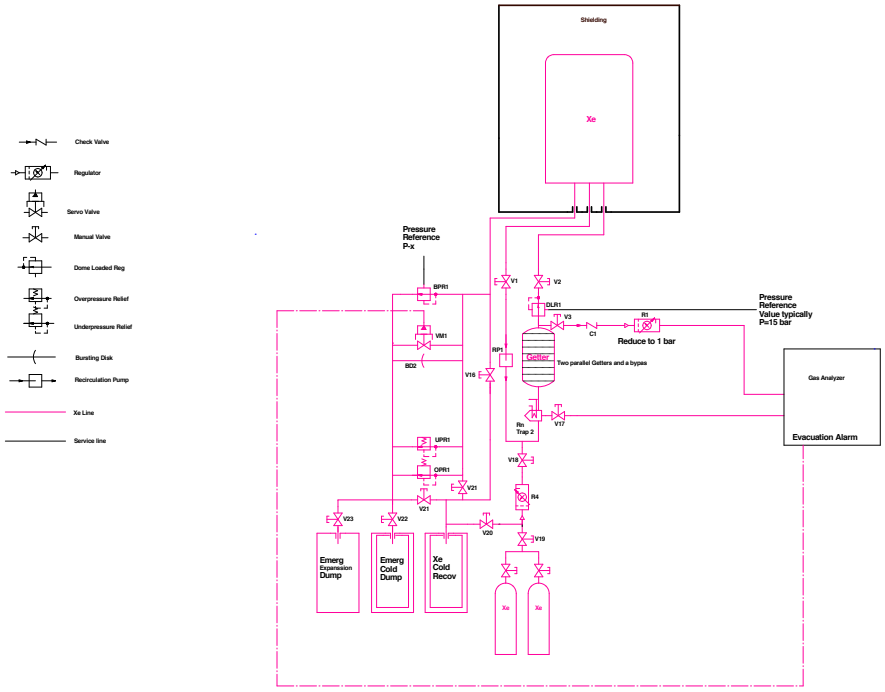

Figure 8.1: Schematic of the gas system.

During operation of the detector, Xe is circulated continuously through the Xe vessel using an axial flow pattern; it is fed in on one end and out the other end where the effluent is passed through a gas purification system.

Inside the pressure vessel, mounted to one head is an array of photomultiplier tubes

(PMTs). The PMT's cannot withstand the 15 bar Xe pressure, so they are enclosed in titanium tube pressure-proof enclosure having a sapphire window on one end. Cables from the PMT exit through a flare fitting into a copper tube that connects to a central manifold that is bolted to the underside of the axial flange of the pressure vessel head. Vacuum is is maintained inside this central manifold (and thus to the inside of the PMT enclosures); this allows the enclosures to be sniffed for Xe leakage. The PMT bases will be potted in vacuum qualified epoxy resin to allow them to operate normally with no flashover.

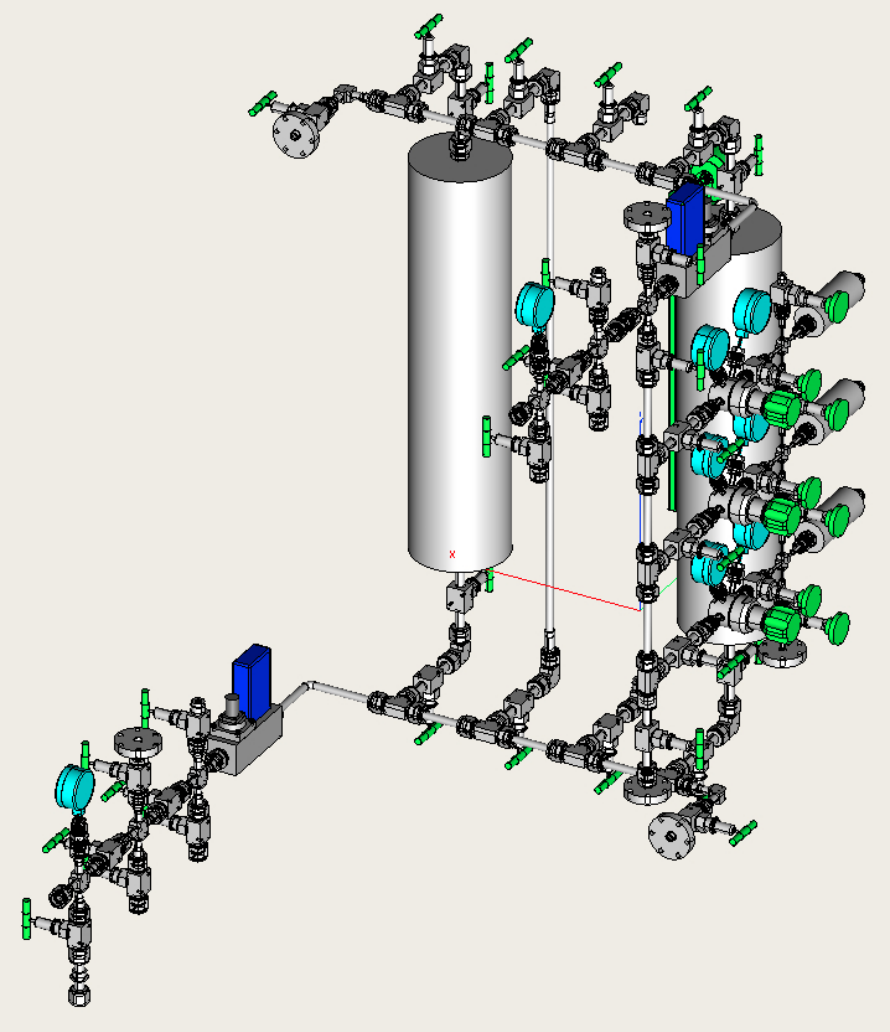

Figure 8.2: Three dimensional engineering model of the gas system piping.

During operation, the enriched Xe will be maintained as a gas at room temperature and 15 bar (abs) pressure inside the detector. Xenon is a rare and expensive gas even in its natural isotopic ratio (NXe) for which Xe 136 is 9% of the total. NEXT100 will

utilize enriched Xe 136 at a 90% or greater ratio; estimated value is 1.5 M$ for 100 kg EXe. It is imperative that any significant loss of Xe is avoided, under any foreseeable circumstance. This is also true if running with depleted (of Xe136) Xe (DXe), which may be done as an experimental control.

8.2 Gas system requirements

The pressure vessel/gas system must be capable of pressurizing, circulating, purifying, and depressurizing the detector with either enriched xenon (EXe), normal xenon (NXe), depleted xenon (DXe) argon and possibly other gases with negligible loss, and without damage to the detector. There is a high priority on avoiding loss of EXe, due to its cost and availability. A list of requirements in approximate decreasing order of importance is shown below:

1. Pressurize vessel, vacuum to 15 bar absolute (bara) - 1 hour max. - EXe, DXe, Ar
2. Depressurize vessel, on fault command, 15 bar to 1 bar - 10 sec max. - to closed reclamation system
3. Depressurize vessel, normal operation, 15 bar to vac. - 1 hour max. - to closed reclamation system
4. Pressure relief for fire or other emergency condition (to ASME std.) - vent to closed reclamation system
5. Maximum leakage, EXe through seals (total combined) - 100 gm/yr
6. Maximum loss, EXe to atmosphere - 10 gm/yr
7. Accomodate a range of gasses - EXe, DXe, N2, dry air, Ar, 95N2/5H2, EXe/TMA, EXe/CF4
8. Circulate all gasses through detector- 10 SCM/min in axial flow pattern
9. Purify EXe continuously - inlet condition to be $<$ 1ppb O2, CO2, N2, CH4, THC$<$1ppt Ra
10. Pull vacuum $1*10^{-6}$ torr at vessel port
11. Provide 1 bara N2 to PMT enclosure system
12. Provide gas circulation of 1 SCM/min through annulus

Requirement 1 above, is performed with a manual valve and regulator. 1/2" diameter connections are sufficient to meet the fill time specification. Requirement 3 is provided by opening a valve to a pre-chilled cryogenic recovery high pressure cylinder, again 1/2

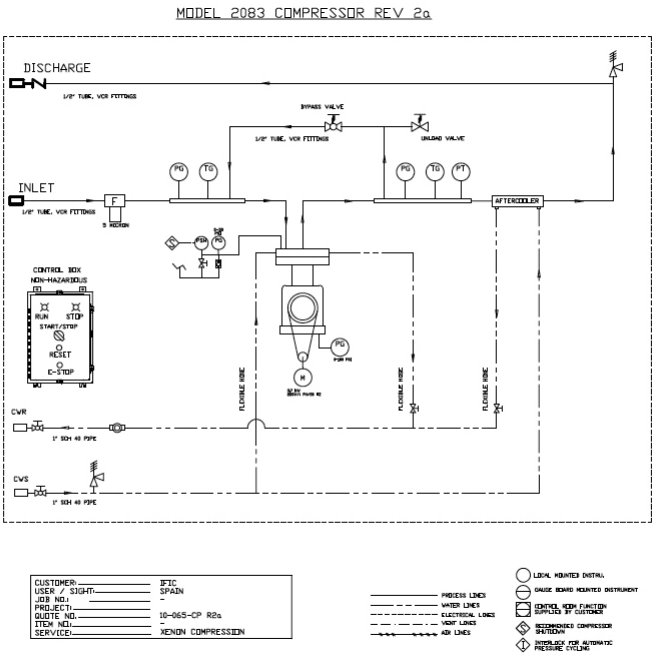

Figure 8.3: Schematic for the re-circulation pump.

" diameter lines are sufficient for this flow rate. Requirement 2 exists to protect against excessive loss of EXe in case a leak develops. It is provided by opening a fast valve or fast-actuatable burst disk leading to an evacuated recovery cylinder of 15x the pressure vessel volume; it will require a much larger port in the pressure vessel, 4" diameter. There will be a number of fault conditions that will open this valve, such as high Xe pressure in any of the sniffer ports that are installed between pressure vessel seals to satisfy requirement 5. Requirement 4 is met by having a pressure relief valve or burst disk mounted directly to the pressure vessel, with a low conductance pipe leading to the evacuated recovery cylinder. High reliability of recovery disallows use of an inflatable gas bag as an option to the recovery cylinder.

The general schematic of the gas system is given in Figure 8.1 and Figure 8.2 shows the three dimensional engineering model of the gas system showing the main valving and piping. The re-circulation pump, vacuum pump and cold traps are not shown

8.3 Pressure and flow control

Pressure control for Xenon, (whether EXe, NXe, or DXe) will be a semi-manual open loop control; the Xe pressure will be set to a set point (with a maximum ramp rate).

During normal operation the ^{136}Xe gas circuit is a closed system. Therefore the flow control can be achieved primarily by means of the re-circulation pump and a bypass line. The re-circulation operates at a set flow rate of 200 standard liters per minute

at 15 bar. In order to reduce the flow rate through the system some of the outlet gas can be diverted, by means of a manual bypass valve, into the inlet of the pump. The layout of the valving is shown in Figure 8.3. As a diagnostic flow rates can be monitored and logged using a Teledyne-HASTINGS HFM-D-301 flow logger, such as that shown in Figure 8.4. However, no active flow control is needed.

Figure 8.4: Example of a Teledyne-HASTINGS flow sensor for the NEXT 100 gas system. The pressure drop across this unit at 10 bar is approximately 0.03 bar.

The most vulnerable component of the gas system is the re-circulation pump. The enriched ^{136}Xe used in NEXT 100 project is very expensive and therefore the pump to move the gas through the re-circulation loop must have sufficient redundancy to minimize the probability of failure and leakage. Furthermore, to preserve the purity of the gas all metal to metal seals must be used. A pump manufactured by Pressure Products Industries [1]. This pump is made with metal-to-metal seals on all the wetted surfaces. The gas is moved through the system by a triple stainless steel diaphragm. Between each of the diaphragms there is a sniffer port to monitor for gas leakages. In the event of a leakage automatic emergency shutdown can be initiated (Figure 8.5).

In terms of redundancy and reliability the estimate time time between failures during continuos operation per diaphragm is in excess of 40 years. Therefore this is a very safe, clean and reliable pump with a nominal maximum flow rate of 200 standard liters per minutes.

[1] http://www.pressureproductsindustries.com/compressors/diaphragm_compressors.html

Figure 8.5: Example of the re-circulation pump chosen for the Xe purification gas system. This is a triple stainless steel diaphragm pump capable of 200 slpm flow rates.

8.4 Gas Purification

MicroTorr cold getter model number MC4500-902FV has been chosen as the purification filter for the Xe gas. Capable of removing electron negative impurities to less than 1 ppb the model chosen has a nominal flow rate of 200 standard liters per minute well in excess of the required flow rates for NEXT-100 offering sufficient spare capacity. The gas system will contain two such getters in parallel with a bypass. This configuration has been developed and used by the smaller gas systems operating at UNIZAR and IFIC. The second spare getter is placed in parallel in the event of accidental contamination of one of the getters allowing uninterrupted running. The ability to bypass the getters will allow the testing of the purification of the gas and aid in diagnostic and monitoring of the gas system. A drawing of the MC4500-902FV getter is shown in Figure 8.6.

While cold getter technology is capable of reaching the required purity levels in water and oxygen a hot getter, like one shown in Figure 8.7, can also remove nitrogen and methane. Furthermore, 362 g of cold getter material has been measured to emit 1.64 atoms of Rn [11]. In that regard a future upgrade to a hot getter technology has been considered. However, the high cost of hot getter may not be justified if other effective means of removing Rn can be found like a Rn cold trap (§8.5).

8.5 Radon Trapping:

Radon is a natural by product in the decay chain of Uranium. Therefore most materials will emanate Rn adding to the radioactive background. Several research groups in the word have been interested in developing methods of trapping Rn and preventing its entry into ultra low background detectors. A group at Queens University, Kingston

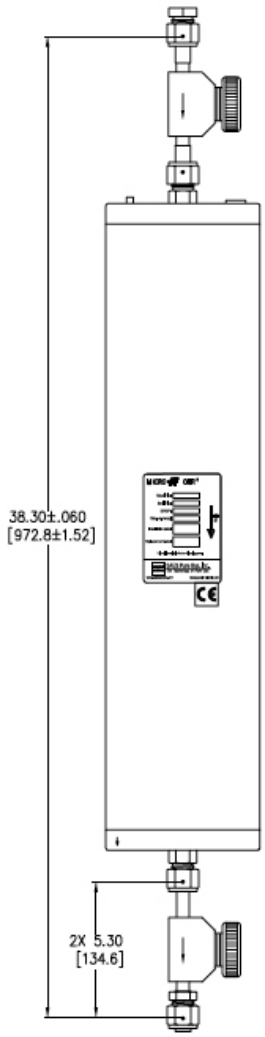

Figure 8.6: Drawing of the MC4500-902FV SAES Pure Gas getter, with VCR valves, to be used for the purification of the Xe. The gas system will contain two such parallel getters.

Figure 8.7: Example of a heated SAES getter model number PS4-MT50 with nominal flow of 150 standard liters per minute. This is a possible future upgrade to the gas system. The hot getter has been reported to be better at filtering out ^{222}Rn and therefore can be preferred purification technology to achieve ultra low radiation background rates.

Ontario, Canada has recently produced such a device [12]. Figure 8.8 shows such a trap. The trapping mechanism operates by passing the gas being filtered through a cooled column of activated carbon spheres. The carbon slows the diffusion of Rn and the low temperature retains the atoms in the trap.

Figure 8.8: ^{222}Rn trap operated at SNO lab.The trap uses activated carbon spheres to slow transmission of radon atoms. The trap tested on removing Rn from Ar gas and operates at a $-110°$C.

We plan to develop and test a ^{222}Rn trap similar to one describe above for use with Xe. The operating temperature of this trap needs to be higher that one developed by the Queens University as Xe will also freeze at $-110°$C. This can prove a very cost effective way of reducing radioactive background due to ^{222}Rn in the NEXT 100 detector.

Another possibility for a ^{222}Rn trap is a chamber filled with copper wool kept at a temperature where Rn freezes and Xe remains gaseous. The large surface area of the copper wool would offer condensation sites for the Rn. This may be a preferable trap to one utilizing activated carbon. For the carbon to be effective in removing Rn it needs to be loaded with an amount of Xe. This Xe would effectively be wasted particularly when NEXT 100 will be filled with enriched Xe.

Thus a Rn trap development and characterization would be a very important project to be undertaken by the collaboration.

8.6 Xenon reclamation

As the xenon gas that will be used in the NEXT-100 is expensive an automatic recovery system will be needed to evacuate the chamber in a case of an emergency condition. We are discussing the solution has been proposed by the LUX collaboration where a permanently chamber cooled by liquid Nitrogen will be used.

We have identified two primary conditions to trigger automatic evacuation. The first condition is an overpressure that could potentially cause an explosion. Because the gas system for NEXT-100 will be operated in a closed mode the overpressure condition could occur only under two possible conditions. The first is during the filling stage of the operation, when the system is being filled with gas and the second in the case of thermal expansion of the gas due to laboratory fire. In the case of overpressure we will have an electromechanical valve, activated by a pressure switch, that will open a pipe from the NEXT 100 chamber to a permanently cold recovery vessel. This will then cryo-pump xenon into the recovery vessel, causing the gas to freeze in the recovery

tank. In the event of the electromechanical valve failing, a mechanical spring-loaded relief valve, mounted in parallel to the electromechanical valve, would open and allow the xenon to be collected in the recovery vessel. As a final safety feature in case both the electromechanical and spring-loaded valves fail a bursting disk, also mounted in parallel to the electromechanical and spring-loaded valves, will burst connecting the NEXT 100 chamber with the recovery vessel causing the gas to be thus evacuated.

The second emergency condition would be detected as under-pressure indicating a leak in the system. Such condition would require evacuation of the NEXT 100 chamber to prevent losses of gas. If this is detected an electromechanical valve sensing under-pressure will open and evacuate the xenon into the recovery vessel.

As the recovery vessel is to be used for safety there cannot be a valve to close once the emergency recovery has been completed. Therefore in the event an automatic system is triggered a signal will be sent to an operator to arrive at the laboratory to supervise post recovery procedures. The aim of post recovery is to move the collected xenon from the recovery vessel to a closable gas bottle for future purification and use once the problems that caused the emergency conditions have been rectified. This operation must be conducted by the responsible person and would involve cryo-pumping the gas collected in the recovery vessel into a stainless steel bottle which will be valved off post transfer.

The same system can be used for controlled recovery of xenon if work needs to be done on the NEXT-100 chamber.

An alternative or an addition to the reclamation system could be a large expansion tank(s) similar to that used by the ZEPLIN II and III experiments. Figure 8.10 show a picture of one of these tanks. The aim of an expansion tank would be to quickly reduce the gas pressure in the system down to 1 bar to prevent gas escaping through a breach. This device would allow a much quicker reduction of pressure than possible with cryo-dumping. It requires, however, a large tank.

We believe that the most prudent avenue for NEXT-100 would be to have both systems, but deploy them staged in time as resource become available.

The other condition that may trigger xenon reclamation is leaking through porous seals into the vacuum or a buffer gas. For instance in the design for the energy plane (see chapter 5) xenon could leak through the photomultiplier enclosure (can). If this happens the use of a cold trap as one shown in Figure 8.11 would permit to recover the gas. The mechanism is simple: a liquid at the xenon freezing temperature circulates through the double concentric coils seen in the figure and then freezes the gas as it circulates through the trap. Periodically the trap will be heated to evaporate the trapped ^{136}Xe into the holding vessel for re-purification. In the specfici case of a leak inside the cans of the energy plane the gas will be recovered by continuously vacuum pumping the system through the cold trap.

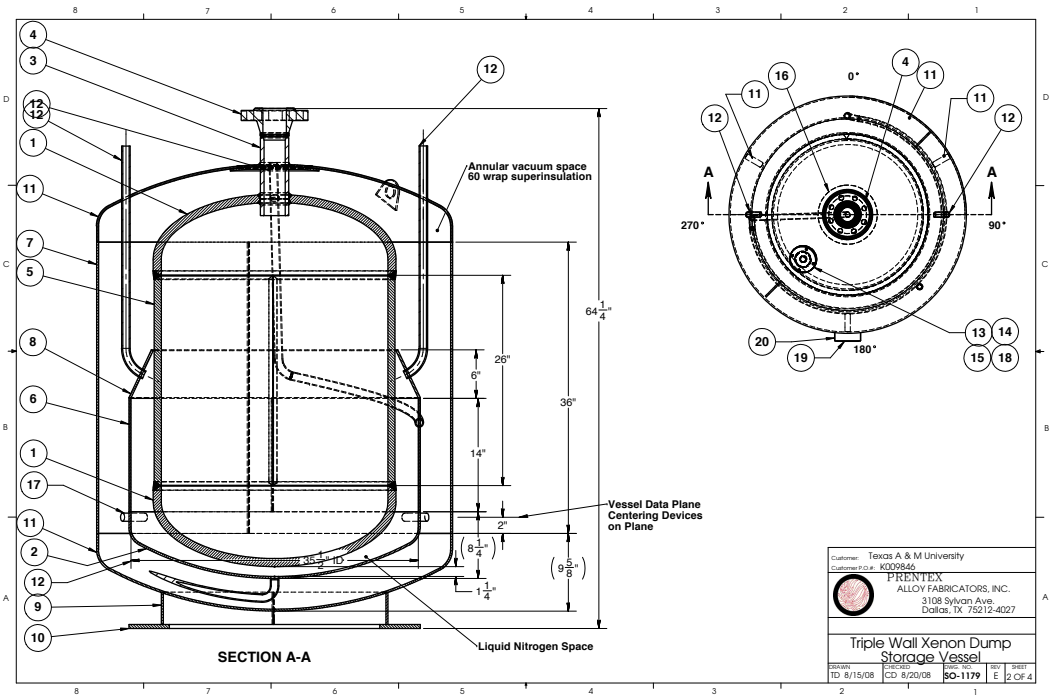

Figure 8.9: Example of a Xe cryo-recovery vessel. This vessel is part of LUX recovery system.

Figure 8.10: Example of an expansion tank that can be used for reducing the pressure in the NEXT 100 detector in an event of breach. One of the expansion tanks, from a set of two, used for ZEPLIN II and III is seen on the far background right.

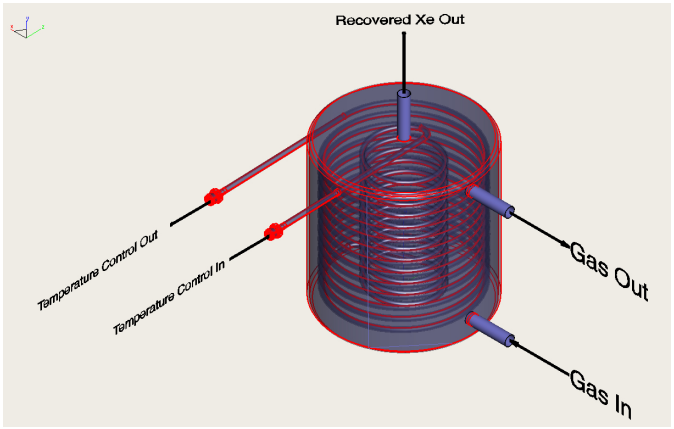

Figure 8.11: Example of a Xe cold trap.

8.7 Vacuum

To insure the cleanliness of the chamber and the gas system prior to the introduction of xenon both the chamber and the gas system need to be vacuum evacuated to as low pressure as possible. A reasonably good vacuum is in the range of 10^{-5} to 10^{-6} mbar. To achieve this the turbo-molecular pump needs to be positioned as close as possible to the vessel being evacuated. For that reason the turbo-molecular pump station will be directly connected to the NEXT 100 vessel through a large conductance valve rated for vacuum and pressure as close as possible to the vessel inside the shielding. The valve satisfying this requirement is shown in Figure 8.12, it is rated down to high vacuum and up to 25 bar pressure. It has a 100 mm orifice and thus well suited to the vacuum needs of the NEXT-100. A smaller valve of the same type has been extensively used by out Laurence Berkeley Laboratory collaborators. After reaching desired vacuum the valve will be closed, the pumping station removed and the valve enclosed in a radio pure cap to shield the detector from the radioactive impurities in the materials that make up the valve.

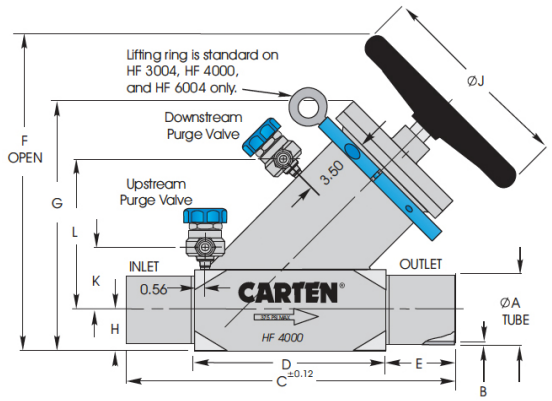

Figure 8.12: The HF4000 CARTEN valve.

Chapter 9

Shielding and platform

9.1 Introduction

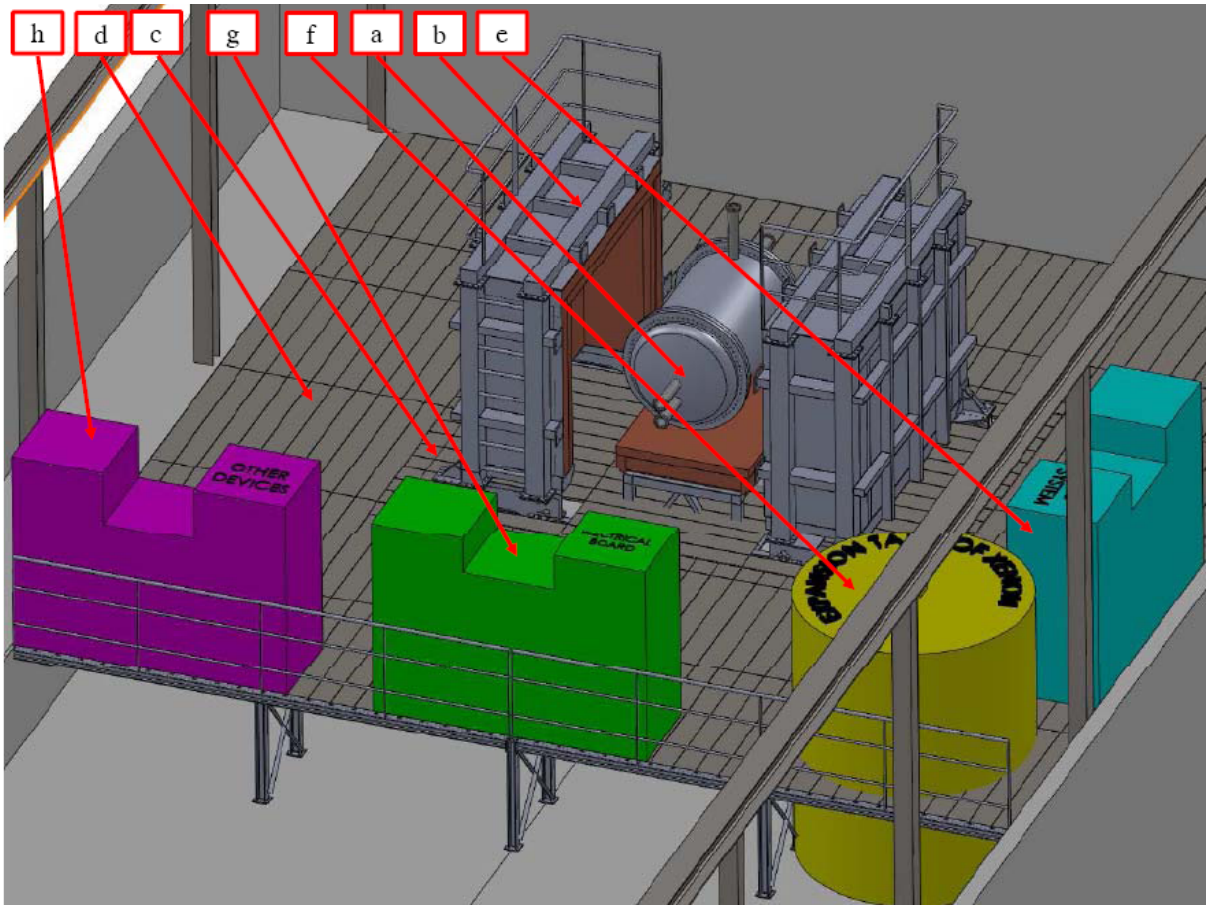

Figure 9.1: NEXT-100 lead castle and platform at the LSC

In our CDR we described two shielding possibilities, a water tank and a water-lead-copper shield. In this TDR we present our final choice. We have chosen a simple structure made of lead and copper primarily on the grounds of safety and easy access. Access to all the critical systems for improvement, repair or regular servicing, which we expect will be frequent during the first year of operation, is much easier if the detector is not immersed in liquid. In addition one avoids HV cables and high-pressure pipes inside the water.

At the same time, the shielding structure that we have designed (a.k.a. lead castle) presents significant difference with respect to that proposed in the CDR. As for the PV, we have simplified the design (e.g, eliminating the water bricks), changed to horizontal axis, and coupled the castle to a working platform (following a requirement of the LSC) and a seismic structure. The lead castle and the seismic structure thad holds the detector are independent, to allow seismic oscillations in the event of an earthquake.

Figure **??** shows a 3D view of the whole structure. The most important systems are:

a. The apparatus, described in chapter 4.

b. The shielding structure, a.k.a. lead castle made out of lead bricks and terminated by a copper sheet.

c. The platform holding the vessel, mounted on a seismic structure.

d. The platform.

e. The gas system, described in chapter 8.

f. The xenon expansion tank also described in chapter 8.

g. Power and DAQ racks.

h. Other devices (e.g, slow controls).

i. Gas and cable pipes (not show in the figure).

In this chapter we present an integrated design of the working platform (WP), the seismic structure to hold the detector (a.k.a. detector pedestal, DP) and the lead castle (LC) itself.

9.2 Overview of the layout and assembly procedure

Figure 9.2 shows a top view of the layout, with dimensions. The platform has a squared shape, with dimensions of 11×11 m^2 meters and useful surface of 112 m^2. It includes a safety area with a length of about 2 meters to provide clear access in case of an emergency.

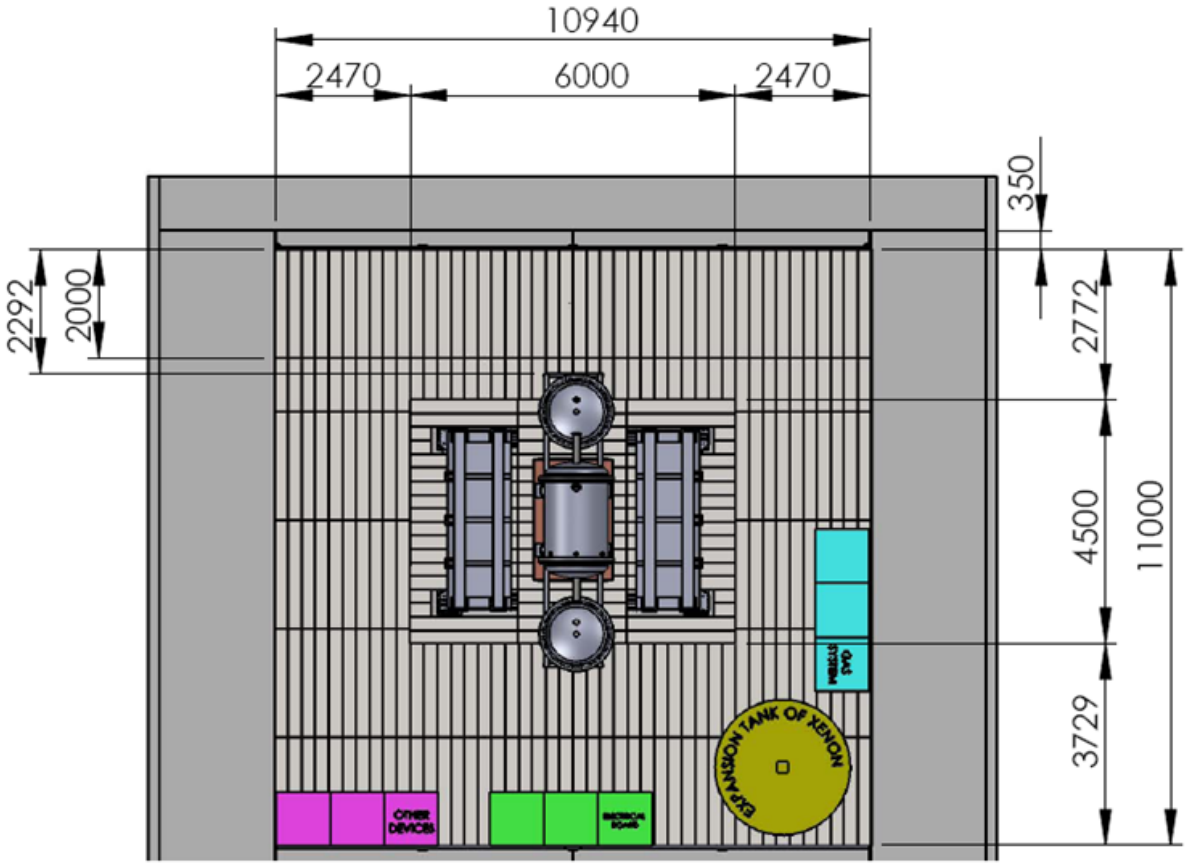

Figure 9.2: Top view of the layout

9.2.1 Assembly procedure

The assembly procedure will be divided in several steps:

1. Assembly of the detector pedestal (DP) to the LSC floor.
2. Assembly of the working platform (WP) skeleton to the LSC floor and to the LSC "pool" walls.
3. Assembly of WP floor.
4. Assembly of the lead castle (LC) motion system.
5. Assembly of the LC itself.

The DP, WP and LC are composed of modular and standard elements which will be manufactured by a supplier. All beam welding and most of the bolting will be done outside the LSC hall. Pre-assembled elements will be transported to the LSC, cleaned when necessary (e.g, the lead bricks) and assembled in place, according to a procedure previously tested at an external workshop.

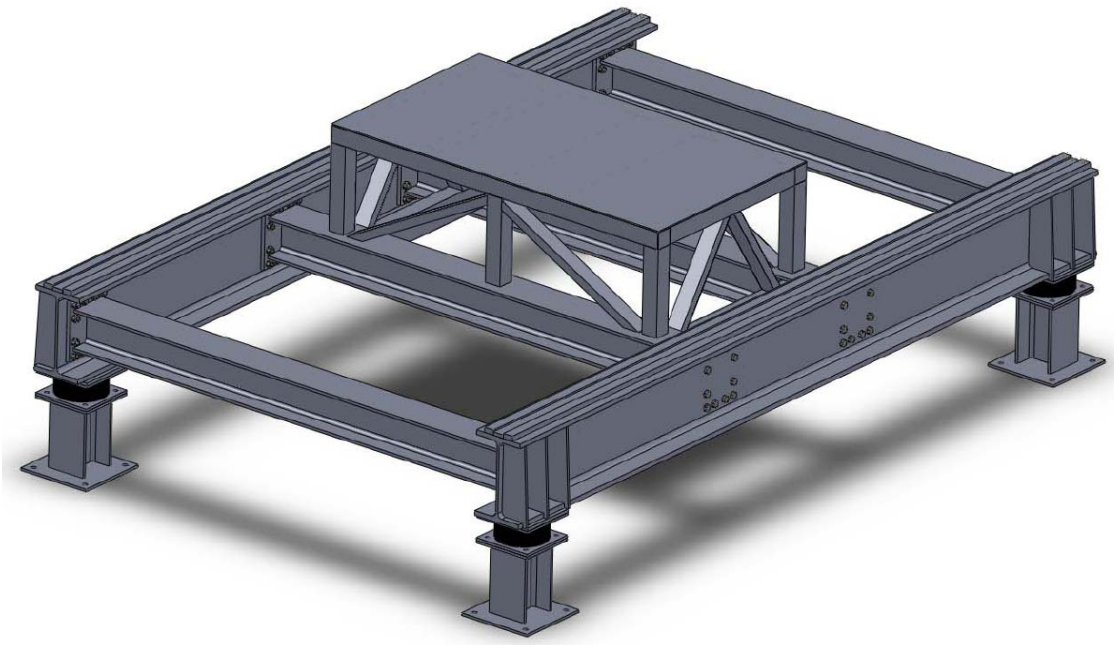

Figure 9.3: Three-dimensional view of the seismic structure (a.k.a. detector pedestal, DP)

The DP is shown in Figures 9.3 and **??**. It is anchored to the pool ground and supports all the weight of the detector and the LC. The WP shown in Figure 9.5 is designed to stand a uniform load of 300 kg/m^2 and a concentrated load of 200 kg/m^2.The

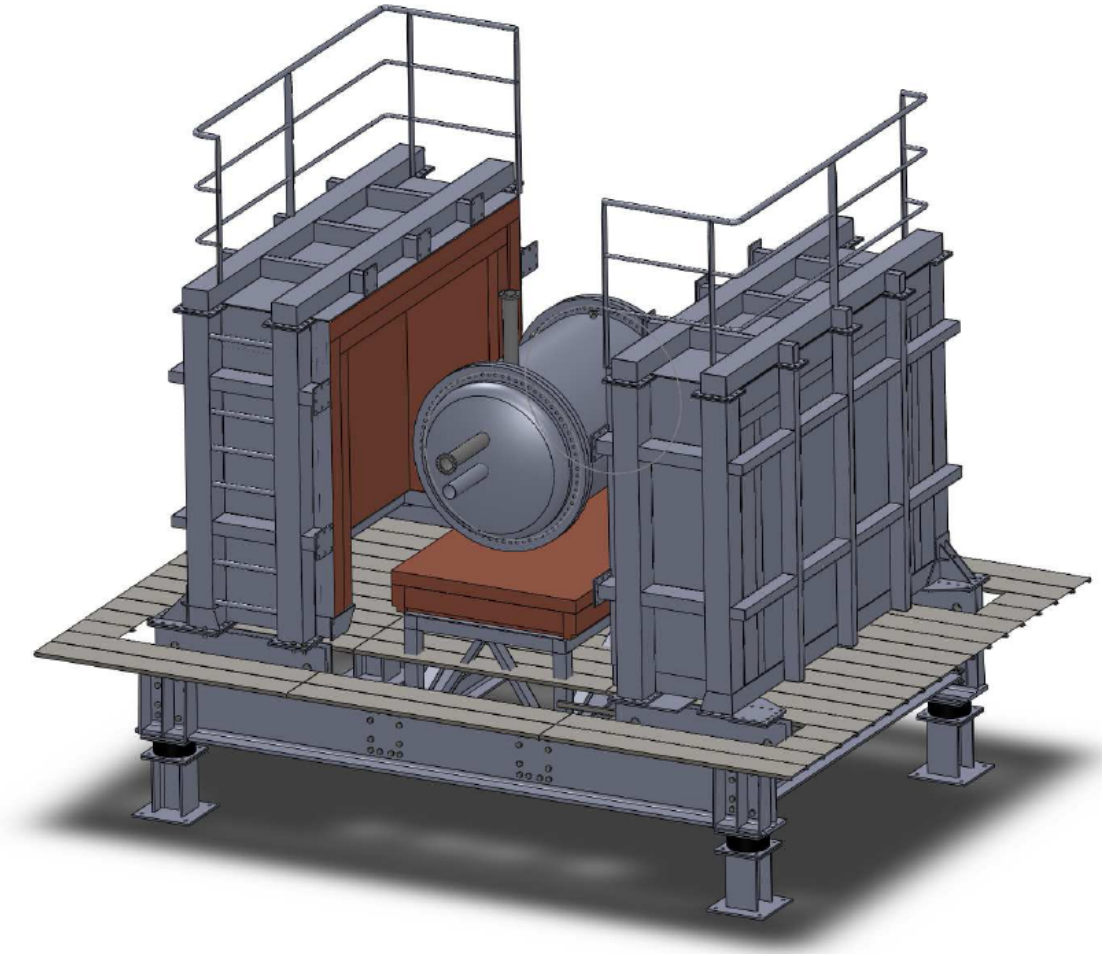

Figure 9.4: View of the DP holding the pressure vessel and movable lead castle

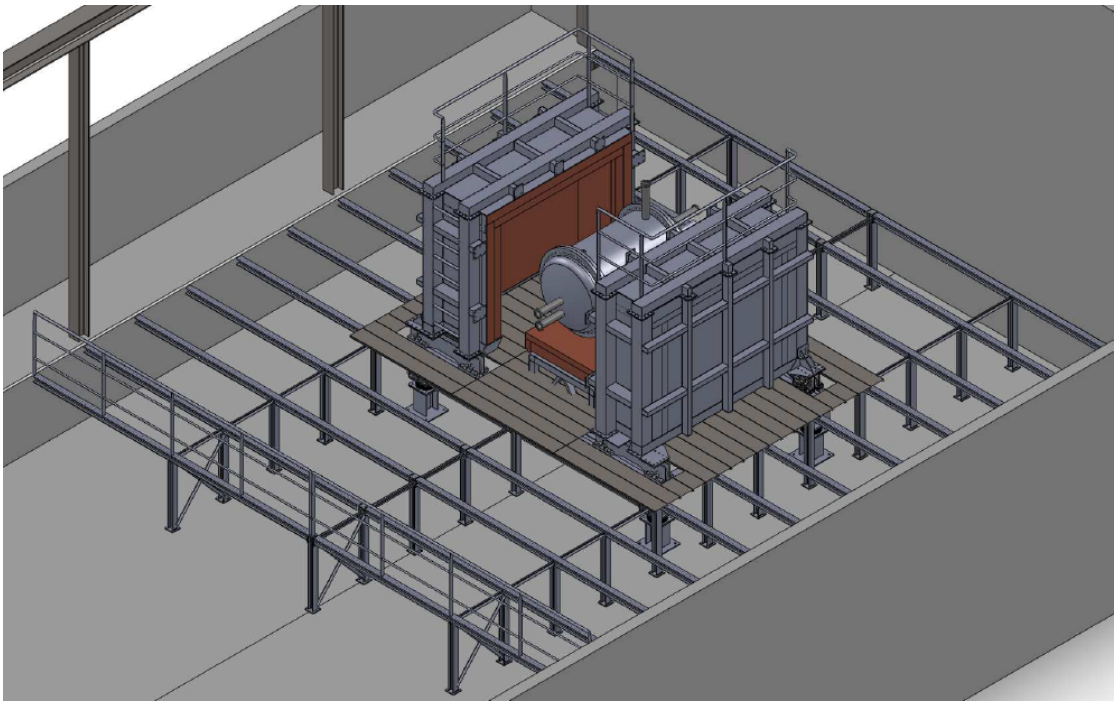

Figure 9.5: WP and DP with the lead castle opened.

platform is anchored to the pool ground and to the pool walls. Notice that the WP and the DP structured are independent to allow seismic displacements in the event of an earthquake. The platform floor tiles are made of galvanized steel and have standard dimension to minimize cost. All beams and pillars of the WP are designed with IPE and HEB cross sections, IPE-100 for pillars, HEB-240 for seismic beams and HEB-500 for main seismic beams.

9.2.2 Assembly of the castle motion system

The movable lead castle has two position: opened, as shown in Figure 9.5 and closed, as shown in Figure 9.6. The open position is used for the installation and service of the pressure vessel. The closed position is used normal operations. The LC itself is made of two halves mounted on a system of wheels that move on tracks with the help of an electric engine. The system includes a lifting device and a lock for each wheel. The lifting devices elevates all the wheels from 5 to 10mm above the guides. Once in the desired position the lock fixes the movable lead castle to the seismic structure, both in the open and in the closed position, to avoid seismic displacements during an eventual earthquake.

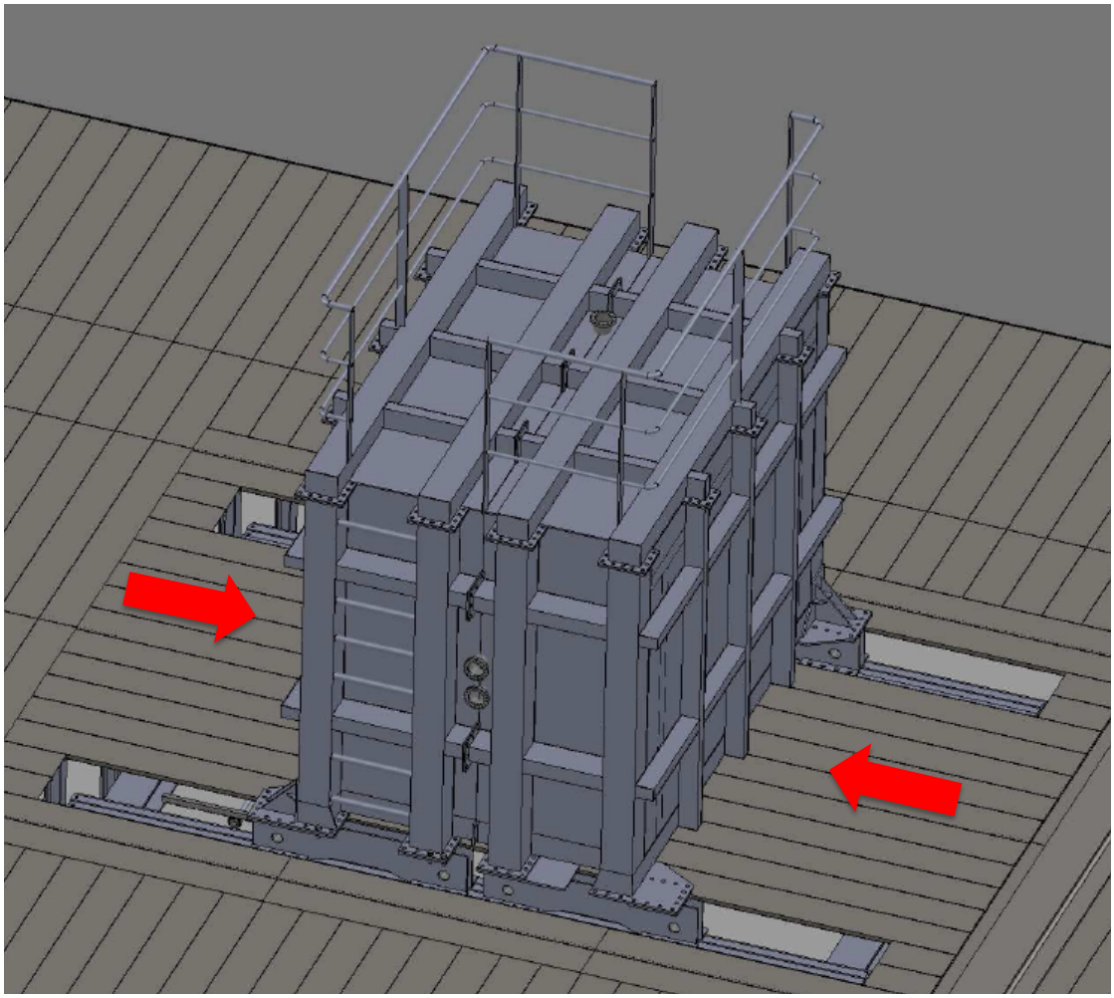

Figure 9.6: Three-dimensional view of lead castle closed

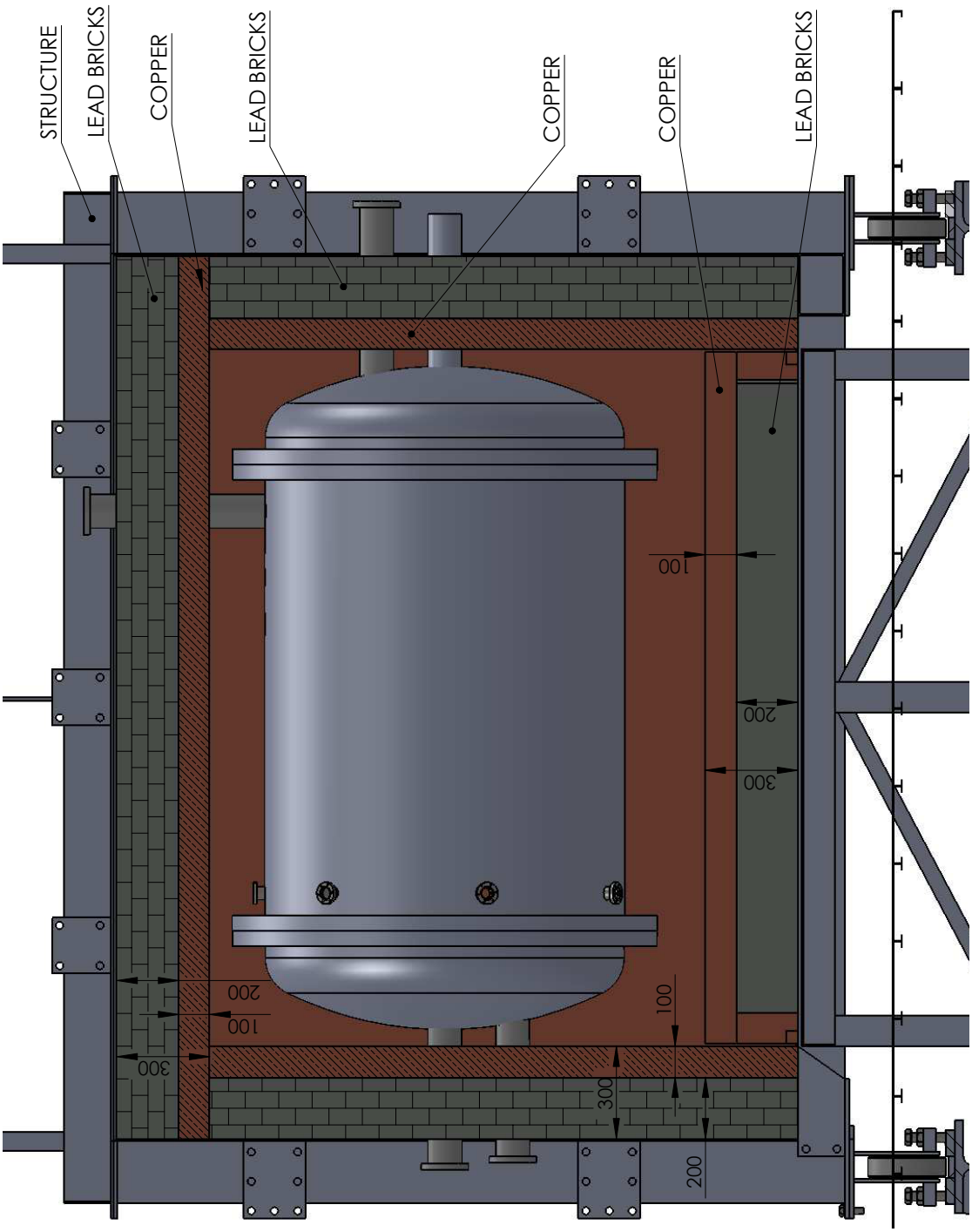

Figure 9.7: View of the lead castle

9.2.3 Assembly of the lead shielding

A top view of the lead castle is shown in Figure 9.7. The lead wall has a thickness of 20 cm and is made of fours layers of staggered lead bricks and copper or steel sheets. The lead bricks have standard dimensions ($200 \times 100 \times 50$ mm^3, and, by requirement, an activity in uranium and thorium less than 0.4 mBq/kg respectively.

A copper wall, made of copper sheets was designed to further attenuate the residual activity emanating from the lead and to provide structural support. The thickness shown in Figure 9.7 is 10 cm. However, with the introduction of the inner copper shield inside the pressure vessel the thickness of the external copper shield can be considerably reduced, and even eliminated (in reality we have simply moved it inside the PV). Instead we will use a radiopure SS sheet (from the same batch used to build the detector), 1 cm thick, to provide structural support to the whole system.

9.3 Procurement of radiopure lead and copper

9.3.1 Providers

Several companies have been contacted as lead and copper providers. An Italian company, COMETA, and a Spanish company, TECNIBUSA, are being considered for two reasons: their competitive prices and their expertise in shielding materials. Possible optimizations of the melting techniques (use of steel matrices and melting in argon atmosphere) are currently studied with both companies in order to get a lower level of radioactive contamination. The company LUVATA can provide very radiopure copper at a reasonable price for the ICS.

9.3.2 Radioactivity screening of materials.

The radioactive contamination of materials such as copper and lead has been measured by Shiva company (EAGlabs) using Glow Discharge Mass Spectrometry (GDMS). These measurements are quite promising concerning the COMETA lead sample (370 μBq/kg in ^{238}U –or 214Bi – and 72 μBq in ^{232}Th –or 26 μBq/kg in ^{208}Tl) and also to a sample from MIFER's lead provider(0,34 mBq/kg in ^{238}U –or 214Bi – and 100 μBq in ^{232}Th –or 36 μBq/kg in ^{208}Tl), which is also TECNIBUSA's provider. Improvement in melting technique would decrease radioactivity levels. Concerning copper, LUVATA could offer a level of radiopurity of less than 12.4 μBq/kg from ^{238}U and less than 4 μBq/kg from ^{232}Th (less than 1 μBq/kg from ^{208}Tl).

9.4 Summary

We have chosen a simple and easy to build lead castle as the shielding system for NEXT-100. The LC is integrated with a seismic structure (DP) and a working platform (WP). The LC opens horizontally, and the whole system is designed to withstand earthquakes. The LC thickness if 20 cm. The copper shield has been moved inside the PV, although we

Table 9.1: Summary of recent material screening results compare to XENON experiment data. Contaminations are expressed in μBq/kg. See also chapter 2

Material	U238	Th232	Tl208	Exp. or Provider
Copper	¡70	¡30	¡11	XENON
Copper	12.4	4	1	LUVATA
Lead	¡660	¡550	¡198	XENON
Lead	330	100	36	MIFER
Lead	370	72	26	COMETA
Lead	730	140	50.4	TECNIBUSA
Poly	¡230	¡94	¡34	XENON

may still leave a few cm in the castle, depending of the availability of funds. Alternatively (or in addition) a SS support sheet will be added.

Work is underway, in coordination with LSC staff to refine and complete the design of each relevant element, and the integration of all the systems.

Bibliography

[1] **EXO** Collaboration, M. Breidenbach *et. al.*, *EXO, an advanced Enriched Xenon double-beta decay Observatory (Letter of Intent)*, 2001. `http://www-project.slac.stanford.edu/exo/`.

[2] **KamLAND** Collaboration, A. Terashima *et. al.*, *R&D for possible future improvements of KamLAND*, *J. Phys. Conf. Ser.* **120** (2008) 052029.

[3] M. Koga, *KamLAND double beta decay experiment using* ^{136}Xe, in *International Conference on High Energy Physics (ICHEP)*, 2010.

[4] D. Nygren, *Optimal detectors for WIMP and* $0\nu\beta\beta$ *searches: Identical high-pressure xenon gas TPCs?*, *Nucl. Instrum. Meth.* **A581** (2007) 632–642.

[5] E. D. C. Freitas *et. al.*, *Secondary scintillation yield in high-pressure xenon gas for neutrinoless double beta decay (0nu beta beta) search*, *Phys. Lett.* **B684** (2010) 205–210.

[6] J. Gomez-Cadenas, F. Guinea, M. Fogler, M. Katsnelson, J. Martin-Albo, *et. al.*, *GraXe, graphene and xenon for neutrinoless double beta decay searches*, `arXiv:1110.6133`. * Temporary entry *.

[7] **NEXT** Collaboration, E. Gomez *et. al.*, *The NEXT-100 experiment for neutrinoless double beta decay searches (Conceptual Design Report)*, `arXiv:1106.3630`.

[8] **RD51 Collaboration** Collaboration, "Development of micro-pattern gas detectors technologies." `http://rd51-public.web.cern.ch/rd51-public/`.

[9] L. Kaufmann and A. Rubbia, *The ArDM project: A direct detection experiment, based on liquid Argon, for the search of Dark Matter*, *Nucl. Phys. Proc. Suppl.* **173** (2007) 141.

[10] **The ArDM** Collaboration, V. Boccone *et. al.*, *Development of wavelength shifter coated reflectors for the ArDM argon dark matter detector*, *JINST* **4** (2009) P06001, [`arXiv:0904.0246`].

[11] "Unpublished Report.".

[12] E. O'Dwyer, *Radon Background Reduction in DEAP-1 and DEAP-3600*. PhD thesis, Queens University-Kingston, Ontario, Canada, 2011.